


1993

Support minimized inversion of acoustic and elastic wave scattering

Ali Safaeinili
Iowa State University

Follow this and additional works at: <https://lib.dr.iastate.edu/rtd>

 Part of the [Acoustics, Dynamics, and Controls Commons](#), [Applied Mechanics Commons](#), [Electrical and Computer Engineering Commons](#), and the [Physics Commons](#)

Recommended Citation

Safaeinili, Ali, "Support minimized inversion of acoustic and elastic wave scattering" (1993). *Retrospective Theses and Dissertations*. 10264.
<https://lib.dr.iastate.edu/rtd/10264>

This Dissertation is brought to you for free and open access by the Iowa State University Capstones, Theses and Dissertations at Iowa State University Digital Repository. It has been accepted for inclusion in Retrospective Theses and Dissertations by an authorized administrator of Iowa State University Digital Repository. For more information, please contact digirep@iastate.edu.

1
93

35013

U·M·I

MICROFILMED 1993

INFORMATION TO USERS

This manuscript has been reproduced from the microfilm master. UMI films the text directly from the original or copy submitted. Thus, some thesis and dissertation copies are in typewriter face, while others may be from any type of computer printer.

The quality of this reproduction is dependent upon the quality of the copy submitted. Broken or indistinct print, colored or poor quality illustrations and photographs, print bleedthrough, substandard margins, and improper alignment can adversely affect reproduction.

In the unlikely event that the author did not send UMI a complete manuscript and there are missing pages, these will be noted. Also, if unauthorized copyright material had to be removed, a note will indicate the deletion.

Oversize materials (e.g., maps, drawings, charts) are reproduced by sectioning the original, beginning at the upper left-hand corner and continuing from left to right in equal sections with small overlaps. Each original is also photographed in one exposure and is included in reduced form at the back of the book.

Photographs included in the original manuscript have been reproduced xerographically in this copy. Higher quality 6" x 9" black and white photographic prints are available for any photographs or illustrations appearing in this copy for an additional charge. Contact UMI directly to order.

U·M·I

University Microfilms International
A Bell & Howell Information Company
300 North Zeeb Road, Ann Arbor, MI 48106-1346 USA
313/761-4700 800/521-0600



Order Number 9335013

**Support minimized inversion of acoustic and elastic wave
scattering**

Safaenili, Ali, Ph.D.

Iowa State University, 1993

U·M·I

**300 N. Zeeb Rd.
Ann Arbor, MI 48106**



Support minimized inversion of acoustic and elastic wave scattering

by

Ali Safaeinili

A Dissertation Submitted to the
Graduate Faculty in Partial Fulfillment of the
Requirements for the Degree of
DOCTOR OF PHILOSOPHY

Department: Electrical Engineering and Computer Engineering
Major: Electrical Engineering (Electromagnetics)

~~Approved:~~

Signature was redacted for privacy.

In Charge of Major Work

Signature was redacted for privacy.

~~For the Major Department~~

Signature was redacted for privacy.

For the ~~Graduate~~ College

Members of the Committee:

Signature was redacted for privacy.

Iowa State University
Ames, Iowa
1993

TABLE OF CONTENTS

ACKNOWLEDGEMENTS	xi
CHAPTER 1. INTRODUCTION	1
CHAPTER 2. MINIMUM SUPPORT INVERSION	7
Introduction	7
The Problem of Limited Data	8
Minimum $(L_2)^2$ Norm Solution	12
Minimum Support	14
Maximum Entropy Solution	19
Discussion	19
CHAPTER 3. FORWARD MODELLING OF ELASTODYNAMIC	
WAVE SCATTERING	22
Introduction	22
Wave Motion in Elastic Media	23
Algorithm Verification	29
Reducing Elastic to Acoustic	34
CHAPTER 4. MINIMUM SUPPORT LINEARIZED ACOUSTIC	
INVERSION	37

Introduction	37
Model For The Forward Problem	37
A Two Dimensional Example	41
The Support Minimized Inversion	44
CHAPTER 5. SUPPORT MINIMIZED NONLINEAR ACOUS-	
TIC INVERSION WITHOUT ABSOLUTE PHASE	54
Introduction	54
Forward Model	55
Inversion	59
Results	63
Absolute Phase Error Correction	71
Conclusion	77
CHAPTER 6. SUPPORT MINIMIZED NONLINEAR ELASTIC	
INVERSION	79
Introduction	79
Forward Elastic Model	80
Inversion Algorithm	81
Inversion Examples	82
Conclusion	91
BIBLIOGRAPHY	92
APPENDIX A. GREEN'S FUNCTION DERIVATION	98
APPENDIX B. DISCRETIZATION OF THE INTEGRAL EQUA-	
TION	100

APPENDIX C. DISCRETIZATION OF THE INTEGRAL EQUATION (ALTERNATE METHOD)	104
APPENDIX D. SERIES SOLUTION TO SCATTERING FROM A CYLINDER	107
APPENDIX E. PARALLEL COMPUTATION	110
APPENDIX F. GRADIENT CALCULATION	112
APPENDIX G. ASYMPTOTIC EVALUATION OF INCIDENT FIELD	117
APPENDIX H. CALCULATION OF THE VOLTAGE USING THE RECIPROCITY THEOREM	118
APPENDIX I. RELATIONSHIP BETWEEN VOLTAGE AND THE SCATTERER POTENTIAL	120
APPENDIX J. FOCUSING OF AN ARRAY OF TRANSDUCERS	123

LIST OF FIGURES

Figure 1.1:	Pulse-Echo and Pitch-Catch mode ultrasonic measurements.	3
Figure 2.1:	What are the numbers in the box given the sums of the rows and columns	9
Figure 2.2:	The vectors spanning the null space.	11
Figure 2.3:	Minimum $(L_2)^2$ solution	13
Figure 2.4:	Minimum support: a) functional b) gradient of the functional, for different values of ϵ	15
Figure 2.5:	Minimum support solution	15
Figure 2.6:	Minimum support: a) functional b) gradient of the functional, for different values of ϵ	16
Figure 2.7:	Minimum support solution with upper bound penalty $x_{th} = 3$	16
Figure 2.8:	Minimum support solution with upper bound penalty $x_{th} = 2$	18
Figure 2.9:	Maximum Entropy functional for different values of x_0	20
Figure 2.10:	Maximum Entropy solution with a small x_0	20
Figure 3.1:	Forward scattering calculation from a small inhomogeneity .	25
Figure 3.2:	An incident plane wave impinging on a cylindrical scatterer .	29

Figure 3.3:	Total back-scattered power from a steel cylindrical scatterer in Silicon-Nitride with P-wave incidence: Comparison between the solutions from series method and the integral equation method for $ka = 0.6$ (e.g., a 30μ cross section at 20 Mhz) . .	30
Figure 3.4:	Profile of the scatterers ranging from sharp to smooth boundary	32
Figure 3.5:	Comparing backscattered power from cylindrical scatterers a) back-scattered power for $ka = 0.6$. b) back-scattered power for $ka = 1.5$	32
Figure 3.6:	Comparing the series solution (grey) with the integral equation solutions with (solid)/without (dotted) Born approximation: a) $ka = 0.6$ b) $ka = 0.9$ c) $ka = 1.2$, and d) $ka = 1.5$. .	33
Figure 4.1:	Ultrasonic probing: volumetric image may be obtained using a two-dimensional scan	38
Figure 4.2:	Incident field in the far-field	39
Figure 4.3:	An example of data coverage in the k -space using a limited-view-angle pulse-echo system	42
Figure 4.4:	Case 1: Original object (min=0.0, max=1.0)	47
Figure 4.5:	Inversion result using 150 degree view-angle and bandwidth $1 < ka < 6$ a) using $(L_2)^2$ norm (min=-0.26 max= 0.95) and b) using the minimum support functional (min=0.0 max= 1.0)	48
Figure 4.6:	Inversion result using 120 degree view-angle and bandwidth $1 < ka < 6$ a) using $(L_2)^2$ norm (min=-0.29 max= 0.86) b) using the minimum support functional (min=0.0 max= 1.0)	49

Figure 4.7:	Case 2: a) Original scatterer (min =0.0, max = 1.0), b) $(L_2)^2$ norm reconstruction of the scatterer using 90 degree view-angle and bandwidth $1 < ka < 6$ (min= -0.37, max = 0.54)	50
Figure 4.8:	Inversion result using 90 degree view-angle and bandwidth $1 < ka < 6$ with the minimum support functional: a) with no amplitude constraint (min=0.0, max= 2.0), b) with amplitude constraint at $x_{th} = 1.1$ (min=0.0, max=1.12)	51
Figure 4.9:	Inversion result using 90 degree view-angle and bandwidth $1 < ka < 6$ with the minimum support functional: a) with amplitude constraint at $x_{th} = 1.0$ (min=0.0, max=1.0) b) with amplitude constraint at $x_{th} = 0.5$ (min=0.0, max=0.87)	52
Figure 4.10:	Inversion result using 90 degree view-angle and bandwidth $1 < ka < 6$ a) using maximum entropy functional (min=-0.34 max= 1.12) b) using the minimum support functional (min=0.0 max= 1.24)	53
Figure 5.1:	Acoustic back-scatter measurement.	57
Figure 5.2:	Acoustic case 1: a) true scatterer potential $v(x)$ b) reconstruction using 6 frequency and 19 measurement position over 180 degree, c) reconstruction using 6 frequency and 19 measurement position over 180 degree with minimum support.	64
Figure 5.3:	Acoustic case 2: a) true scatterer potential $v(x)$, b) reconstruction using 10 frequency and 19 measurement position over 180 degree.	65

Figure 5.4:	Spatial frequency domain profile for: a) acoustic scatterer of case 1, b) acoustic scatterer of case 2.	66
Figure 5.5:	Acoustic reconstruction of scatterer in case 1: a) with 3 frequency and 19 measurements positions over 180 degree, b) with 3 frequency and 13 measurements positions over 120 degree, c) with 3 frequency and 10 measurement positions over 90 degree, d,e, and f are the above with minimum support functional minimized.	67
Figure 5.6:	Acoustic reconstruction of scatterer in case 2: a) with 3 frequency and 19 measurements positions over 180 degree, b) with 3 frequency and 13 measurements positions over 120 degree, c) with 3 frequency and 10 measurement positions over 90 degree, d,e, and f are the above with minimum support functional minimized.	68
Figure 5.7:	Acoustic reconstruction of scatterer in case 1 using: a) 6 frequency and 10 measurement positions over 90 degree, b) 6 frequency and 10 measurement positions over 90 degree with minimum support constraint, c) 6 frequency and 10 measurement positions over 90 degree with minimum support constraint and a quadratic penalty function for large pixels with $g_{ub} = 1.0$	69
Figure 5.8:	Experiment set-up: Back-scattered signal measured from two rubber band each $1mm$ thick using a $500Khz$ transducer. . .	72

Figure 5.9:	Pulse-echo time signals were collected at 19 angles over a 180 degree view angle.	73
Figure 5.10:	Time signals are digitized and Fourier transformed: inversion algorithm uses spectral components in the band-pass of the system.	74
Figure 5.11:	Some of collected Pulse-echo time signals.	75
Figure 5.12:	Results of inversion for scatter potential v using experimental data: a) without the minimum support functional and absolute phase corrections, b) with the minimum support functional and absolute phase corrections.	76
Figure 5.13:	Phase corrections at center frequency of 500 khz ($\theta_0 = 360d_i/\lambda_0$). 78	
Figure 6.1:	Curves showing the value of the penalty function versus λ for few frequencies: a) marching on a line from $v = 0$ to $v = v_0$, b) marching on a line from $v = 1$ to $v = v_0$	84
Figure 6.2:	Comparing the total penalty function for the two cases.	85
Figure 6.3:	Original scatterer: Steel scatterer in Silicon-Nitride.	87
Figure 6.4:	Inversion of a steel scatterer in Silicon-Nitride background using 180 degree view angle and $0.1 < ka < 1.5$ (e.g. for a 30μ radius particle $3 \text{ Mhz} < f < 50 \text{ Mhz}$): a) without minimum support, b) with the minimum support	87
Figure 6.5:	Inversion of a steel scatterer in Silicon-Nitride background using 150 degree view angle and $0.1 < ka < 1.5$ (e.g. for a 30μ radius particle $3 \text{ Mhz} < f < 50 \text{ Mhz}$): a) without minimum support b) with the minimum support	88

Figure 6.6:	Inversion of a steel scatterer in Silicon-Nitride background using 120 degree view angle and $0.1 < ka < 1.5$ (e.g. for a 30μ radius particle $3 \text{ Mhz} < f < 50 \text{ Mhz}$): a) without minimum support b) with the minimum support	88
Figure 6.7:	Original scatterer for case of steel in Silicon-Nitride	89
Figure 6.8:	Inversion of a steel scatterer in Silicon-Nitride background using 180 degree view-angle and $0.7 < ka < 6$ (e.g. for a 30μ radius particle $20 \text{ Mhz} < f < 200 \text{ Mhz}$): a) without using minimum support, b) with using minimum support	90

ACKNOWLEDGEMENTS

This work has become possible with the help of many of my friends and co-workers at the Center for Nondestructive Evaluation in Ames. I am indebted to all of my committee members for their time and their valuable guidance. I would like to thank my professor Dr. R.A. Roberts whose clear vision and detailed guidance had a great impact on the quality of my work. I appreciated his availability for answering my questions at all time during the past three years. Finally, I would like to thank my parents for all their sacrifices so I could get the best education, and my wife Lisa who supported me and coped patiently with a student as a husband for the past four years.

This work was partially supported by the Director of Energy Research, office of Basic Energy Sciences. The Ames Laboratory is operated for the U.S. Department of Energy by Iowa State University under Contract No. W-7405-ENG-82. The United States government has assigned the DOE Report number IS-T1672 to this thesis.

CHAPTER 1. INTRODUCTION

The purpose of this work is to further the state of the art in ultrasonic inverse scattering for NDE and remote sensing applications. Ultrasonic probing is an effective method of acquiring information for a variety of types of objects in NDE. The application may vary from remote sensing of large tanks containing hazardous material to imaging of flaws in industrial parts. In all of these applications, one extracts information about objects under probe from a voltage due to back-scattered and/or transmission scattered field obtained by one or an array of transducers. In these applications, the quality of testing and evaluation is adversely affected by problems such as limited aperture and limited temporal bandwidth. These problems are compounded by the lack of accurate phase information and use of inaccurate models. The importance of the above factors are widely known, however, much work is needed to find methods of reducing their impact on the quality evaluation.

In very general terms, inversion is the process of solving for a unknown quantity (X) that has been operated on by a known operator \mathcal{F} to yield $Y = \mathcal{F}(X)$, which are given as measured data. In many cases, an exact closed form solution for $X = \mathcal{F}^{-1}(Y)$ may not be found. In these cases, we can, generally, only find X over a discrete domain with finite accuracy using numerical methods. Hence, the term “inversion” in this work does not imply a complete access to the solution X , rather

it means approximate and partial estimate of X . It should be noted that this is natural when dealing with numerical inversion. Detection problem is an example of an inversion in which X is only partially recovered. Detection of a signal merely states that X is non zero and does not give any further information about X . Imaging can be considered as solving for a transformed version of X say $g(X)$, where $g(X)$ is easier interpreted visually than $\mathcal{F}(X)$. Finally, for cases where X is found explicitly we have inversion in the conventional sense.

Normally, data which is available for inversion ($Y = \mathcal{F}[X]$), covers only a part of the range of the operation. This introduces a non uniqueness problem which may be overcome by adding a priori information to the available data (i.e., “regularization of data”). In the present work, this information is added by optimization of an appropriate functional (e.g., $(L_2)^2$ norm, maximum entropy [6, 41], minimum support, etc.) using a variational approach [35, 22].

Our specific problem deals with calculating material parameters (or a function of the parameters) of the object using ultrasonic measurements. The object parameters are found with a finite accuracy which is set by the noise level, extent of the coverage of measured data in both temporal and spatial domain, and accuracy of phase measurements between transducers. In Fig. 1.1, a common ultrasonic set up is shown. The two main modes of data collection are 1) pulse-echo and 2) pitch-catch.

In the pulse-echo mode, the same transducer is used for both transmission and reception of signal while in the pitch-catch mode, transducer and receiver are different. The limited data in this application is caused by 1) finite temporal bandwidth of the transducer-receiver system, 2) limited angular access in the data collection process,

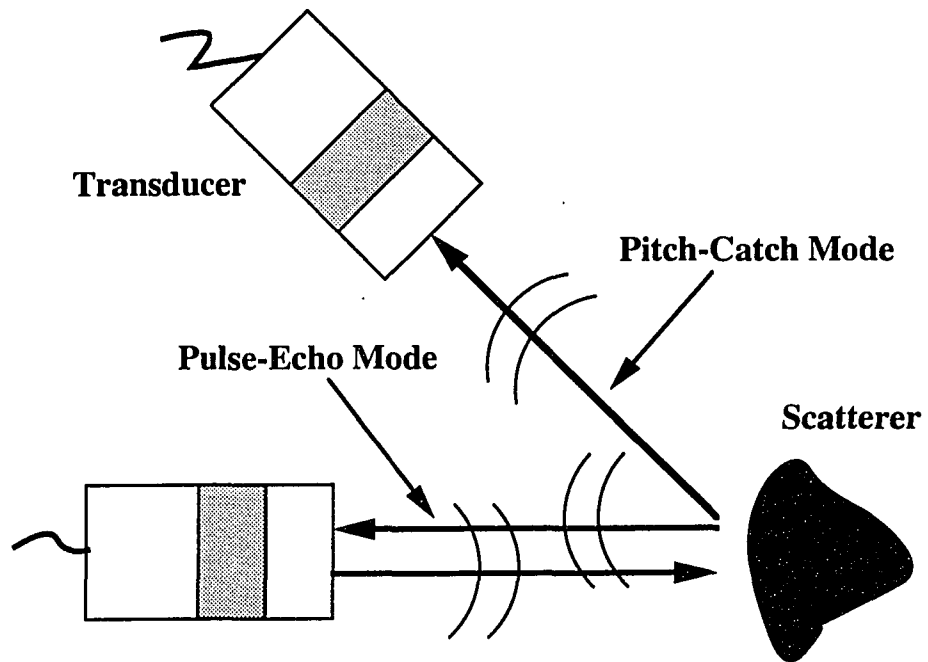


Figure 1.1: Pulse-Echo and Pitch-Catch mode ultrasonic measurements.

3) lack of absolute phase between measurements at different locations (also known as the *The Zero-of-Time problem*), 4) nonlinear dependence of measurements on the scatterer, and 5) noise. The objective is to characterize the scatterer using limited data as mentioned above. Since, in this work, the emphasis is on the problem of the limited data in ultrasonic inversion, all the discussions regarding the forward problems are of secondary concern. In all of the inversions discussed, the forward process can be viewed as a black box which can be replaced with more efficient forward procedures as needed. Throughout this work an exact forward solution is used with the exception of the Chapter III in which the linearized inversion is discussed. Although using an exact forward solution may not be efficient, it was done in order to keep the study of compensation for limited data separate from the study of approximate forward scattering solutions. Although the choice of an efficient forward process was secondary to this work, an understanding of the forward process is of primary importance in any inversion effort. Approximate models provide adequate solution with much less computation [33, 18, 5, 19, 29, 4, 45, 44, 3]. However, they do not provide solutions that satisfy the physics governing the measurement process. In cases where more accurate solutions are needed an exact inversion is useful. The solution from an exact inversion, even when not providing a unique solution, is guaranteed to agree with the physical model governing the measurement process. In other words, a valid solution is obtained within the tolerances dictated by the available data. Furthermore, as it will be shown later, a unique solution may be obtained if additional *a priori* information such as minimum support is available.

Inversion is usually an ill-posed problem. In order to obtain a solution one has to resort to regularization techniques. The ill-posedness of the inversion becomes even

more severe when data is limited. This problem of ill-posedness plagues almost all inversion methods in many different fields (e.g., radio astronomy, X-ray tomography, and diffraction tomography and holography). The most classic mathematical approach in removing the singularities and ill-posedness are methods such as minimum $(L_2)^2$ norm [34]. These methods make it possible to obtain a unique solution. However, in many cases the obtained solution is not the best solution! The best solution is the one that is consistent with all the available qualitative as well as quantitative information. The most delicate task is to balance the degree of consistency with each available piece of information. For example, in radio astronomy, the obtained images suffer from artifacts which result from incomplete data. The image with the artifacts is consistent with the collected data, however, it is inconsistent with physical reality, the physical reality being the fact that most astronomical objects are isolated objects in a dark background. Although this information is only a qualitative observation based on experience, one can develop algorithms such that the image obtained is consistent with both data and observer's expectations.

In limited-view-angle X-ray tomography, a similar phenomena also occurs [36, 37, 38, 31]. Many researchers have proposed ways to include qualitative information. Many are based on procedures that are being used only because they result in expected images [36, 38, 31]. Recently, Roberts [31] proposed a minimal support function which for the first time was designed to achieve a well defined objective. He had observed that in almost all his X-ray tomograms reconstructed from limited data, the artifacts covered a large area in the image. He proposed a functional which would choose a solution which is consistent with the collected data and has minimum support. This observation is very important in that many important characteristics

of an NDE tomogram can be formulated in the form of such functionals (e.g., boundedness, smoothness, etc.). The solution can be obtained using appropriate methods to optimize the functional. The same type of approach can be used in diffraction tomography with limited data.

In what follows, we will start by explaining the need for constrained inversion. This is done in Chapter II where the problem of limited data and its effects on inversion are discussed. In this chapter, it is shown how a *non uniqueness* problem can be remedied with added information through optimization of functionals. Finally, a few simple examples are presented to clarify the issue. Chapter III gives an overview of the physics of elastodynamic motion and defines all the equations that are used in the following chapters. In this chapter, we start with the general equation of motion in solids and then reduce it to the case of the ideal fluid. Also in this chapter, we discuss how the forward problem can be solved using a volume integral equation approach. Chapter IV presents a minimum support linearized inversion scheme for acoustic scatterers in an acoustic background. The limited data inversion results are presented along with improved results when appropriate functionals are optimized in the inversion. In Chapter V, we use an exact nonlinear model for the forward process and present results of inversion with/without using minimum support functional. Also, in this chapter, an inversion result is presented using experimental data where the *zero-of-time* is missing for the backscattered time signals. Finally, in Chapter VI, a nonlinear forward model is used for the inversion of elastic scatterers in elastic background.

CHAPTER 2. MINIMUM SUPPORT INVERSION

Introduction

The problem of inversion of incomplete data is common to many areas of NDE. Incomplete data is defined as lack of uniqueness in the solution. In general, given a forward problem $u = \mathcal{F}(s)$, the inverse problem seeks to find $s = \mathcal{F}^{-1}(u)$, where \mathcal{F} is a one-to-one mapping. Functions u and s can be defined as $u : D_u \mapsto R_u$ and $D_s \mapsto R_s$ where D_u and D_s are domains of functions u and s and R_u and R_s are ranges of functions u and s respectively. Let's assume, functions u and s are defined such that they should be known entirely over domains D_u and D_s to make functional \mathcal{F} one-to-one. Let's define such domains as *essential domain*. In practice, measurements might be defined over a domain which is not *essential* and has to be mapped onto an essential domain.

If \mathcal{F} is one-to-one s can be obtained uniquely given a measurement u defined over its entire *essential* D_u . However in most applications, a complete measurement u is not available, instead u is known over a finite subset of its domain D_u which we denote as D_u^m . One can envision a function u' such that it is zero over D_u^m and nonzero otherwise. Clearly, $x = \mathcal{F}^{-1}(u+u')$ is a valid solution to the inverse problem since $u+u' = \mathcal{F}(x)$ which is equal to u over D_u^m . Since there can be infinite number of functions like u' and \mathcal{F} is one-to-one, there will be infinite number of solutions to

the inverse problem.

For example in the ultrasonic inverse problem, one may consider a real valued scatterer which is defined over $R^3 \mapsto R$. The measurements are the complex scattered values measured in space and time, i.e. it is defined over $R^4 \mapsto C$. In this example, the essential domain of measurement has a lower dimension than 4. This is evident from the fact that we are trying to find a function with a dimension $4 = 3 + 1$ from a function with a dimension $6 = 4 + 2$. For example in Born inversion a measurement set defined as $R^3 \mapsto R$ is sufficient. The three dimensions of the essential domain may be either two dimensional space and one dimension time, or three dimension space. Normally, the measurement function is known over a finite region of space and time which does not map onto the entire essential domain. As mentioned above, one may find infinite number of scatterers to match the function over a subdomain of measurements.

Although a unique solution may never be obtained in most inverse problems, it is still possible to produce valuable information through inversion. Fortunately, in most applied problems, in addition to the measurements, there are other qualitative and/or quantitative information that can be used in getting a "better" (possibly unique) solution. To demonstrate this, the following example is presented.

The Problem of Limited Data

Let's consider a 3×3 grid on which there are 9 real numbers x_i . These 9 numbers will form the solution vector X . The measurements will consist of 6 real numbers $y_i = \mathcal{P}_i(X)$ each showing the sum of a row or a column as shown in Fig. 2.1.

Clearly, there can be an infinite number of solutions to this problem. If X_0 is a

$$y_1 = 9 \quad y_2 = 6 \quad y_3 = 3$$

x_1	x_2	x_3	$y_4 = 3$
x_4	x_5	x_6	$y_5 = 9$
x_7	x_8	x_9	$y_6 = 6$

$$P_1(x) = y_1 = 9 = x_1 + x_4 + x_7$$

$$P_2(x) = y_2 = 6 = x_2 + x_5 + x_8$$

$$P_3(x) = y_3 = 3 = x_3 + x_6 + x_9$$

$$P_4(x) = y_4 = 3 = x_1 + x_2 + x_3$$

$$P_5(x) = y_5 = 9 = x_4 + x_5 + x_6$$

$$P_6(x) = y_6 = 6 = x_7 + x_8 + x_9$$

Figure 2.1: What are the numbers in the box given the sums of the rows and columns

solution then

$$X = X_0 + \sum_i c_i X_i \quad (2.1)$$

is also a solution where X_i 's are the vectors spanning the null space and c_i 's could take any value. Corresponding X_i 's for this problem are given in Fig. 2.2. By definition, the result of forward operator on any vector in the null space is zero which can be verified easily by inspecting the vectors in Fig. 2.2.

$$\mathcal{P}_i(X_j) = 0 \quad i = 1, 6 \quad j = 1, 4 \quad (2.2)$$

where the \mathcal{P}_i operator gives the sum of element on columns or rows ($i = 1, \dots, 6$ for 3 rows and 3 columns). The dimension of the Null space is 4 which implies there are only five independent equations. This can be seen by realizing that sum of the three numbers corresponding to the sum of the columns or rows are sum of all numbers on the grid; hence given any five numbers the sixth can be found.

To obtain a unique solution, we need to provide additional constraint on the solution. This can be done through optimizing a penalty functional defined as

$$\mathcal{E} = \sum_{i=1}^6 \mathcal{D}(\mathcal{P}_i(X), y_i) + \lambda \sum_{j=1}^9 \mathcal{S}(x_j) \quad (2.3)$$

where $\mathcal{D}(\cdot)$ is a distance measure and $\mathcal{S}(\cdot)$ is an additional constraint on the solution. Minimizing $\sum_{i=1}^6 \mathcal{D}(\mathcal{P}_i(X), y_i)$ guarantees the fidelity to the measurements while optimizing $\sum_{j=1}^9 \mathcal{S}(x_j)$ helps narrow the solution set to one with a characteristic favored (biased) by the constraint. In the following sections, we discuss a few examples for the function $\mathcal{S}(\cdot)$ (Minimum $(L_2)^2$ norm, Minimum Support, and Maximum Entropy) and for each case provide the relevant solution.

-0.8	1.6	-0.8	2.6	-0.9	-1.6
-1.4	-0.3	1.7	-1.8	0.6	1.2
2.2	-1.3	-0.9	-0.7	0.3	0.4
0.0	-1.1	1.1	0.0	-1.5	1.5
-0.3	-1.0	1.3	-1.3	2.4	-1.1
0.3	2.1	-2.4	1.3	-0.9	-0.4

Figure 2.2: The vectors spanning the null space.

Minimum $(L_2)^2$ Norm Solution

Suppose we know that the solution to our problem is the one with minimum sum of the squared (minimum $(L_2)^2$ norm). Then a solution may be obtained which belongs to a subset of the set containing all plausible solutions. This solution may still not be unique (i.e., the subset defined by $(L_2)^2$ norm constraint may have more than one member). A solution with minimum $(L_2)^2$ can be obtained through optimizing \mathcal{E} defined as

$$\mathcal{E}(x) = \sum_{i=1}^6 (p_i(X) - y_i)^2 + \lambda \sum_{j=1}^2 x_j^2. \quad (2.4)$$

The minimization of $\mathcal{E}(x)$ can be carried out using conjugate gradient or other similar gradient search algorithms. However, in this case, the minimum $(L_2)^2$ norm solution is given by pseudo inverse solution to the problem $AX = Y$ where X is the solution vector and Y is the measurement vector and A is defined by mapping $y_i = \mathcal{P}_i(X)$. The solution is given by

$$X = (A^T A)^{-1} A^T Y \quad (2.5)$$

It should be stressed that the added condition(s) on the solution may only be enough to reduce the number of plausible solutions. Such narrowing of the solution set has considerable advantage. If one considers two state of 1) lack of knowledge and 2) unique identification of the solution as two extreme ends of a continuous scale, then in the absence of a unique solution, a smaller set of plausible solutions is preferred to a larger set of solutions. $(L_2)^2$ norm is one example of many types constraints that can be used to *more* uniquely define a solution. In the following, we present

	9	6	3	
	2	1	0	3
	4	3	2	9
	3	2	1	6

Figure 2.3: Minimum $(L_2)^2$ solution

the Minimum Support functional which is another type of constraint and has some interesting characteristics.

Minimum Support

In NDE applications where cracks and voids are the dominant expected source of signals, a minimum support approach might be ideal. To minimize support, we want to minimize the number of nonzero pixels, so, ideally, a penalty of 1 is associated to a nonzero pixel. In practice, due to noise and other reasons, pixel values may never be exactly zero. Hence, a pixel is not penalized if it is below a threshold ϵ . This means the support penalty function is $H(|x_i| - \epsilon)$. In the present work, since a gradient approach for minimization of support is used, the Heaviside function is not suitable since it has a zero or an ill-defined gradient. Instead an approximate form of the Heaviside function is used which has well-behaved gradient. One such function is

$$\mathcal{S}(x; \epsilon, \eta) = \frac{|x|^\eta}{|x|^\eta + \epsilon^\eta}. \quad (2.6)$$

where x is a pixel in the image, ϵ is the noise threshold and η is the steepness parameter of the function. It should be noted that as η approaches infinity, $\mathcal{S}(x)$ approaches a Heaviside function. (see Fig. 2.4).

If the minimum $(L_2)^2$ norm functional is replaced by the minimum support functional in the Eq. (2.4), the solution obtained will be more compact. The reason for the compactness of the minimum support solution versus that of $(L_2)^2$ is due to constant penalty for large pixel values. This is in contrast with the increasingly large penalties for larger pixels in the $(L_2)^2$ functional.

In cases where there are many degrees of freedom in the solution due to missing

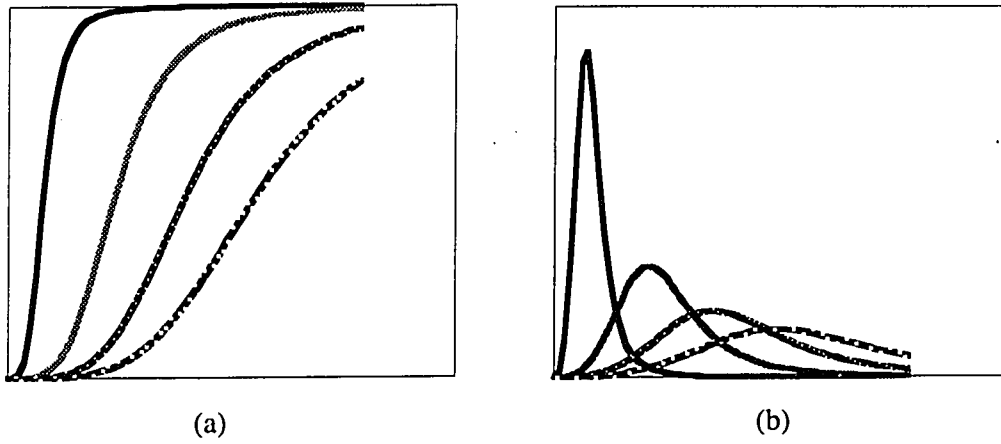


Figure 2.4: Minimum support: a) functional b) gradient of the functional, for different values of ϵ

	9	6	3	
	0	0	3	3
	9	0	0	9
	0	6	0	6

Figure 2.5: Minimum support solution

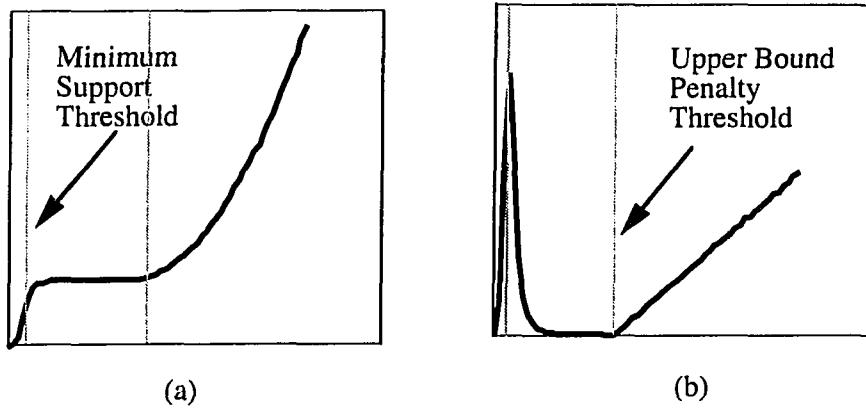


Figure 2.6: Minimum support: a) functional b) gradient of the functional, for different values of ϵ

	9	6	3	
	3	0	0	3
	3	3	3	9
	3	3	0	6

Figure 2.7: Minimum support solution with upper bound penalty $x_{th} = 3$

data, minimum support functional may not strongly affect the high pixel values. In those cases, it may be necessary to complement the minimum support functional by another functional to constrain high pixels. An example of such a constraint seeks an upper bound for the pixel values by adding penalty for pixel values above a specified threshold x_{th} .

$$\mathcal{F}(x) = \mathcal{S}(x; \epsilon_0, \eta_0) + \mathcal{S}(x; \epsilon_1, \eta_1) \left(\frac{x - x_{th}}{\epsilon_2} \right)^\beta \quad (2.7)$$

Function $\mathcal{S}(x; \epsilon_0, \eta_0)$ is a special case of $\mathcal{F}(x)$ for $\epsilon_1 = \infty$. In cases with high degrees of freedom in the solution, this additional constraint only affects the high pixel values without increasing the support. In the case at hand, we do not have many degrees of freedom in the solution. Hence, the solution using this functional with $x_{th} = 3$ as shown in Fig. 2.7 has smaller peaks at the expense of increased support. This solution is not as compact as the minimum support solution since a threshold is set at x_{th} beyond which pixels are penalized heavily. Hence, support of the minimum support solution has increased accordingly to reach a balance for the new condition. All pixel in the solution are equal to 3 which is purely a coincidence, however, the fact that there is no pixel greater than 3 is due to the heavy penalty given to pixels greater than 3. Note that, by counting the nonzero pixels, the support has increased from 3 to 6 which is a result of the balance between the support and the penalty for pixel values greater than threshold x_{th} . To see how the solution is affected by the value of x_{th} , we reduced the threshold from 3 to 2. The solution for this case is given in Fig. 2.8. The support has further increased to 9 to balance the penalty due pixels with values greater than 2.

	9	6	3	
	2.7	1.3	-1.0	3
	3.5	2.8	2.7	9
	2.8	1.9	1.3	6

Figure 2.8: Minimum support solution with upper bound penalty $x_{th} = 2$

Maximum Entropy Solution

The maximum entropy function has been used extensively in many areas of image and signal processing to supplement incomplete data inversions. Various forms of the functional has been used in different application, however, most conventional form of the functional is given as

$$e = |x| \log |x/x_0| \quad (2.8)$$

There have been many justifications for the use of the maximum entropy function from the aspect of information theory [11, 12]. In this work, however, we will view it only from a functional standpoint. The maximum entropy functional, unlike minimum support functional, it is unbounded while it is not as rapidly growing as the $(L_2)^2$ norm functional. The gradient of the maximum entropy functional is monotonically increasing which is similar to the $(L_2)^2$ norm functional than minimum support function which has a gradient with extremum point. Qualitatively speaking, it behaves in between the minimum support functional and $(L_2)^2$ norm functional.

The solution obtained using this functional is given in Fig. 2.10 using a small value for x_0 . The solution has many pixels around 1 which is a bias of this functional for $x_0 = 1$ since for values of x between 0 and x_0 there is a reward rather than a penalty. The functional is zero for $x = 0$ and $x = x_0$

Discussion

It is clear that choice of an appropriate functional depends on the physical problem at hand. Among other commonly used functionals is maximum entropy functional that has been used extensively in many areas of signal and image process-

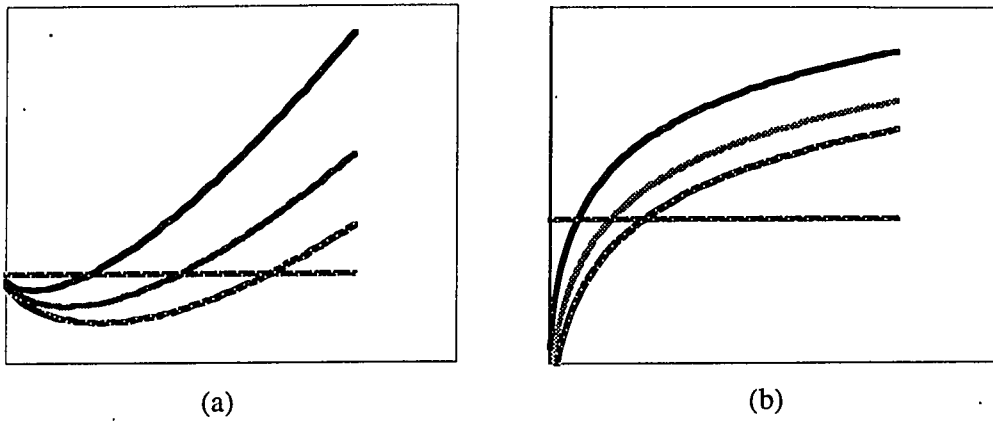


Figure 2.9: Maximum Entropy functional for different values of x_0

	9	6	3	
1.5				3
4.5				9
3				6

Figure 2.10: Maximum Entropy solution with a small x_0

ing. The difference between Maximum Entropy and Minimum Support functional is mostly in their behavior for larger arguments. The maximum entropy functional is unbounded while minimum support functional is bounded by 1 as argument approaches infinity. This is an important difference since it will pressure the large values in the solution downward. The minimum support functional, on the other hand, puts the greatest pressure on values in the transition region and leaves the higher values to adjust appropriately to minimize the inconsistency with the measurements. Convergence to a solution can be slow due to small gradients in most ranges of pixel value x (As seen in Fig. 2.4). In Fig. 2.4, it is observed that as ϵ varies for a fixed η , the peak of the gradient shifts. To speed the convergence, one may start the iteration with a large value of ϵ and gradually reduce it to the noise level. Numerous experiments have proved the effectiveness of this scheme. Results will be shown in the following chapters.

CHAPTER 3. FORWARD MODELLING OF ELASTODYNAMIC WAVE SCATTERING

In this chapter, a two-dimensional elastic forward algorithm is presented that utilizes the integral form for the equation of motion in the isotropic elastic medium. This approach is most suitable for cases where scattering from a small inhomogeneous body in an otherwise homogeneous background is sought. In this chapter, the forward problem is solved by discretizing the integral equations. The results from the numerical implementation are compared with the series solution to the scattering from a cylinder. Furthermore, the results obtained from the exact nonlinear model will be compared with results from linearized model (Born approximation). Finally, the equations for the motion for the acoustic medium is derived as a special case of the elasticity problem.

Introduction

The work on the integral equation approach to elastic wave scattering is motivated by the need to have an algorithm which would yield far field scattering from an object with ka less than 10. Differential equation methods (e.g., finite element and finite difference methods) have been used successfully in the past to model wave phenomena [24]. However, differential equation methods method are not inherently

suitable for cases where field is sought at large distances. This is due to the fact that differential methods require global discretization and hence are not efficient for such purposes. Much work has been carried out in making differential methods efficient in propagating the field in the homogenous medium beyond the scatterer itself (for example see [10]). Workers have proposed and implemented boundary matching techniques which utilizes the existing symmetry of the problem. In this work, we present a volume integral equation approach to solving the forward problem which will avoid the problems of boundary matching. The volume integral approach is optimum for cases where the scatterer is a small inhomogeneity in a homogeneous background. This method can be improved to efficiently handle the case of the homogeneous scatterer too. For example, application of the divergence theorem reduce the volume integral equation to a boundary integral formulation. One can envision an improved volume integral method which it adjusts itself to efficiently solve the scattering problem for a given scatterer. The adjustment can be regarded as choosing the best set of the basis functions to represent the field and the scatterer. One can show that the Boundary Element solution can be derived from a volume integral solution with appropriate basis functions. Further details on this topic is yet to be explored in the future.

Wave Motion in Elastic Media

The wave motion in a homogeneous isotropic elastic solid is governed by

$$\tau_{ij,j} + \rho\omega^2 u_i = 0 \quad (3.1)$$

where stress tensor τ_{ij} is given by

$$\tau_{ij} = \lambda \delta_{ij} u_{k,k} + \mu (u_{i,j} + u_{j,i}) \quad (3.2)$$

where λ and μ are the material Lamé constants and ρ is the mass density. The displacement u includes both shear (S-wave) and pressure wave (P-wave) motion. Generally, parameters ρ , λ and μ are not constant; indicating the material is inhomogeneous. If the medium is homogeneous everywhere except for a finite region of space, then it is beneficial to represent ρ , λ and μ as the sum of the constant background parameter and the variation due to the scatterer given as

$$\rho(x) = \rho_0 + \delta\rho(x) \quad (3.3)$$

$$\lambda(x) = \lambda_0 + \delta\lambda(x) \quad (3.4)$$

$$\mu(x) = \mu_0 + \delta\mu(x) \quad (3.5)$$

note that $\delta\rho$, $\delta\lambda$ and $\delta\mu$ are zero everywhere except for the scatterer.

The general solution to Eq. (3.1) in the presence of an incident displacement field u^{inc} can be represented in terms of the Green's functions $u_{i;j}^G(x|x')$ for the background medium with elastic parameters ρ_0 , λ_0 and μ_0 .

$$u_i(x') = u_i^{inc}(x') + \int u_{i;j}^G(x|x') s_j(x) dx \quad (3.6)$$

$$\begin{aligned} -s_i(x) = & \delta\lambda(x) u_{k,ki}(x) + \delta\mu(x) (u_{i,jj}(x) + \\ & u_{j,ii}(x)) + \delta\rho(x) \omega^2 u_i \end{aligned} \quad (3.7)$$

$$\tau_{ij:k,j}^G + \rho\omega^2 u_i^G : k = \delta_{ik} \delta(x - x') \quad (3.8)$$

The $s_j(x)$'s are seen to be "equivalent source" functions. If displacement $u_i(x)$ is known, using Eq. (3.6), the scattered displacement can be calculated anywhere in

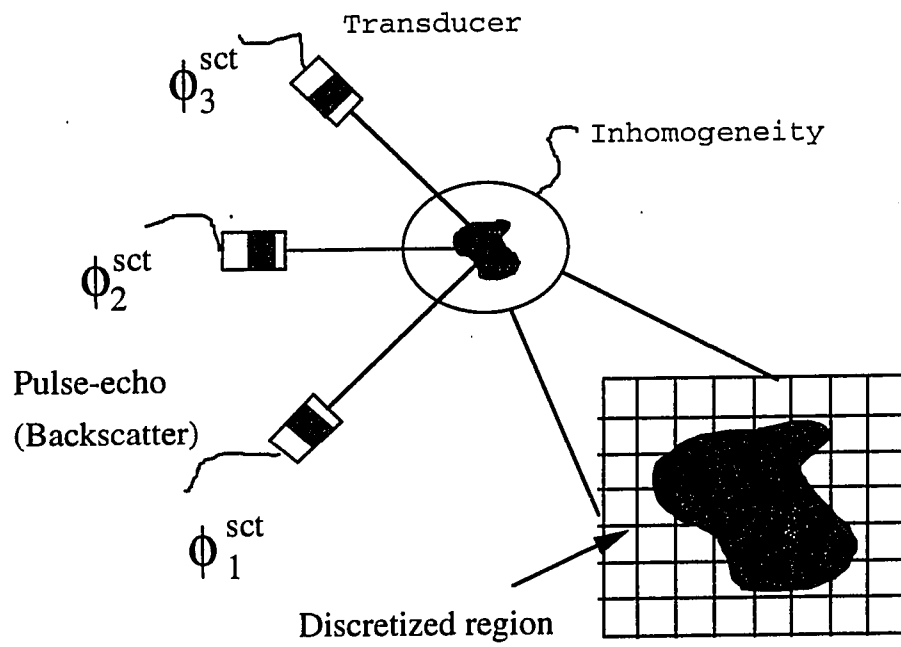


Figure 3.1: Forward scattering calculation from a small inhomogeneity

space. The displacement $u_i(x')$ can be obtained over the scatterer by solving the above equations. In order to solve for $u_i(x')$, we proceed to discretize the above integral equations. One method of solving volume integral equations is to project the solution onto a discrete basis set. The choice of the basis function is very important in obtaining a physically sensible solution. As it will be discussed further, if only far-field displacements are desired, the choice of basis function is not as crucial as when we are interested in displacements close to discontinuity regions. In the case at hand where functions and its derivatives are to be defined, a basis function should be chosen that is differentiable at least up to the order needed in s . A basis function like Gaussian-Sinc function is infinitely differentiable

$$b(x_1, x_2) = e^{-a^2(x_1^2 + x_2^2)} \text{Sinc}\left(\frac{\pi x_1}{\Delta x}\right) \text{Sinc}\left(\frac{\pi x_2}{\Delta x}\right) \quad (3.9)$$

where a is chosen such that it effectively limits the support of the basis function so as to limit the support of the numerical integration. The choice of Δx depends on the spatial bandwidth that is required to represent the function. Note that $b(x)$ behaves like a delta function as $\Delta x \rightarrow 0$.

$$\delta(x) = \lim_{x \rightarrow 0} b(x) \Delta x \text{Erf}\left(\frac{\pi}{2a}\right) \quad (3.10)$$

$u_i(x')$, $\delta\lambda(x')$, $\delta\mu(x')$ and $\delta\rho(x')$ may be expressed in terms of the basis functions as

$$u^i(x') = \sum_k u_i(x_k) b(x' - x_k) \quad (3.11)$$

$$\delta\lambda(x') = \sum_k \delta\lambda(x_k) b(x' - x_k) \quad (3.12)$$

$$\delta\mu(x') = \sum_k \delta\mu(x_k) b(x' - x_k) \quad (3.13)$$

$$\delta\rho(x') = \sum_k \delta\rho(x_k) b(x' - x_k) \quad (3.14)$$

By combining Eqs. (3.6) and (3.14), the following linear system of equation is obtained.

$$\sum_{\beta} \sum_j a_{i\alpha j\beta} u_{j\beta} = u_{i\alpha}^{inc} \quad (3.15)$$

or in matrix form

$$AU = U^{inc} \quad (3.16)$$

where $u_{i\alpha}$'s are vectors containing displacement components (Greek symbols refer to position index and Roman symbols refer to component). $a_{i\alpha j\beta}$'s are defined as

$$a_{i\alpha j\beta} = - \int \sum_k u_{j:k}^G(x_{\alpha}, y_{\alpha}; x, y) A_{ki}(x, y; x_{\beta}, y_{\beta}) \quad (3.17)$$

(x_{α}, y_{α}) and (x_{β}, y_{β}) correspond to locations α and β respectively, and $u_{i:j}^G$ is the Green function given by

$$u_{1:1}^{Gl}(r) = \frac{1}{\lambda k_l^2 4i} \left[-k_l^2 \frac{x_2^2}{r^2} H_0''(k_l r) - k_l \frac{x_1^2}{r^3} H_0'(k_l r) - k_l^2 H_0(k_l r) \right] \quad (3.18)$$

$$u_{1:2}^{Gl}(r) = u_{2:1}^{Gl}(r) = \frac{x_1 x_2}{4i \lambda k_l^2} \left[\frac{k_l^2}{r^2} H_0''(k_l r) - \frac{k_l}{r^3} H_0'(k_l r) \right] \quad (3.19)$$

$$u_{2:2}^{Gl}(r) = \frac{1}{\lambda k_l^2 4i} \left[-k_l^2 \frac{x_1^2}{r^2} H_0''(k_l r) - k_l \frac{x_2^2}{r^3} H_0'(k_l r) - k_l^2 H_0(k_l r) \right] \quad (3.20)$$

$$(3.21)$$

and A_{ij} 's involve the products of b_u and $\delta\lambda$, $\delta\mu$, and $\delta\rho$. These lengthy expressions are listed in the appendix. The above system of equations is solved either iteratively or by an exact inversion of matrix A . Matrix A is not a fully populated matrix and is

dominated by diagonal and subdiagonals. It is conceivable to avoid an exact inversion by exploiting the physics of the problem. In this work, we will not discuss techniques that can be applied and suffice to state that less interaction between the elements of the scatterer translates into a more diagonally dominant matrix.

The initial algorithm developed in this work employed the Gaussian-Sinc basis. The Gaussian-Sinc function efficiently represent any bandlimited function. However, in choosing a basis set, one has to balance the representation efficiency with the computation efficiency. Choosing the most efficient basis set may not be the best in terms of overall computation burden. The most efficient basis set can represent the function using fewest components, however, it might require more computation in calculating coefficients $a_{i\alpha j\beta}$ represented in Eq. (3.17). By choosing an appropriate basis set, it is possible to considerably improve the overall computation speed. In a problem where many forward calculation is necessary, as it is the case for iterative inversion algorithms, using a basis set with minimum computation demand is imperative. Hence, an alternative to Gaussian-Sinc basis function was chosen for the current algorithm to provide speed in forward modeling. The new approach assumes basis functions that yield finite difference formulation, hence, making it possible to evaluate integrals as a Riemann sum. A set of equations was obtained (see appendix for detail), as before, in terms of the unknown displacement field on the scatterer. Solution obtained from this model is compared with the series solution. It is observed that the result is as good as the previous solution which used Gaussian-Sinc basis functions. Due to computation efficiency, from here on, the alternative solution (using an implicit basis function) will be used.

In the following section, we present some results obtained using the developed

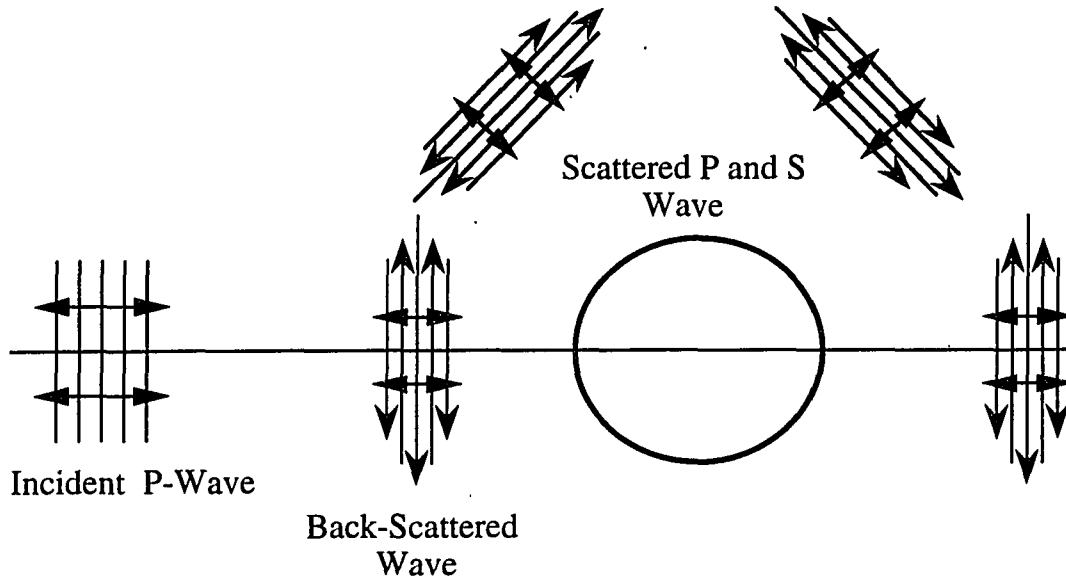


Figure 3.2: An incident plane wave impinging on a cylindrical scatterer

forward scattering model.

Algorithm Verification

The first step is to validate our forward model. To do this, the special case of scattering from a cylinder was considered. The solution for the scattering from a cylinder is available analytically in the form of a series solution because of separable geometry [27] (see appendix).

In the following, we consider the case of scattering from a steel cylindrical scatterer ($\rho = 7850 \text{ kg/m}^3$, $c_l = 5906 \text{ m/s}$ and $c_t = 3230 \text{ m/s}$) in a Silicon-Nitride ($\rho = 3250 \text{ kg/m}^3$, $c_l = 5906 \text{ m/s}$ and $c_t = 3230 \text{ m/s}$) background. The scattering is due to a plane pressure wave incident on the cylinder as shown in Fig. 3.2.

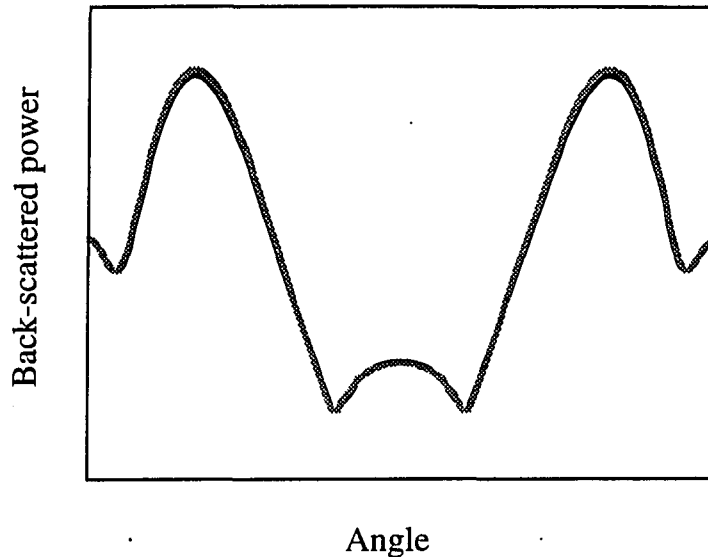


Figure 3.3: Total back-scattered power from a steel cylindrical scatterer in Silicon-Nitride with P-wave incidence: Comparison between the solutions from series method and the integral equation method for $ka = 0.6$ (e.g., a 30μ cross section at 20 Mhz)

In Fig. 3.3 the total back-scattered power calculated with the integral equation method is compared with the solution obtained using the series method. The integral equation result was obtained using a 11×11 discretization of the cylinder. The series solution was obtained using 12 terms in the series. There is very good agreement between the two solution as shown in Fig. 3.3 .

Now that we have verified the algorithm, we can use our forward algorithm to study other problems. For example, it is valuable to know how the scattering is affected by the sharpness of the transition boundary between the two medium. In Fig. 3.4a, the radial profile of three different rotationally symmetric scatterers are shown. The boundary of the scatterer in these scatterer varies from a sharp

boundary to a smooth Gaussian scatterer. The scattered power is plotted versus angle for $ka = 0.6$ for the case of steel scatterer in Silicon-Nitride as shown in Fig. 3.5a. The scattered power for this ka does not vary significantly from diffused boundary scatterer to the sharp boundary scatterer. However, by increasing ka the difference is more significant. The case of $ka = 1.5$ is shown in Fig. 3.5 (a 11×11 discretization was used to represent the cylinder in integral equation approach and 12 terms was used in the series solution).

Another interesting issue is testing how the exact nonlinear solution compares with the Born solution. Again the case of steel in Silicon-Nitride is considered. The backscattered power is plotted for series solution, nonlinear solution and the linearized Born solution. Figs. 3.6a, 3.6b, 3.6c, and 3.6d show the solutions for $ka = 0.3, 0.9,$ and 1.5 respectively. As the ka increases the accuracy of the Born result decreases. As seen in Fig. 3.5, where back-scattered power is shown for $ka = 1.5$, the difference between Born and exact solution is the largest (a 11×11 discretization was used to represent the cylinder in integral equation approach and 12 terms was used in the series solution).

It should be noted that the solution for the displacement can be used to calculate the induced voltage in a transducer. This is done using Auld's reciprocity theorem. Auld's reciprocity theorem (see appendix) states that given displacement and stress components U and T for a case where no flaw exists and U' and T' for a case where flaw exists, the voltage in the transducer can written as

$$\delta V = \frac{i\omega}{4P} \int (U \cdot T' - U' \cdot T) dS \quad (3.22)$$

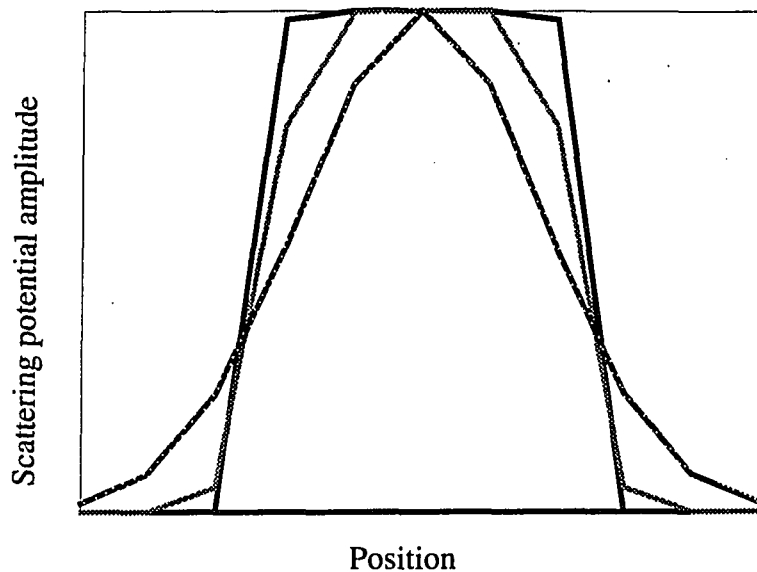


Figure 3.4: Profile of the scatterers ranging from sharp to smooth boundary

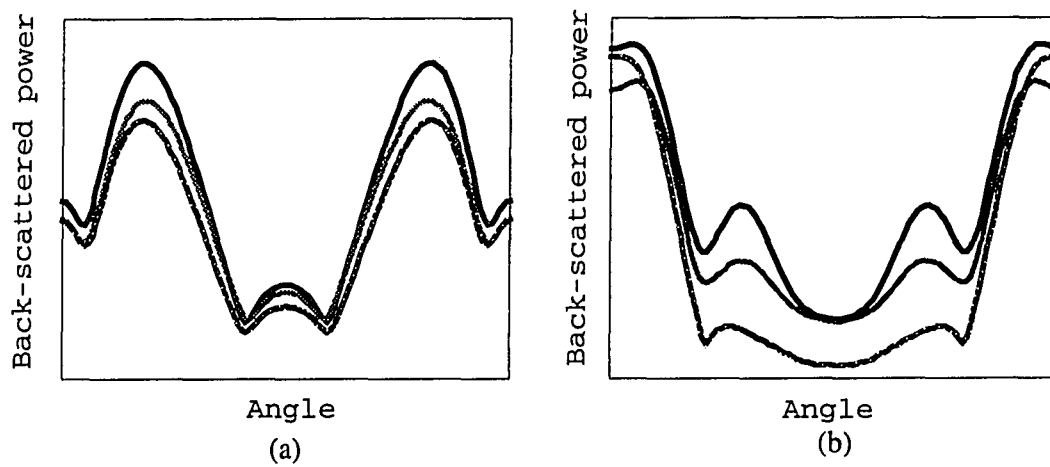


Figure 3.5: Comparing backscattered power from cylindrical scatterers a) back-scattered power for $ka = 0.6$. b) back-scattered power for $ka = 1.5$

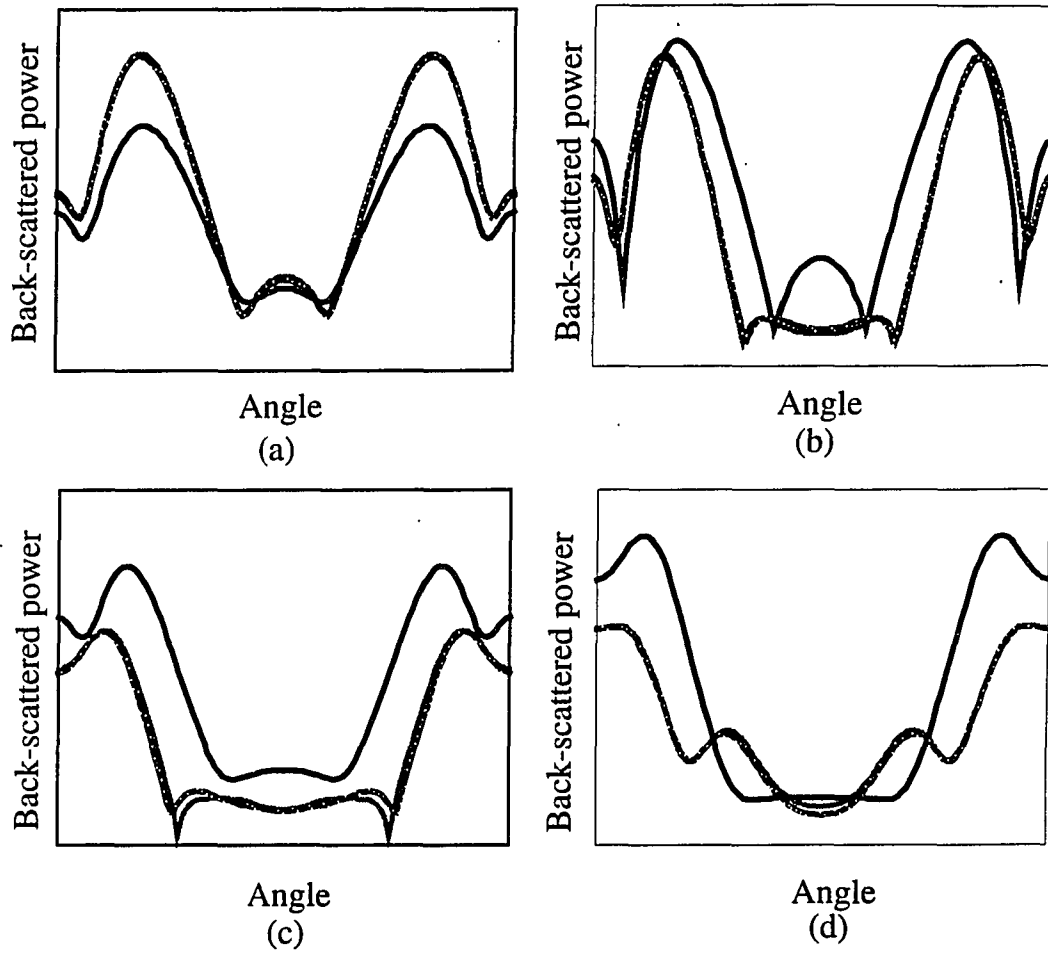


Figure 3.6: Comparing the series solution (grey) with the integral equation solutions with (solid)/without (dotted) Born approximation: a) $ka = 0.6$ b) $ka = 0.9$ c) $ka = 1.2$, and d) $ka = 1.5$

Reducing Elastic to Acoustic

In the case of an elastic scatterer in an acoustic background, the solution can be represented by a scalar quantity ϕ where $u = \nabla\phi$, since the displacement in acoustic medium is irrotational. However, it is more common to refer to pressure inside fluids; for this reason, in the following, we start from the elastic equations of motion and derive the equation for the pressure $p = -\lambda\nabla \cdot u$.

$$\tau_{ij,j} + \rho\omega^2 u_i = 0 \quad (3.23)$$

hence

$$(\tau_{ij,j} + \rho\omega^2 u_i),_i = 0 \quad (3.24)$$

knowing $p = -\lambda u_{k,k}$

$$p_{,kk} + (\omega/c_l)^2 p = -\rho_i \omega^2 u_i \quad (3.25)$$

furthermore, if we assume $\rho_{,i} = 0$, we obtain the Helmholtz equation for the pressure inside the fluid. Furthermore, by representing slowness $1/c_l^2 = 1/c_{l0}^2 - 1/\delta c_l^2(x)$, the volume integral equation becomes

$$p(x', \omega) = p^{inc}(x', \omega) + \int v(x') p(x', \omega) G(x'|x) dx' \quad (3.26)$$

where $v(x) = 1/\delta c_l^2(x)$ and G is the Green function for equation

$$\nabla^2 G(x|x') + k^2 G(x|x') = \delta(x - x'). \quad (3.27)$$

In many applications, it is desired to know the scattering from an elastic object immersed in an acoustic medium (e.g. water). Considering the fact that an ideal fluid can be assumed an elastic object with $\mu = 0$, the approach to the problem becomes clear. However, one should proceed with caution since by setting $\mu = 0$ we assume

a zero velocity of propagation for the shear component of the wave in the acoustic medium. The complexity is due to the fact that displacements can be discontinuous in directions tangent to the interface. Since the source function in Eq. (3.6) contains terms including derivatives of displacement makes the problem ill-posed in nature and could adversely effect the stability of the solution. In the following, two cases of scattering from an elastic scatterer in an acoustic medium and an acoustic scatterer in an elastic medium is considered.

The case of an elastic scatterer in an acoustic medium is more interesting and also is more commonly observed. Since the acoustic medium can not support shear displacement, at the boundary of the scatterer, the displacement tangent to the interface can be discontinuous. This discontinuity can introduce numerical instabilities. For the case of elastic scatterer in an acoustic medium, the scattered displacement can be written in terms of the Green's function for the acoustic background and the source function carries the information about the elastic scatterer. The approach to solving the problem follows that of scattering by elastic solid in an elastic medium.

The Green's functions for displacement in which case can be derived as a special case from Eqs. (3.18), (3.19), (3.20).

$$G_{1:1}^l(r) = \frac{1}{\lambda k_l^2 4i} \left[-k_l^2 \frac{x_2^2}{r^2} H_0''(k_l r) - k_l \frac{x_1^2}{r^3} H_0'(k_l r) - k_l^2 H_0(k_l r) \right] \quad (3.28)$$

$$G_{1:2}^l(r) = G_{2:1}^l(r) = \frac{x_1 x_2}{4i \lambda k_l^2} \left[\frac{k_l^2}{r^2} H_0''(k_l r) - \frac{k_l}{r^3} H_0'(k_l r) \right] \quad (3.29)$$

$$G_{2:2}^l(r) = \frac{1}{\lambda k_l^2 4i} \left[-k_l^2 \frac{x_1^2}{r^2} H_0''(k_l r) - \right]$$

$$k_l \frac{x^2}{r^3} H_0'(k_l r) - k_l^2 H_0(k_l r)] \quad (3.30)$$

$$(3.31)$$

The voltage in the transducer can be represented in terms of the pressure field p using Auld's reciprocity relationship given by

$$s(x, \omega) = \int p(x', \omega) p^{inc}(x', \omega) v(x') dx'. \quad (3.32)$$

The voltage s at different positions x and different frequencies ω can be used as the measurement for the inversion process.

CHAPTER 4. MINIMUM SUPPORT LINEARIZED ACOUSTIC INVERSION

Introduction

In this chapter, the linearization of the inversion problem is introduced. The linearized problem is the basis of common imaging techniques such as SAFT (Synthetic Aperture Focusing Technique) and diffraction tomography. The discussion that follows only considers the acoustic problem to limit complexity, and keep conceptual focus on the issue of limited data inversion.

Model For The Forward Problem

Auld's reciprocity theorem states that the voltage in the transducer due to a scatterer is given by (see previous chapter and appendix for a detailed derivation)

$$s(\omega) = -\frac{i\omega}{4\rho\Gamma} \int \left(\frac{1}{c_0^2} - \frac{1}{c(x)^2} \right) p(x) p^{inc}(x) dv \quad (4.1)$$

where ω is the frequency, ρ is the density of the scatterer and background, Γ is the incident power, c_0 and $c(x)$ are velocity of the background and the scatterer respectively, $p^{inc}(x)$ is the pressure when the scatterer is not present, and $p(x)$ is the pressure when the scatterer is present. $p(x)$ can be calculated from the following

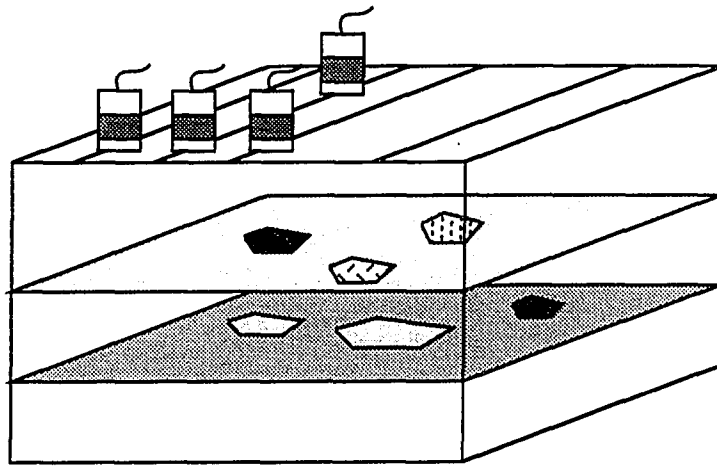


Figure 4.1: Ultrasonic probing: volumetric image may be obtained using a two-dimensional scan

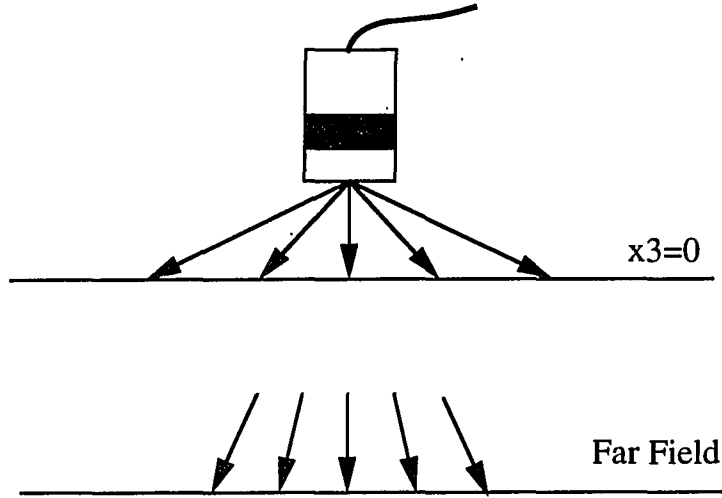


Figure 4.2: Incident field in the far-field

integral equation.

$$p(x') = p^{inc}(x') + \omega^2/c_0^2 \int p(x)v(x)G(x|x')dx \quad (4.2)$$

where $G(x|x')$ is the Green function and $v(x) = c_0^2/c(x)^2 - 1$. The fact that $p(x)$ depends on the scatterer makes Eq. (4.1) nonlinear with respect to the unknown $v(x)$. Assume a weak scatterer where $c^2(x) \approx c_0^2 + \epsilon c_1^2(x)$ and $p(x) \approx p_0(x) + \epsilon p_1(x)$. Expanding Eq. (4.1) yields the linear integral equation for $v(x)$ as the leading order written as

$$s(\omega) = \int_{\mathcal{V}} p^{inc}(x, \omega)^2 v(x) dx \quad (4.3)$$

Given a transducer, incident field at any point in space can be represented as (see Fig. 4.2)

$$p^{inc}(x_1, x_2, x_3) = \int \hat{p}(k_1, k_2) e^{k_1 x_1 + k_2 x_2 + \sqrt{k^2 - k_1^2 - k_2^2} x_3} \quad (4.4)$$

where $\hat{p}(k_1, k_2)$ is called the spatial frequency spectrum of the transducer and is simply the spatial Fourier transform of the field $p(x)$ at depth $x_3 = 0$. For large values of x_3 , incident field may be asymptotically evaluated in closed form (see appendix) given by

$$p^{inc}(x_1, x_2) = \frac{2\pi k x_3}{r^2} \hat{p}^{inc}(kx_1/r, kx_2/r) e^{j\omega r/c} \quad (4.5)$$

Hence, the output voltage of transducer located at a position $(x'_1, x'_2, 0)$ is given by

$$s(x'_1, x'_2, \omega) = 4\pi^2 k^2 \int_{\mathcal{V}} \hat{p}^2(kx_1/r, kx_2/r) v(x_1, x_2, x_3) \frac{e^{j2\omega r/c}}{r} \quad (4.6)$$

where $r = \sqrt{(x'_1 - x_1)^2 + (x'_2 - x_2)^2 + x_3^2}$. Assuming a point source transducer (i.e. $p(kx_1, kx_2) = 1$) at a distance r in the far field the voltage can be written as

$$s(rn, \omega) = C(\omega, r) \hat{v}(2\omega n/c) \quad (4.7)$$

where $C(\omega, r)$ is a complex constant. The exact expression for this constant can be known as shown in the next chapter. However, in practice it is determined by experiment and includes all temporal and spatial behavior of data collection system. where ω is the frequency and n is the unit direction vector. $v(x_1, x_2, x_3)$ can be obtained exactly through a Fourier transform if $v(2\omega n/c)$ is known for all ω and directions. If the scatterer is real-valued, it can be reconstructed exactly using measurements on a hemisphere (2π radian coverage of k -space) because the other half is complex conjugate of the known half. Usually, due to finite temporal bandwidth and finite aperture, it is not possible to obtain a complete measurement set. As a consequence, the result of inversion is not unique and obtained solution depends on the algorithm which was used for the inversion. As discussed in Chapter II, most algorithms have implicit biases toward certain solutions. In the following sections, we utilize the inversion methods discussed in Chapter II. First results of inversion with minimum

support will be presented and it will be compared with the results from minimum $(L_2)^2$ norm inversion. In one case, a maximum entropy solution is also provided.

A Two Dimensional Example

In this section, we use a two dimensional example to demonstrate the effectiveness of the minimum support inversion. The forward scattering model for the two dimensional case is developed in Chapter III (for a detailed SAFT derivation see appendix). As shown in the previous section, the relationship between the voltages observed by the transducers $s^m(x_1, t)$ and the scatterer potential $v(x_1, x_2)$ can be written as

$$\hat{v}^m(2\omega/c \cos \theta, 2\omega/c \sin \theta) = s^m(\omega, \theta) \quad (4.8)$$

where $s^m(\omega, \theta)$ the voltage at the output of the transducer and $\hat{v}^m(2\omega/c \cos \theta, 2\omega/c \sin \theta)$ is the Fourier transforms of the scatterer $v(x_1, x_2)$. For a given set of measurements $s^m(x_1, t)$, $\hat{v}^m(2\omega/c \cos \theta, 2\omega/c \sin \theta)$ can be calculated. A solution may be obtained by evaluating the two dimensional Fourier Transform of $\hat{v}^m(k_1, k_2)$. For a finite temporal bandwidth and limited angular view, space (k_1, k_2) is only partially known (see Fig. 4.3). As discussed earlier, the solution is not uniquely defined. By assuming zeros for regions in the k -space where measurement does not exist we obtain the minimum $(L_2)^2$ norm solution (see chapter 2). This a consequence of parseval's theorem. An $(L_2)^2$ norm solution has many artifacts in the form of negative and positive peaks. Furthermore the $(L_2)^2$ norm solution is, almost always, unphysical because this solution is obtained by assuming zeros for the missing measurements which is rarely the case in practice. To understand the exact relationship between our obtained solution and the exact solution, let's define a function $\psi(k_1, k_2)$ such

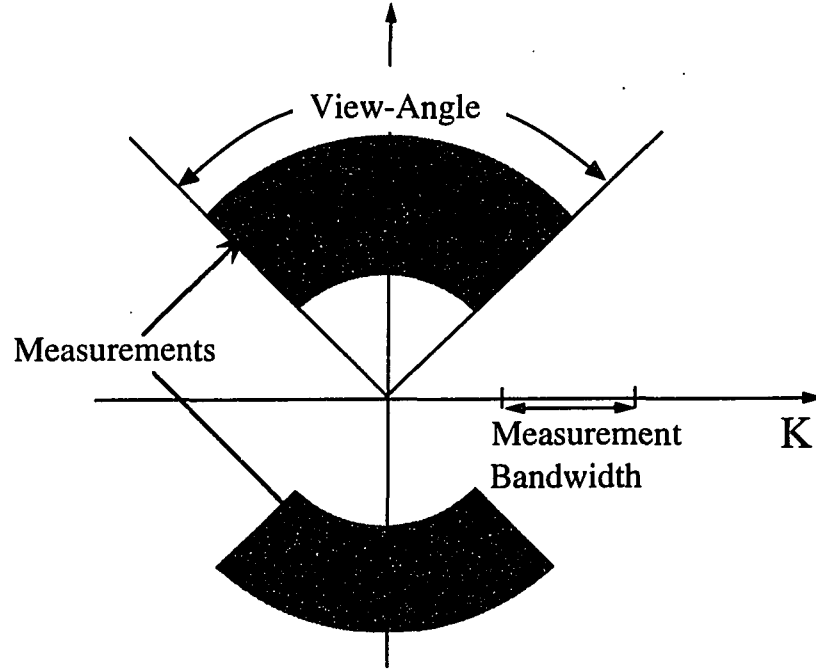


Figure 4.3: An example of data coverage in the k -space using a limited-view-angle pulse-echo system

that $\psi(k_1, k_2) = 1$ for all (k_1, k_2) where a measurement is available and $\psi(k_1, k_2) = 0$ otherwise. Using $\psi(k_1, k_2)$

$$\hat{v}^m(k_1, k_2) = \psi(k_1, k_2)\hat{v}(k_1, k_2) \quad (4.9)$$

or

$$v^m(x_1, x_2) = \hat{\psi}(x_1, x_2) \otimes v(x_1, x_2) \quad (4.10)$$

where \otimes is the two-dimensional convolution operation.

It is interesting to note that if $\psi^T(k_1, k_2) = 1 - \psi(k_1, k_2)$ then $\psi^T(k_1, k_2)\psi(k_1, k_2) = 0$. So if we consider a vector $g_\psi(x_1, x_2) = \psi^T(x_1, x_2) \otimes g(x_1, x_2)$ then adding

$g_\psi(x_1, x_2)$ to $v(x_1, x_2)$ does not change the measurements. This is because

$$\hat{\psi}(x_1, x_2) \otimes (v(x_1, x_2) + g_\psi(x_1, x_2)) = \hat{\psi}(x_1, x_2) \otimes v(x_1, x_2) + 0 \quad (4.11)$$

This is a very useful result since now we can optimize the support functional $\mathcal{S}(v)$ by correcting $v(x_1, x_2)$ by $\hat{\psi}(x_1, x_2) \otimes g(x_1, x_2)$ where $g(x_1, x_2)$ is the gradient of the minimum support functional without worrying about the consistency with the measurement as that is preserved by definition. In the discretized form, the minimum support functional is written as

$$\mathcal{S}(v) = \sum_i \sum_j \frac{|v(i, j)|^\eta}{|v(i, j)|^\eta + \epsilon^\eta} \quad (4.12)$$

If $g = \hat{\psi} \otimes \nabla \mathcal{S}$, then a new solution $v_{k+1}(x_1, x_2)$ can be written as

$$v_{k+1}(i, j) = v_k(i, j) + \gamma g(i, j) \quad (4.13)$$

where γ is found by a line-minimization in the direction of vector g .

Note that due to the nonuniformity of measurement sample location in the (k_1, k_2) space, FFT can not be used for transformation between the k -space and x -space. It is possible to use the discrete Fourier transform, however, it is not very efficient. Numerical implementation can be made more efficiently by using FFT if the sampled data is first resampled over a uniform grid. This can be done by resampling a new measurement function defined as

$$v^{mg}(k_1, k_2) = v^m(k_1, k_2) \otimes u(k_1, k_2) \quad (4.14)$$

This method was implemented, however, convergence was extremely slow and a solution could not be obtained. We believe a modified version of this technique can

be used successfully to yield inversions with great efficiency. The results which are presented in this chapter are obtained by gradient search using unfiltered gradients. In other word, we allow some discrepancy between measurements and the solution in the optimization process.

The Support Minimized Inversion

A minimum support inversion is obtained by minimizing the penalty function \mathcal{E} defined as

$$\mathcal{E} = \sum_i (d_i - d_i^m)^2 + \sum_j \mathcal{S}(x_j) \quad (4.15)$$

where d_i is the i_{th} measurement obtained through the forward model, d_i^m is the i_{th} measurement, and x_j is the j_{th} pixel and $\mathcal{S}(x_j)$ is the minimum support functional as defined in the previous section.

The choice of measurement d_i is important in reduction of unnecessary computation. Instead of choosing time-domain signal as the measurement, it is computationally more efficient to reduce all available time-signals by taking $s(x', t)$ into a uniform grid of $\hat{s}(k)$. This will significantly reduce the number of measurements without throwing away any important information. The main reason for the reduction is the fact that time signals have a non-uniform density of information in the k -plane. This is evident by transforming the time signals collected at all direction into the k -plane. It is seen that near zero spatial frequency there is a cluster of data while as k increases data points are located more sparsely. Assuming a size constraint of Δx is placed on the object, k -space data spaced more closely than $1/\Delta x$ is redundant information, as dictated by the sampling theorem. By resampling data on a uniform grid with spacing $1/\Delta x$, the redundancy can be eliminated. When noise is present,

the resampling performs an averaging of data which improves the signal to noise ratio.

In the following, two sets of results are presented. For the first case, a *crescent* shape object is considered and inversion is presented using limited bandwidth and limited-view-angle data. In the second case a square scatterer is considered and results are presented for limited bandwidth and limited view-angle using minimum support functional with a maximum ceiling constraint.

Fig. 4.4 shows the true scatterer which is in the shape of a crescent. The $(L_2)^2$ norm solution is shown in Fig. 4.5a using a 150 degree view-angle and $1 < ka < 6$. Fig. 4.5b shows the minimum support solution. By comparing the two image, it is clear that the minimum support solution is much closer to the original object than the $(L_2)^2$ solution. The artifacts in the form of negative and positive side-lobes and blurriness of the $(L_2)^2$ norm solution is expected based on our experience from results discussed in chapter II. In fact, by reducing the amount of available data we should observe a steady degradation of the $(L_2)^2$ norm solution. This is because the $(L_2)^2$ norm assumes zero for unmeasured regions of k -space which is highly unlikely in the case of a "real-world" scatterer. The minimum support functional on the other hand tries to extrapolate the unknown measurements such that the scatterer has the smallest volume (compact support). Results shown in Figs. 4.5a, Figs. 4.5b, Figs. 4.6a, and 4.6b clearly demonstrate this point.

The objective of the second experiment is to see the effects of minimum support functional on the solution. The scatterer is a square as shown in Fig. 4.7a and simulated data was generated for a 90 degree view-angle and $1 < ka < 6$. The $(L_2)^2$ norm solution is shown in Fig. 4.7b. The result is blurred and there are strong

negative side-lobes in the solution. In Fig. 4.8a, the minimum support solution with no amplitude constraint is presented. The support is considerably smaller than that of the $(L_2)^2$ norm solution. As it was discussed in chapter II, minimum support functional does not influence high pixel values, hence making it possible for high pixel value to take any value as long as they are consistent with the measurements. In cases where data is severely limited, as it is for the case at hand, the degree of the freedom for high pixel values is relatively high. This makes it desirable to define an additional constraint for high pixel values. An example of such functional is the minimum support functional with a maximum amplitude penalty. This functional was introduced in chapter II and its behavior was studied. Figs. 4.8b, 4.9a, and (4.9b) show results of inversion using parameters $x_{th} = 1.1, 1.0, 0.5$ respectively. It is seen from these results that by bringing the threshold x_{th} lower the high pixel values decrease without any change in measurement error or the support until the x_{th} goes below what was the actual peak in the scatterer. For the case of $x_{th} = 0.5$ the support starts to increase so as to reduce the penalty for the high pixel values. It should be noted that as x_{th} approaches ϵ the solution will approach the $(L_2)^2$ norm solution.

Finally, we conclude this section by presenting the maximum entropy solution to the problem of the box scatterer with 90 degree view-angle and limited $1 < ka < 6$. Fig. 4.10a shows a maximum entropy inversion of the box with entropy function defined as

$$\mathcal{S}(x_i) = x_i \log|x_i| \quad (4.16)$$

The solution resembles that of the $(L_2)^2$ norm solution. The negative side-lobes and blurrieness which is characteristic of $(L_2)^2$ norm solutions is present in the mem

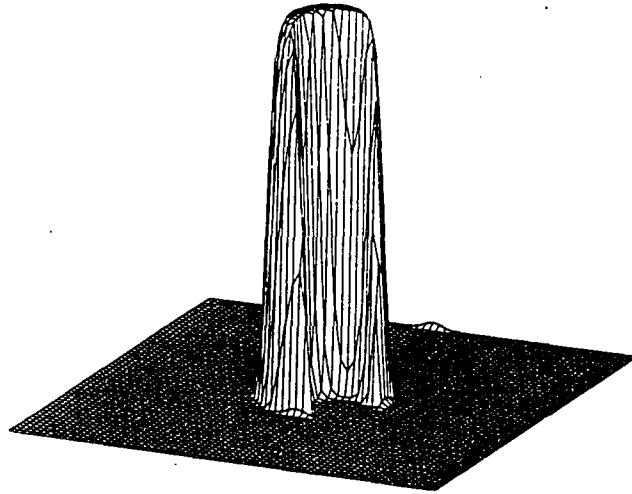
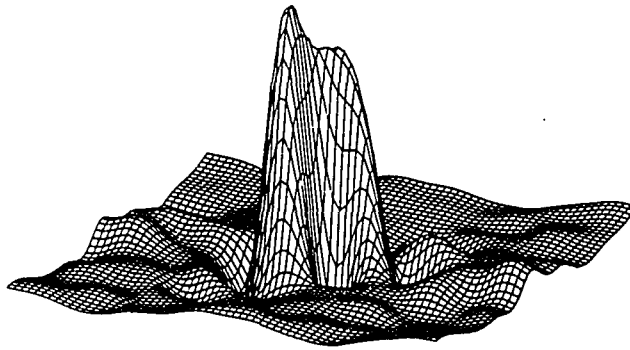
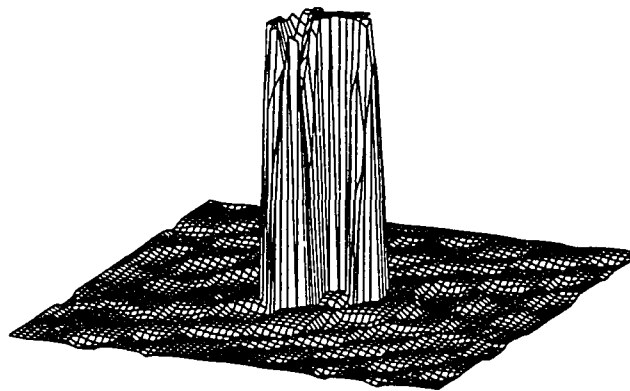


Figure 4.4: Case 1: Original object (min=0.0, max=1.0)

result. This is expected from our previous argument in Chapter II stating that mem solution behaves much like $(L_2)^2$ norm solution while being closer to the minimum support solution. Sometimes mem is used in combination with positivity constraints. Fig. 4.10b shows this solution which was obtained by optimizing mem function with additional quadratic penalty for negative pixels. This solution is practically (to the specified tolerance) is all positive. Although this solution is closer to the original scatterer, it is still blurred due to the high penalty for high pixels. We conclude this chapter, by restating that in the absence of any *a priori* information all of the above solutions are equally valid, however, if one is searching for the most compact object, then support minimized inversion provides the best solution.

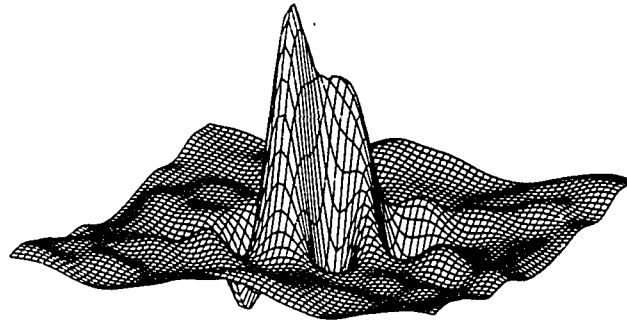


(a)

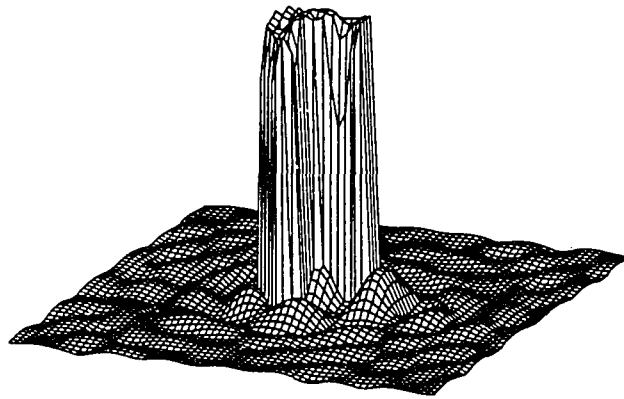


(b)

Figure 4.5: Inversion result using 150 degree view-angle and bandwidth $1 < ka < 6$
a) using $(L_2)^2$ norm (min=-0.26 max= 0.95) and b) using the minimum support functional (min=0.0 max= 1.0)

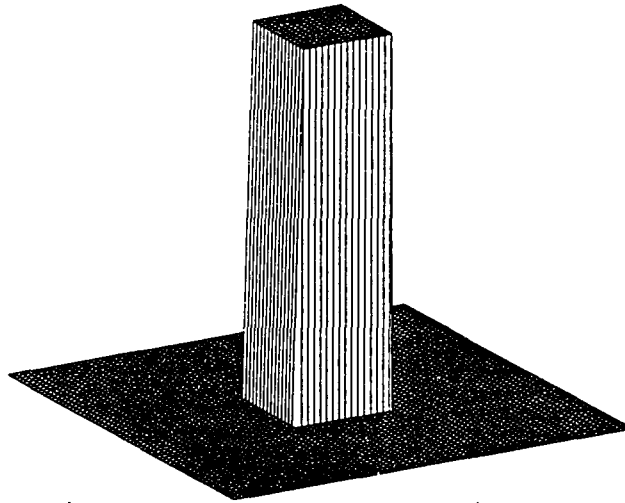


(a)

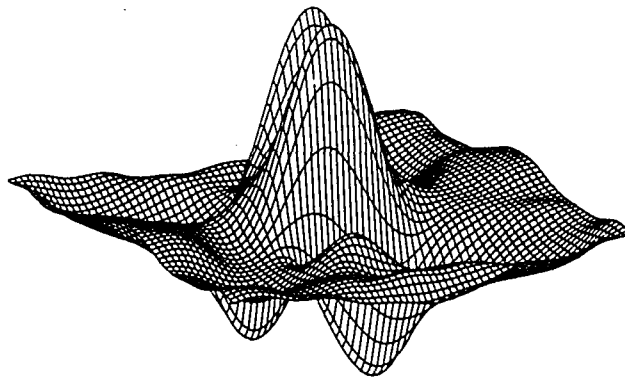


(b)

Figure 4.6: Inversion result using 120 degree view-angle and bandwidth $1 < ka < 6$
a) using $(L_2)^2$ norm (min=-0.29 max= 0.86) b) using the minimum
support functional (min=0.0 max= 1.0)

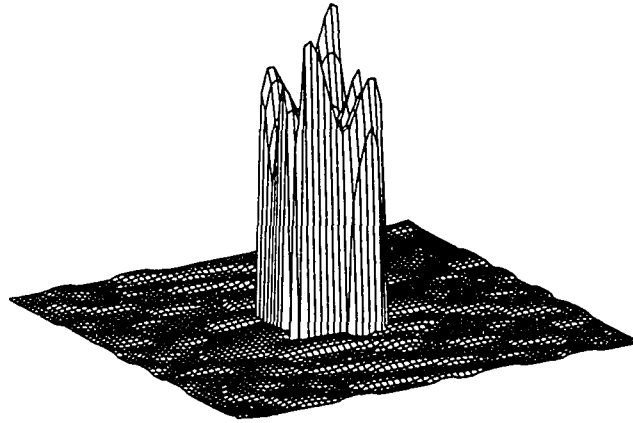


(a)

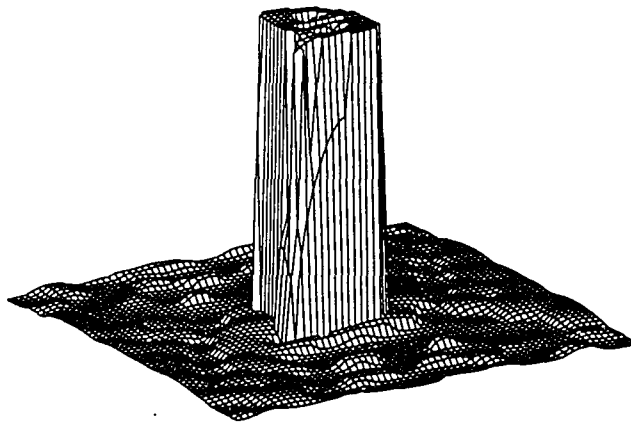


(b)

Figure 4.7: Case 2: a) Original scatterer (min = 0.0, max = 1.0), b) $(L_2)^2$ norm reconstruction of the scatterer using 90 degree view-angle and bandwidth $1 < ka < 6$ (min = -0.37, max = 0.54)

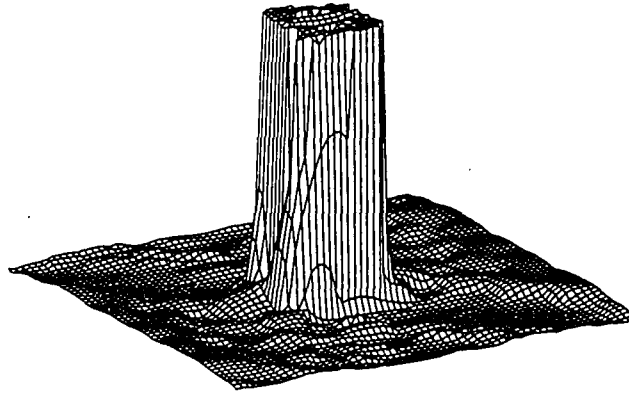


(a)

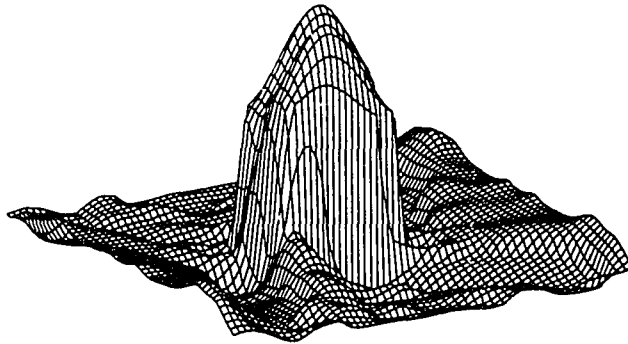


(b)

Figure 4.8: Inversion result using 90 degree view-angle and bandwidth $1 < ka < 6$ with the minimum support functional: a) with no amplitude constraint (min=0.0, max= 2.0), b) with amplitude constraint at $x_{th} = 1.1$ (min=0.0, max=1.12)

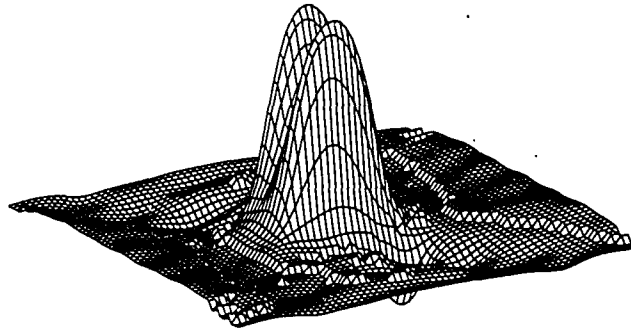


(a)

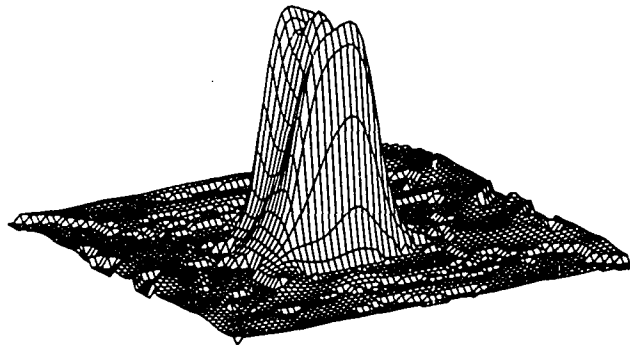


(b)

Figure 4.9: Inversion result using 90 degree view-angle and bandwidth $1 < ka < 6$ with the minimum support functional: a) with amplitude constraint at $x_{th} = 1.0$ (min=0.0, max=1.0) b) with amplitude constraint at $x_{th} = 0.5$ (min=0.0, max=0.87)



(a)



(b)

Figure 4.10: Inversion result using 90 degree view-angle and bandwidth $1 < ka < 6$
a) using maximum entropy functional (min=-0.34 max= 1.12) b) using
the minimum support functional (min=0.0 max= 1.24)

CHAPTER 5. SUPPORT MINIMIZED NONLINEAR ACOUSTIC INVERSION WITHOUT ABSOLUTE PHASE

Introduction

In this chapter, the application of support minimization to non-linear inversion of incomplete acoustic scattering data is presented. Similar to the inversion scheme in the previous chapter, the inversion scheme presented here utilizes a variational approach based on repeated application of a forward scattering algorithm. However, the forward scattering algorithm is not linearized. Even when a more explicit means for expressing the inverse mapping is available, the need to appropriately constrain the underdetermined incomplete data inversion will remain unchanged. Since optimization of the employed non-linear functionals requires an iterative procedure, the repeated application of the forward scattering algorithm does not present a significant increase in algorithm complexity. Indeed, the support minimization and implicit inverse mapping are carried out simultaneously by treating agreement with the measured data as an additional *a priori* condition to be optimized.

The problem considered here is the two-dimensional acoustic backscatter problem for which a broadband pulse with a plane wavefront insonifies a scattering object, and scattering data is collected at a large distance in the backscatter direction (i.e., in the direction of the source of the incident pulse). In the examples shown here,

the data to be inverted is limited in both collection angle and temporal frequency bandwidth. The measurement space in this example is the (θ, ω) plane, where θ is the observation (and incidence) angle and ω is time-harmonic frequency. The object space is the (x_1, x_2) spatial coordinate plane. The forward mapping in this problem maps the scattering object onto the scattered field measured at a large distance.

Forward Model

The scattering problem is governed by

$$\phi(x', \omega) + k_0^2 \int_V \phi(x, \omega) g(x) \phi^G(x|x', \omega) dx = \phi^{inc}(x', \omega) \quad (5.1)$$

where $\phi^{inc}(x, \omega)$ represents the incident pulse as a function of position x , and temporal frequency ω , $\phi(x, \omega)$ represents the total wavefield in the medium (incident plus scattered pulse), and $k_0 = \omega/c_0$ is the wavenumber of the host medium having constant acoustic velocity c_0 . It is assumed that the scattering object is contained within a closed volume V , in which the acoustic velocity $c(x)$ is a non-constant function of x . The scattering object $g(x)$ is defined as

$$\begin{aligned} g(x) &= \left(\frac{c_0}{c(x)}\right)^2 - 1 \\ &= \left(\frac{k(x)}{k_0}\right)^2 - 1. \end{aligned} \quad (5.2)$$

The Green function $\phi^G(x|x', \omega)$ is written

$$\phi^G(x|x', \omega) = \frac{1}{4i} H_0^1(k_0|x - x'|) \quad (5.3)$$

where H_0 is the zero order Hankel function of the first kind. In this work, an incident plane wave pulse is assumed, written

$$\phi^{inc}(x, \omega) = e^{ik_0 n(\theta) \cdot x} \quad (5.4)$$

where $n(\theta)$ is a unit vector pointing in the direction of incidence. Eq. (5.1) can be interpreted as a second kind integral equation for the total wavefield $\phi(x, \omega)$ when $x' \in V$. The measured data is received at a large fixed distance r outside V in the backscatter direction $-n(\theta)$. The measured data is therefore represented by rewriting Eq. (5.1) as

$$d(\theta, \omega) \equiv \phi^{sc}(-rn(\theta), \omega) = -k_0^2 \int_V \phi(x, \omega) g(x) \phi^G(x | -rn(\theta), \omega) dx \quad (5.5)$$

The forward mapping in this problem maps the scattering object $g(x)$ onto the measured data $d(\theta, \omega)$. This is performed computationally by first solving Eq. (5.1) as an integral equation for the total wavefield $\phi(x, \omega)$ over V for a given incident field $\phi^{inc}(x, \omega)$ and scatterer $g(x)$, then evaluating Eq. (5.5) to determine the data $d(\theta, \omega)$ at the measurement positions. The forward mapping is seen to depend linearly on the incident field $\phi^{inc}(x, \omega)$, but non-linearly on the scattering object $g(x)$, since the total field $\phi(x, \omega)$ obviously depends on $g(x)$. The desired inverse mapping is likewise non-linear.

Due to the non-linearity of the problem, it is difficult to state *a priori* what constitutes a complete set of measured data. However, insight into this question is provided by the examination of the linearized approximation of the inverse mapping (Born inversion) [33, 8] (a similar result is obtained independently in Chapter IV). Using the far-field approximation of the Green function

$$\phi^G(x | rn(\theta), \omega) \approx C(\omega, r) e^{-ik_0 x \cdot n(\theta)} \quad (5.6)$$

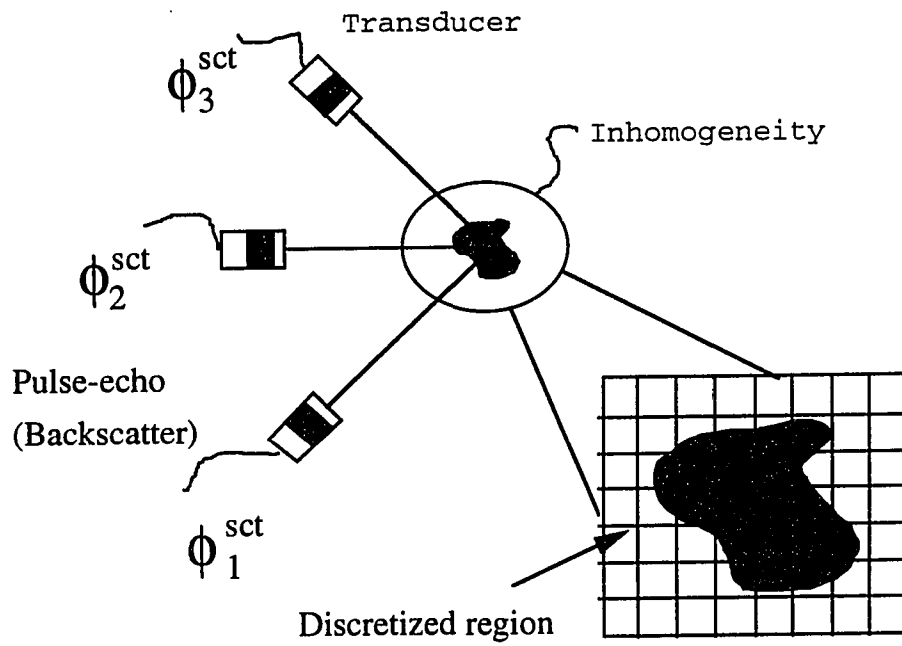


Figure 5.1: Acoustic back-scatter measurement.

$$C(\omega, r) = \frac{k_0^{3/2}}{\sqrt{\pi r}} e^{ik_0 r + ik_0 \pi/4} \quad (5.7)$$

in Eq. (5.5), the measured data ϕ^{sc} is expressed

$$\phi^{sc}(-rn(\theta), \omega) \approx C(\omega, r) \int \hat{\phi}(k_0 n(\theta) - \gamma, \omega) \hat{g}(\gamma) d\gamma \quad (5.8)$$

where $\hat{\phi}$ and \hat{g} are the spatial Fourier transforms of ϕ and g . The inversion is linearized by neglecting the scattered field contribution to the total wavefield, in which case $\phi = \phi^{inc}$. Using the incident field of Eq. (5.4), the Born inversion is expressed

$$\phi^{sc}(-rn(\theta), \omega) \approx C(\omega, r) \hat{g}(2\omega/c_0 n(\theta)) \quad (5.9)$$

In examining Eq. (5.9), a number of conclusions regarding data completeness are evident for the linearized inversion. The scattering object $g(x)$ is assumed frequency independent in the examples considered in this presentation. Conditions for data completeness for backscatter measurements from a frequency independent scatterer are summarized as follows; 1.) A one-to-one mapping is obtained (i.e., all of k -space is covered) when backscattered data is available in all directions of observation/incidence, and at all temporal frequencies. 2.) If the scattering object is restricted to a real valued function (i.e. $\hat{g}(k)$ has Hermitian symmetry about the origin), then a complete data set requires backscatter measurements covering only 180 degrees, and at all temporal frequencies. 3.) If the object is bandlimited in spatial frequency, the object can be reconstructed from finite temporal frequency bandwidth data. 4.) The maximum spatial dimension of the object will determine the required temporal frequency sample spacing. 5.) Likewise, the angular sample spacing depends on angular frequency bandwidth of the object. An important question concerns how these facts change when the inversion becomes non-linear. Note

that in the non-linear case, the support of the total field $\hat{\phi}$ is no longer infinitesimal. Consequently, a given region of the measurement space is sensitive to values of $\hat{\phi}$ within a correspondingly larger region of the object k -space, via the convolution of Eq. (5.8).

In NDE practice, interest is often in the reconstruction of compact, discontinuous flaws using limited aperture, limited temporal frequency bandwidth backscatter data. The ultrasonic signals measured from such objects contain far less high spatial frequency information than is needed to sharply define the object boundary. Likewise, low frequency information required to define the gross shape and homogeneity of the scatterer is often insufficiently available. The following examples show how inversion errors due to such data deficiencies are compensated through the use of support minimization.

Inversion

The mechanics of the inversion scheme and the incorporation of support minimization are now summarized. The measured data at discrete points θ_i, ω_i in the θ, ω plane are denoted d_i^m . To proceed with the problem discretization, the scattering object is represented as a discrete sum

$$g(x) = \sum_j g_j v_j(x), \quad (5.10)$$

where $v_j(x)$ are suitably chosen basis functions. Likewise, the total scattered field at discrete frequency ω_i is written in terms of a basis $b_n(x, \omega_i)$ as

$$\phi(x, \omega_i) = \sum_n \phi_{ni} b_n(x, \omega_i). \quad (5.11)$$

A frequency dependent basis is desirable for representing the wavefield, since spatial frequency bandwidth requirements of the basis scale directly with temporal frequency. Using eqs. 5.10 and 5.11, discrete forms of Eqs. (5.3) and (5.5) are written

$$\sum_n (b_{mni} + \sum_j g_j G_{mnji}) \phi_{ni} = \phi_{mi}^{inc} \quad (5.12)$$

$$d_{im} = \sum_n \sum_j \phi_{ni} g_j G_{mnji}^O \quad (5.13)$$

$$G_{mnji} = k_0^2 \int_V b_n(x, \omega_i) v_j(x) \phi^G(x | x'_m, \omega_i) dx \quad (5.14)$$

$$G_{mnji}^O = k_0^2 \int_V b_n(x, \omega_i) v_j(x) \phi^G(x | -rn(\theta_m), \omega_i) dx \quad (5.15)$$

where $b_{mni} = b_n(x_m, \omega_i)$. Equations (5.12) and (5.13) state the discrete mapping between the data d_{im} and the object g_j .

The inversion proceeds through the optimization of a functional in the form of

$$\mathcal{E} = \int \mathcal{D}(\mathcal{F}(g_j), d_{im}) + \int \mathcal{S}(g_j). \quad (5.16)$$

where \mathcal{F} is the forward mapping from object to measurements, \mathcal{D} is the measure of distance (in this work \mathcal{D} is $(L_2)^2$), and \mathcal{S} is the minimum support functional as defined in chapter 2. The process is initiated with an approximation of the g_j (e.g. $g_j = 0$). Approximate scattered data d_{im} are evaluated through solution of the forward scattering problem. The functional and its gradient, are then evaluated, the g_j are appropriately updated, and the process is repeated. A conjugate gradient optimization algorithm was employed in the work reported here.

The forward scattering problem requires the inversion of a set of linear equations in the total field ϕ

$$\sum_n \phi_{ni} K_{mni} = \phi_{mi}^{inc} \quad (5.17)$$

$$K_{mni} = \sum_j g_j G_{mnji} + b_{mni} \quad (5.18)$$

The computational bottleneck in the inversion process is the inversion of Eq. (5.17). An explicit inversion of the matrix can be avoided by exploiting special properties of this matrix, such as the convolutional nature of the Green function. Additionally, it is not necessary to obtain an exact solution to Eq. (5.17) at every step of the solution, since the scattering object is itself an approximation during most of the procedure. Thus efficient means of approximately up-dating the scattering matrix can be employed.

Optimization of a functional as expressed by Eq. (5.16) requires taking the gradients of Eqs. (5.12), (5.13) with respect to the discrete object variables g_k . Eq. (5.16) is expressed in discrete form as

$$N = \sum_j P_j + \sum_i Q_i \quad (5.19)$$

$$\frac{\partial N}{\partial g_k} = \sum_i \frac{\partial P_i}{\partial g_k} + \sum_j \frac{\partial Q_j}{\partial d_j} \frac{\partial d_j}{\partial g_k} = 0 \quad (5.20)$$

where

$$\frac{\partial d_{im}}{\partial g_k} = \sum_n \phi_{ni} G_{nki}^0 + \sum_n \sum_j \frac{\partial \phi_{ni}}{\partial g_k} g_j G_{njk}^0 \quad (5.21)$$

The partials in the second term of Eq. (5.21) are obtained by solving the following system, derived by differentiation of Eq. (5.12)

$$\sum_n \frac{\partial \phi_{ni}}{\partial g_k} K_{mni} = - \sum_n \phi_{ni} g_k G_{mnki} \quad (5.22)$$

Note that one matrix inversion serves to solve both Eq. (5.18) and Eq. (5.22). In practice, however, it was observed that the increase in computation time resulting

from calculation of the second term in the right hand side of Eq. (5.21) far exceeds the increase in computation due to the error in the gradient when this term is ignored.

The first examples shown are inversions using the available measured data with no additional functional measures applied other than agreement with the measured data. The local measures applied to the measured data and reconstructed object, Eq.(33), are specified as

$$Q_k = |W_k(d_k - d_k^{measured})|^2 \quad k = 1, 2, \dots, i \times m \quad (5.23)$$

$$P_j = 0 \quad (5.24)$$

$$(5.25)$$

In the above equations, the index k denotes discrete measurement positions in the $\theta - \omega$ plane. The choice of weight function W_k significantly impacts the rate of convergence. An effective weighting was found to be

$$W_k = \frac{\omega_k^{1/2}}{C^2(\omega_k, r)} \quad (5.26)$$

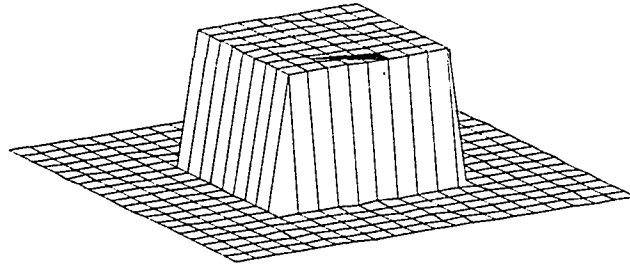
$$(5.27)$$

This weighting applies a filtering similar to that applied in a Born inversion. Indeed, it is noted that, with this weighting, the gradient vector bears considerable resemblance to the Born solution. Other measures of agreement with the measured data may be more appropriate under different circumstances, particularly in the presence of noise [42].

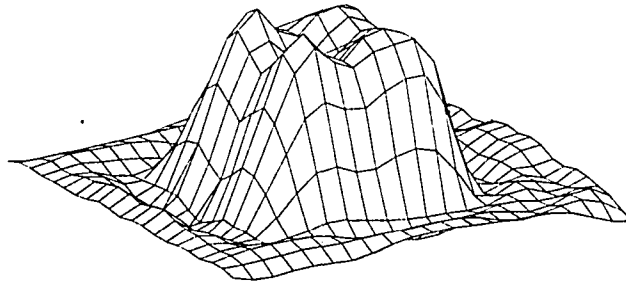
Results

Results are presented for two different scattering objects depicted in Figs.(5.2a) and (5.3a). The first object is a square inclusion with a discontinuous boundary and a velocity which is 30% slower than that of the background medium. This represents the most appropriate type of object for support minimization. The second object consists of two humps representing 30% and 25% reductions in velocity, and a neighboring dip representing a 80% increase in velocity. This object demonstrates the effect of support minimization when the object boundary is continuously varying, rather than discontinuous.

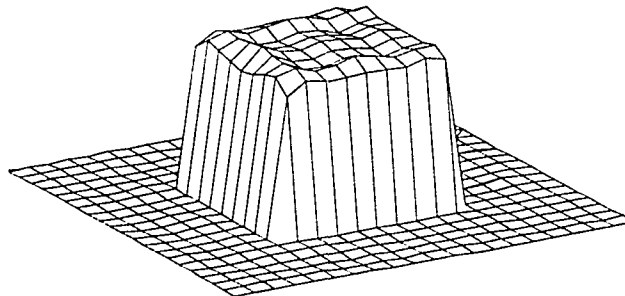
The scatterers of Figs.(5.2a) and (5.3a) are first reconstructed using a 180 degree backscatter aperture, and a relatively broad spectral bandwidth. The measured backscattered data is specified in 10 degree increments. For the object of Fig.(5.2a), six frequencies are equally spaced over a frequency bandwidth of $1.13 < ka < 6.78$, where k is the wavenumber in the background medium and a is the approximate radius of the circle circumscribing the object. For the object of Fig.(5.3a), ten frequencies are equally spaced over a frequency bandwidth of $0.8 < ka < 8.0$. The inversion is initiated by setting the $g_k = 0$. The reconstructions obtained using the measured data only (i.e. no support minimization or other penalties other than agreement with the measured data) are shown in Figs.(5.2b) and (5.3b). The reconstruction performance is better in Fig.(5.3b) than Fig.(5.2b) The reason for this is effectively illustrated in Fig.(5.4), which compares the spatial frequency amplitude spectra of the true and reconstructed objects in the x_1 direction. The true object of Fig.(5.2) is seen to have a substantially broader bandwidth than that of Fig.(5.3). Good agreement is seen over the entire object bandwidth for the object of Fig.(5.3).



(a)



(b)



(c)

Figure 5.2: Acoustic case 1: a) true scatterer potential $v(x)$ b) reconstruction using 6 frequency and 19 measurement position over 180 degree, c) reconstruction using 6 frequency and 19 measurement position over 180 degree with minimum support.

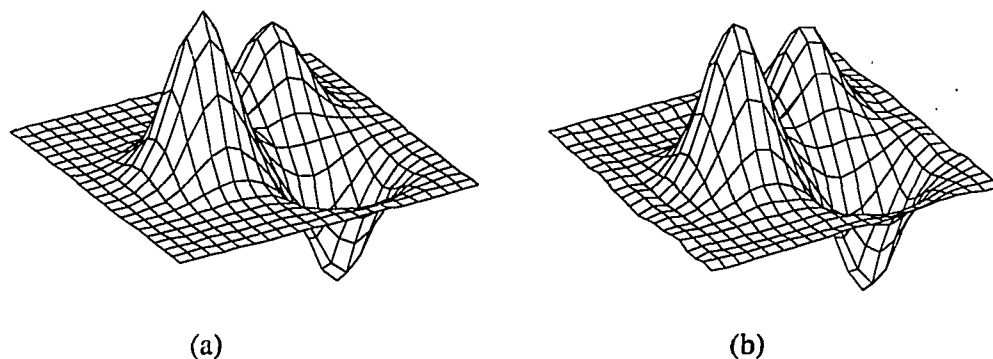


Figure 5.3: Acoustic case 2: a) true scatterer potential $v(x)$, b) reconstruction using 10 frequency and 19 measurement position over 180 degree.

Considerable disagreement between the true object and the reconstruction is evident at high frequencies for the object of Fig.(5.2). The spatial frequency bandwidth covered in the linear (Born) approximation by the measured data temporal frequency bandwidth is also indicated in Fig.(5.4). It is interesting to note that, in both cases, agreement between the true and reconstructed objects extends beyond the bandwidth limit imposed by the measured data under the linear approximation. This observation suggests that the conditions for completeness of data under the linear approximation may be a conservative estimate of those for the non-linear inversion. An interesting speculation is that this is the result of the convolution in Eq. (5.8), which increases the “domain of influence” in the mapping between object and measurement spaces.

Support minimization is now applied to the reconstruction of the object in Fig.(5.2). Eq. (5.24) is modified to

$$P_j = \gamma(1 + (\epsilon/|g_j|^\eta)^{-1} \quad (5.28)$$

The gradient calculation is in turn appropriately modified. The parameter γ in

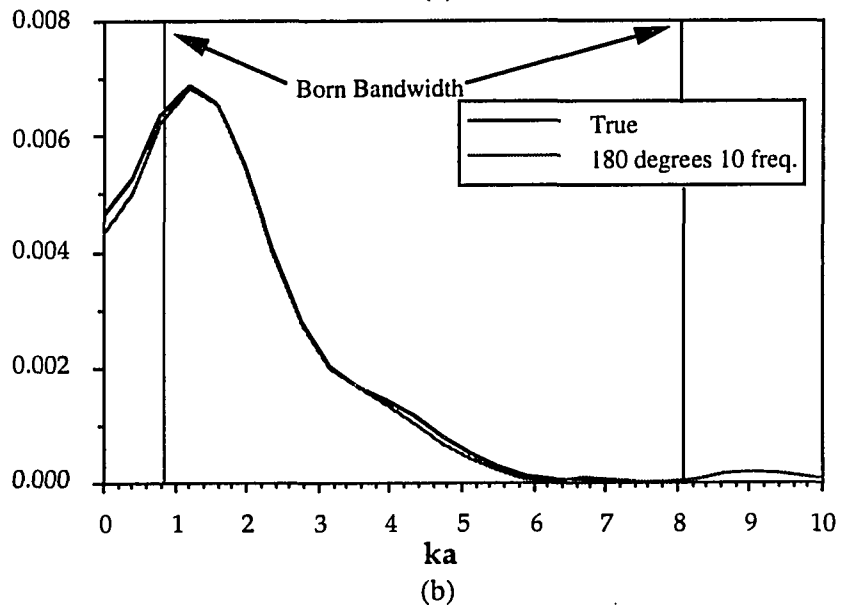
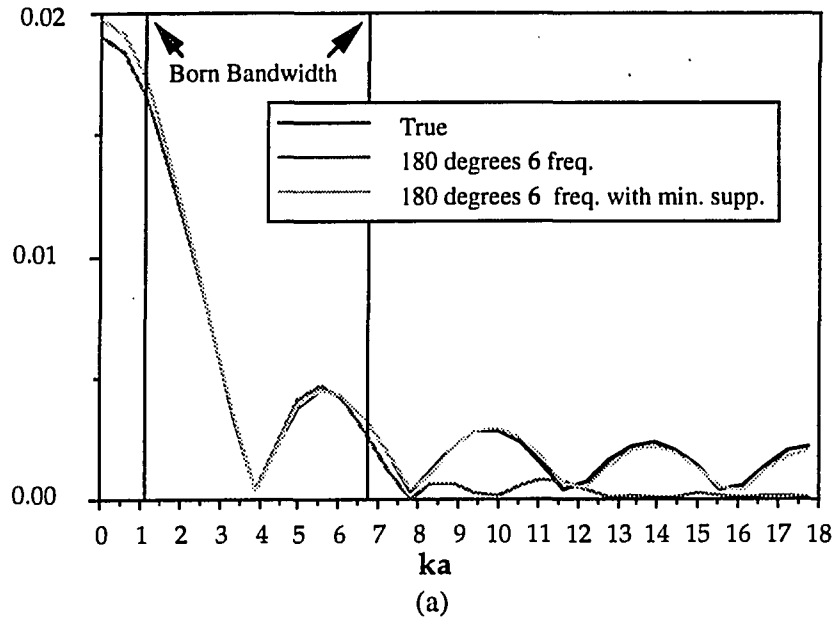


Figure 5.4: Spatial frequency domain profile for: a) acoustic scatterer of case 1, b) acoustic scatterer of case 2.

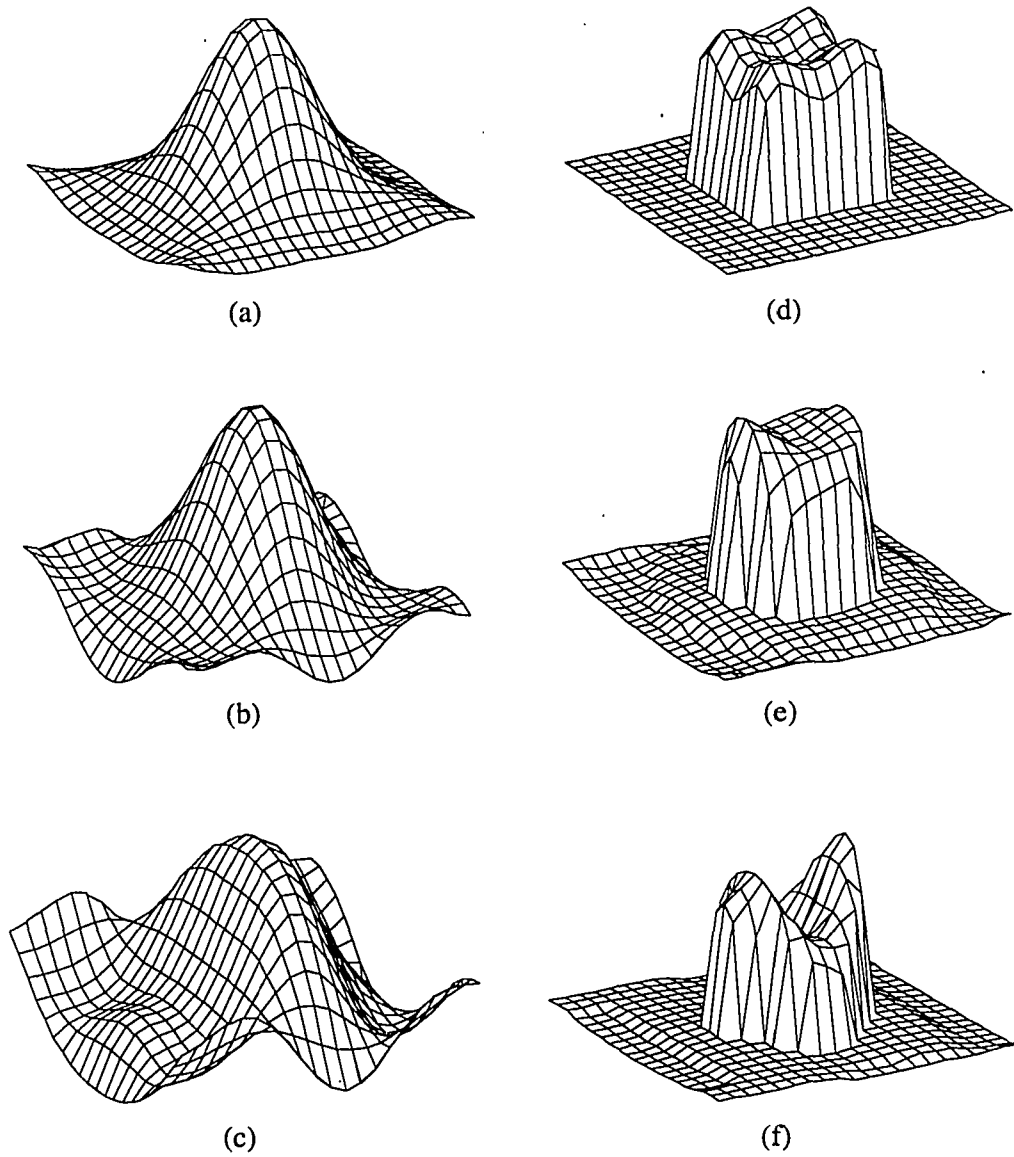


Figure 5.5: Acoustic reconstruction of scatterer in case 1: a) with 3 frequency and 19 measurements positions over 180 degree, b) with 3 frequency and 13 measurements positions over 120 degree, c) with 3 frequency and 10 measurement positions over 90 degree, d,e, and f are the above with minimum support functional minimized.

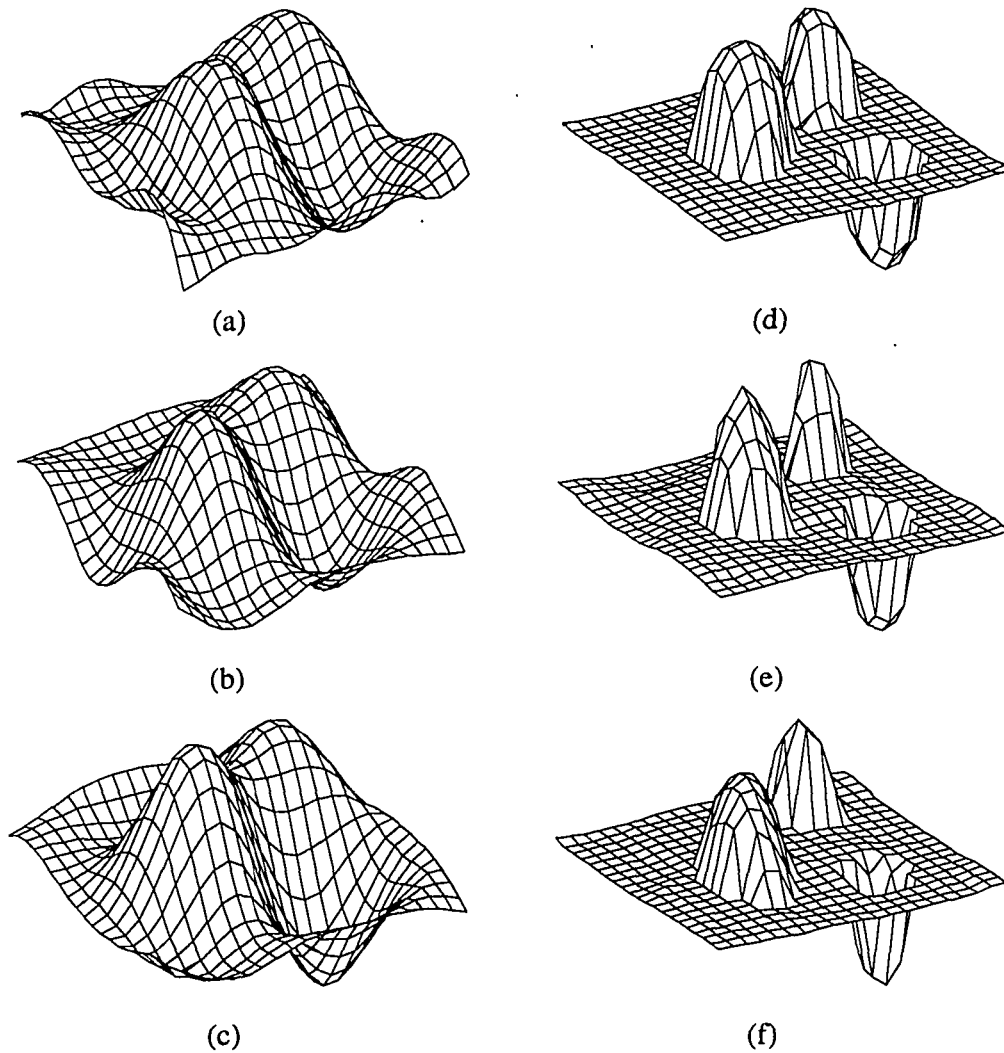


Figure 5.6: Acoustic reconstruction of scatterer in case 2: a) with 3 frequency and 19 measurements positions over 180 degree, b) with 3 frequency and 13 measurements positions over 120 degree, c) with 3 frequency and 10 measurement positions over 90 degree, d,e, and f are the above with minimum support functional minimized.

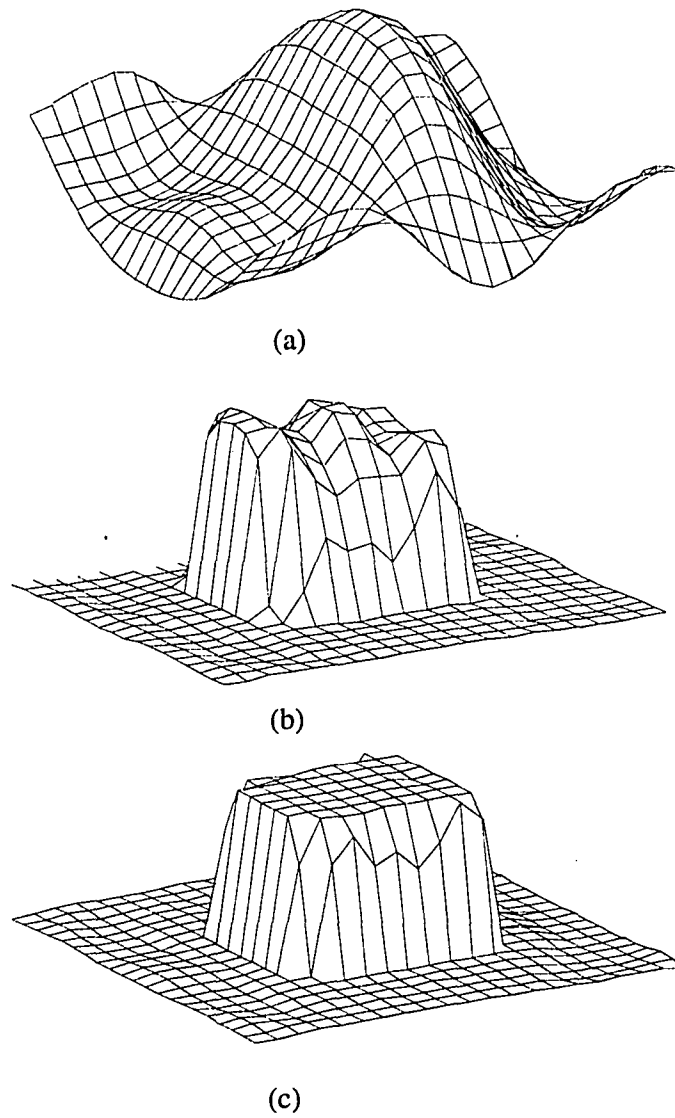


Figure 5.7: Acoustic reconstruction of scatterer in case 1 using: a) 6 frequency and 10 measurement positions over 90 degree, b) 6 frequency and 10 measurement positions over 90 degree with minimum support constraint, c) 6 frequency and 10 measurement positions over 90 degree with minimum support constraint and a quadratic penalty function for large pixels with $g_{ub} = 1.0$.

Eq. (5.28) balances the contributions of the P and Q operators to the optimized penalty. The threshold ϵ is set at 5% of the maximum magnitude of g_i and the parameter η is set to 4. The improvement resulting from support minimization is seen in Fig.(5.2c). This improvement is reflected in the improved agreement in the spatial frequency amplitude spectra, also plotted in Fig.(5.4a). Note the similarity between this result and spectral extrapolation methods based on causality constraints in time domain signal analysis. [28]

Reconstruction's of more severely limited data sets are now examined. In the following examples, the temporal spectral information is limited to three equi-spaced frequencies covering $1.13 < ka < 3.39$ for the object of Fig.(5.2) and $0.8 < ka < 2.4$ for the object of Fig.(5.3). Results for backscattered apertures of 180, 120, and 90 degrees are shown. The angular measurement spacing is kept at 10 degrees. The inversions were initiated with $g_k = 0$. Inversions using the incomplete measured data alone (no support minimization) are shown in Figs.(5.5a,b,c) and Figs.(5.6a,b,c) for the objects of Fig.(5.2) and Fig.(5.3), respectively. The results of the application of support minimization are shown in Figs.(5.5d,e,f) and Figs.(5.6d,e,f). The angular apertures in these results are a,d) 180 degrees, b,e) 120 degrees, and c,f) 90 degrees. The reconstruction without support minimization are obviously severely affected by the reduction in data. A sharper definition of the objects is readily apparent following the application of support minimization. The performance of support minimization in reconstructing an object which does not have discontinuous boundaries is demonstrated in Figs.(5.6d,e,f). The amplitudes of the three humps are reconstructed well, but the boundaries of the object are noticeably more compact than the true object. In this case, the algorithm has found an object consistent with the measured data

which has a support less than that of the true object. In Fig.(5.5d), the support of the square, discontinuous boundary is reconstructed quite well, and a reasonably good representation of the object amplitude is obtained. As the backscatter aperture is decreased, the sharp corners of the object support are seen to become rounded. In the most extreme example, Fig.(5.5f), using 3 frequencies and a 90 degree aperture, the corners of the true object support appear completely rounded, and the amplitude of the reconstruction is significantly in error.

Absolute Phase Error Correction

A significant problem in the practical implementation of any inversion scheme is the assignment of an absolute phase reference (i.e. a "zero-of-time") to individual measurements. This is particularly true in ultrasonic backscatter measurements where a single probe is mechanically (perhaps even manually) positioned at various angular orientations. Accurate inversion of the data requires knowing the probe position to within a small fraction of a wavelength, which, in practice, is not realistic to expect.

This lack of absolute phase information is compensated for in our approach by treating the "zero-of-time" associated with each measurement as variables in the variational optimization of the support functional. In practice, recorded signals scattered from a flaw under different angular orientations are aligned visually to roughly correspond to a common origin within the component. Following this visual alignment, the remaining uncertainty in probe position will likely be within a few wavelengths or less. Corrections for the uncertainties in probe position are denoted d_i , corresponding to the uncertainty in the radial distance from the probe to the flaw at the

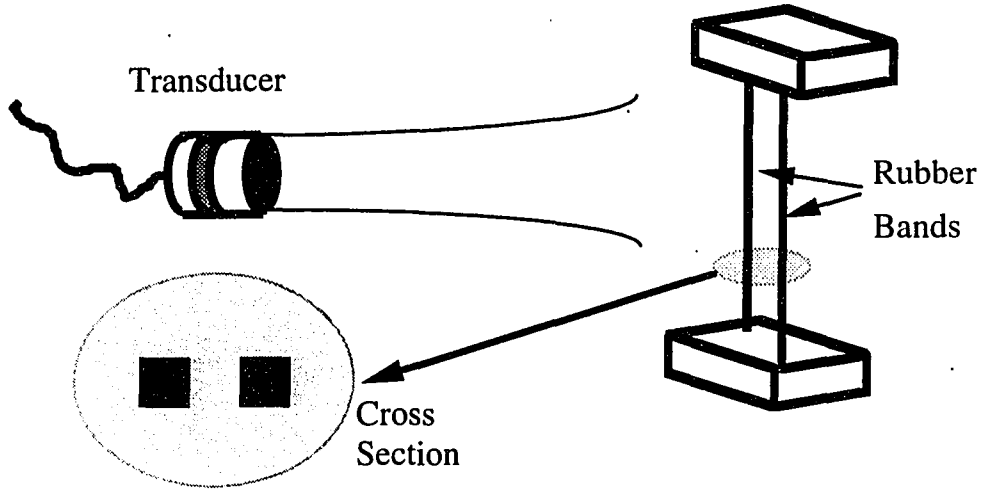


Figure 5.8: Experiment set-up: Back-scattered signal measured from two rubber band each $1mm$ thick using a $500Khz$ transducer.

i_{th} measurement position. The associated phase correction is incorporated into the functional $\mathcal{O}(v, d)$ as

$$\mathcal{O}(v, d) = \sum_i \sum_j |\mathcal{W}_i(\phi_{ij}^{sc:f}(v)e^{jkd_i} - \phi_{ij}^{sc:m})|^2 + \sum_m |v_m|^\eta / (|v_m|^\eta + \epsilon^\eta) \quad (5.29)$$

The d_i 's are treated as additional unknown variables, and are included in the total unknown vector along with the unknown variables v_i . After optimization is complete, the value of d_i indicates how much correction was applied to the i_{th} measurement position.

In order to test the robustness of the proposed algorithm, an experiment was set up as shown in Figs. (5.8), (5.9) and (5.10). In this experiment a series of time signals were collected at finite number of angular positions. The objective of the experiment is to reconstruct the scatterer without an absolute knowledge of the zero-of-time. The only additional a priori information about the object is an assumed compact-

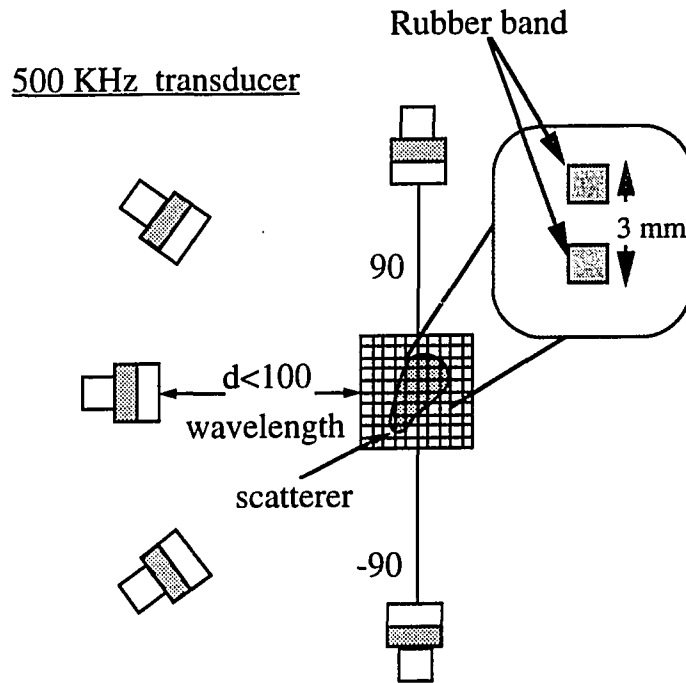


Figure 5.9: Pulse-echo time signals were collected at 19 angles over a 180 degree view angle.

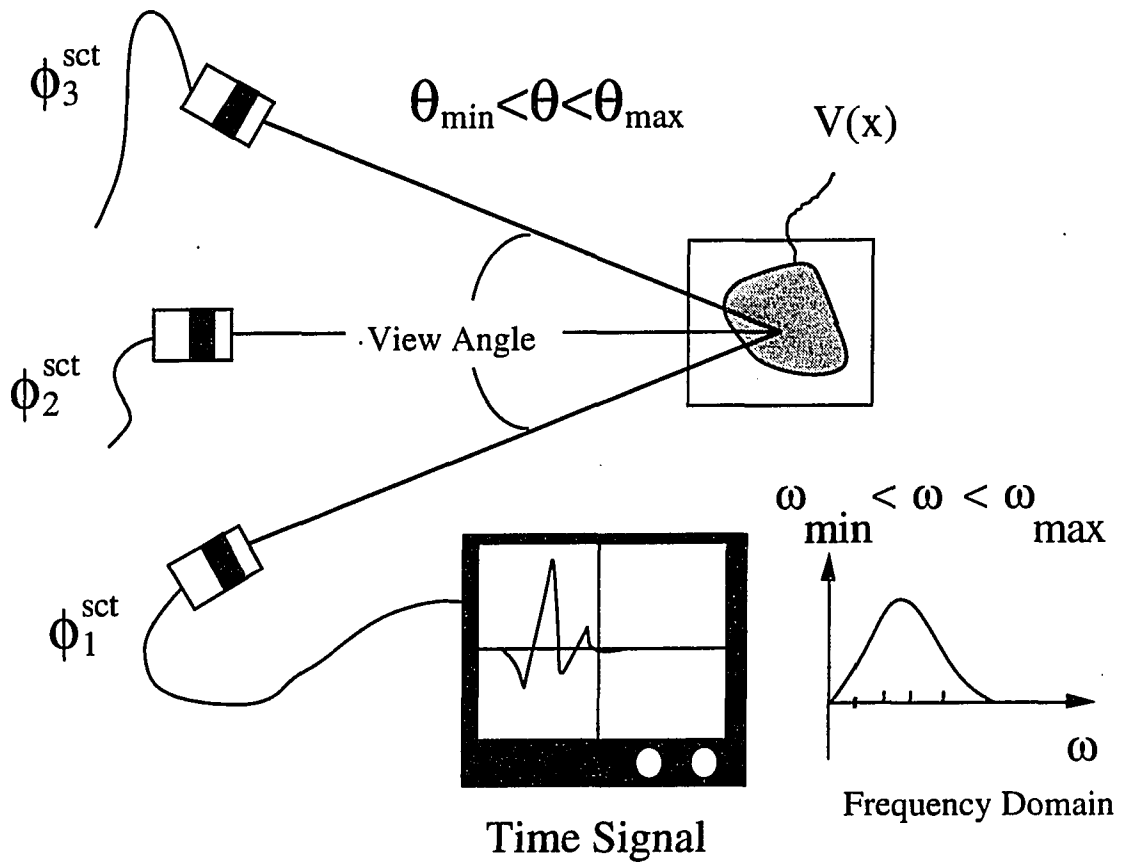


Figure 5.10: Time signals are digitized and Fourier transformed: inversion algorithm uses spectral components in the band-pass of the system.

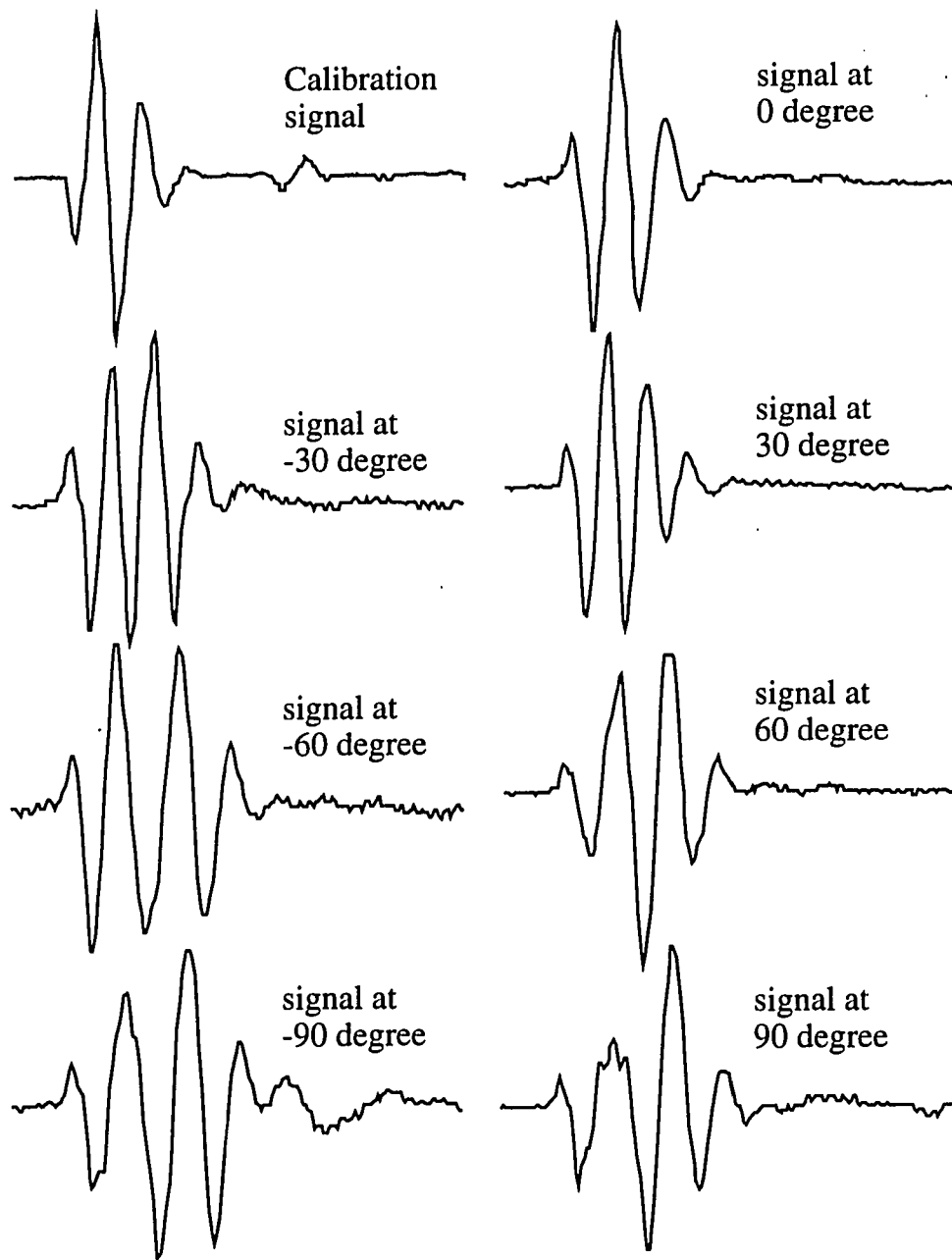


Figure 5.11: Some of collected Pulse-echo time signals.

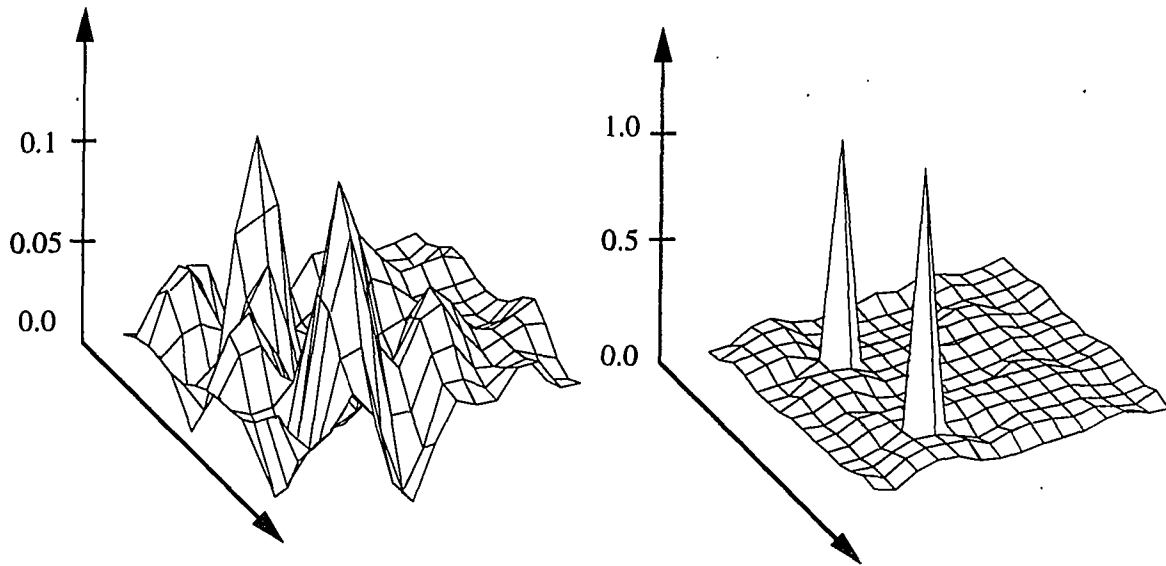


Figure 5.12: Results of inversion for scatter potential v using experimental data: a) without the minimum support functional and absolute phase corrections, b) with the minimum support functional and absolute phase corrections.

ness. A total of 19 measurements were made uniformly spaced in a 180 degree view angle. Following visual alignment, the time signals were Fourier transformed and deconvolved to remove the receiver response. Spectral values at a finite number of frequencies around the 500 khz operating frequency were selected as input data to the inversion algorithm. Results presented here utilized 6 frequency components equally spaced in the 250 to 650 khz range. As seen in Fig. (5.12a), the reconstruction of the object without support minimization or absolute measurement phase is not in agreement with the true scatterer geometry. Artifacts in Fig. (5.12a) indicate a far larger scatterer than actually exists. In Fig. (5.12b) the result of inversion with support

minimization and absolute phase error correction is presented. The reconstruction artifacts have been removed. The separation of the two objects is in agreement with the actual separation. The amplitude of the scattering potential likely does not truly represent the rubber band because the variable velocity Helmholtz equation does not accurately represent scattering from rubber in water. In Fig. (5.13), correction values for the position of the transducer at each measurement position are given. These corrections are the side product of the phase corrected inversion with minimum support. Note that corrections to the nominal distance d_0 are almost symmetric about the middle transducer at 0 degrees. This is expected since the object is symmetric about the 0 degree axis in Fig. (5.12). The visual alignment of the waveforms resulted in an approximately symmetric initial phase error.

Conclusion

A robust algorithm is presented for nonlinear acoustic inversion using acoustic backscatter data limited in both spatial and temporal frequency domains. This algorithm produces a more accurate and intelligible result when applied to scattering data for which an *a priori* assumed compactness is justified. The algorithm compensates for incompleteness in the measured data through the minimization of a functional measure of object support. Examples of application to simulated backscatter measurements demonstrated the effectiveness in reconstructing severely limited data. A scheme for compensating for unknown absolute measurement phases was introduced. This scheme variationally determines the zero-of-time associated with each measurement position as part of the support minimization procedure. Application of this algorithm to experimental back scatter data yielded excellent reconstruction of the

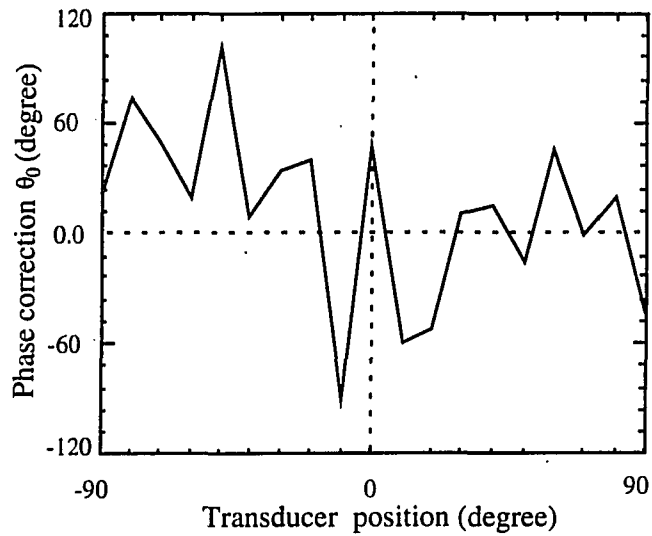


Figure 5.13: Phase corrections at center frequency of 500 khz ($\theta_0 = 360d_i/\lambda_0$).

scatterer geometry assuming no known zero-of-time data. Work is currently under way to extend the algorithm to elastic media.

CHAPTER 6. SUPPORT MINIMIZED NONLINEAR ELASTIC INVERSION

Introduction

NDE of structural components is primarily concerned with inversion of elastic wave scattering in solids. Similar problem has been addressed by workers in the geophysical context [7, 26, 25]. There are many similarities between NDE and geophysical applications. In the NDE applications, the object of interest containing the possible flaw is probed through an acoustic medium. This is done either by immersing the object in a fluid tank or by adding couplant fluid between transducer and the object. Likewise in the geophysical application, the object of interest might be under a body of water (oceanography). The backscattered wave can be detected either at the receiver position (pulse-echo mode) or at other locations by another transducer (pitch-catch mode). The time signals can be captured using a finite bandwidth receiver. The collected time signals carry information about the interface of the elastic solid and fluid in addition to the possible flaw information. In this chapter, we will not discuss how the fluid-solid interface is handled and will assume that scattered data is available somewhere inside the solid under test. There are many similarities between the acoustic inversion and the elastic inversion. In both cases, a forward model is used to simulate the measurements and the inversion is carried out using a

optimization approach. However, there are very significant differences in the physics involved. The main difference is the existence of two types of wave propagating with different velocities. Even when the incident wave is purely of one type, the scattered wave is almost always (except for a few unusual situations) of both types.

In the following, the forward elastic model is briefly restated. Next, a measure of fidelity to the measured data is defined and its gradients are derived. Finally, results are presented for the inversion of an elastic scatterer inside another known elastic solid using finite bandwidth data.

Forward Elastic Model

The wave motion in a homogeneous isotropic elastic solid is governed by

$$\tau_{ij,j} + \rho\omega^2 u_i = 0 \quad (6.1)$$

where stress tensor τ_{ij} is

$$\tau_{ij} = \lambda\delta_{ij}u_{k,k} + \mu(u_{i,j} + u_{j,i}) \quad (6.2)$$

where λ and μ are the Lamé's constants and ρ is the density. A repeated index convention is used; i.e. summation over the repeated index is implicit. Displacement U includes both shear (S-wave) and pressure wave (P-wave). The general solution to Eq. (6.1) in the presence of an incident displacement field u^{inc} can be represented in terms of the Green's functions $u_{i;j}^G(x|x')$ for the background medium with elastic parameters ρ_0 , λ_0 and μ_0 .

$$u_i(x') = u_i^{inc}(x') + \int u_{i;j}^G(x|x')s_j(x)dx. \quad (6.3)$$

where

$$-s_i(x) = \delta\lambda(x)u_{k,k_i}(x) + \delta\mu(x)(u_{i,jj}(x) + \quad (6.4)$$

$$u_{j,ii}(x)) + \delta\rho(x)\omega^2u_i \quad (6.5)$$

$$\tau_{ij:k,j}^G + \rho\omega^2u_i^G : k = \delta_{ik}\delta(x - x') \quad (6.6)$$

The displacement $u_i(x')$ can be obtained by solving the above equations. In order to solve for $u_i(x')$, we proceed to discretize the above integral equations. For the work that follows, the discretization is based on a simple finite difference scheme that was proven accurate and efficient in Chapter III.

Inversion Algorithm

The material parameters are found by a variational inversion of the scattered data as discussed in the previous chapters. Generally, a function $\mathcal{E}(\gamma)$

$$\mathcal{E}(\gamma) = \int \mathcal{L}(u(\gamma)) \quad (6.7)$$

where γ represents the material parameters to be solved for and $u(\cdot)$ is the scattered field which depends on γ . \mathcal{L} is a functional representing the distance between measured and calculated scattered field. In this work, functional \mathcal{L} is chosen to be a $(L_2)^2$ functional defined as

$$\mathcal{L}(u) = \sum_i |(u_i^{sct} - u_i^{meas.})|^2 \quad (6.8)$$

In this work, the inversion uses the displacements due to the p-type back-scattered portion of the scattered wave. Although in practice it is possible to obtain both P and S components of the scattered wave, it is not convenient. In fact, if we show we

can provide inversion with one type of back-scattered wave, surely, it is possible to provide a solution using both components.

$\mathcal{E}(\gamma)$ should be optimized with respect to γ . This can be done numerically using the gradient information of \mathcal{E} . First, the gradients of \mathcal{E} with respect to γ are found. The gradients are derived in the appendix.

To see how this inversion scheme performs, a test case is considered. The test involves inversion of an elastic scatterer in an homogeneous elastic background given the backscattered field at many temporal frequencies and angular positions. The number of measurements required for the inversion is not clearly understood for the non-linear inversion problem. However, we can estimate the values for $\Delta\omega$ and $\Delta\theta$ by inspection of the time signal at the observation point. $\Delta\omega$ should be chosen such that the observed time signal is uniquely defined. In other words, $\Delta\omega \leq \frac{1}{T}$ where T is the maximum length of the time signal among all signals measured. However, this condition for $\Delta\omega$ is a conservative estimate and in some cases this might not be necessary. For example, when there is resonance behavior, it might not be necessary to choose $\Delta\omega = 1/T$. Instead, one might find $\Delta\omega$ from the early portion of the signal. In other words, discard component of the signal that is due to resonance. This topic is still under study and definite answers may be known in the future.

Inversion Examples

To test the inversion algorithm, the case of scattering from steel impurities in Silicon-Nitride is considered. It is assumed that all the parameters vary as

$$\lambda(x) = v(x)(\lambda_1 - \lambda_0) + \lambda_0 \quad (6.9)$$

$$\mu(x) = v(x)(\mu_1 - \mu_0) + \mu_0 \quad (6.10)$$

$$\rho(x) = v(x)(\rho_1 - \rho_0) + \rho_0. \quad (6.11)$$

Hence, the inversion involves finding $v(x)$. The assumption that all three parameters λ , μ and ρ vary in the same way is not true in general. However, this is a reasonable assumption as a starting point to a full inversion. Due to the nonlinearity of the problem, it is not clear how much information is needed to obtain an exact inversion. Furthermore, it is not known to what degree the existence of local minima pose a problem in inversion. Due to high dimensionality the solution space it is very difficult to develop any intuitive picture of the penalty functional space. However, we can examine the penalty functional space on a one or two dimensional subspaces. For example, for a given scatterer v_0 , we can calculate penalty functional $\mathcal{E}(v(\lambda))$ where $v(\lambda)$ is defined as

$$v(\lambda) = v_0 + \lambda(v_0 - v_1) \quad (6.12)$$

v_1 is an arbitrary point chosen in the object space. By varying λ we can traverse the distance between v_0 and v_1 . Figs. 6.1a and 6.2b show two such plots for two cases 1) v_1 is all zero and 2) v_1 is all one. Each curve on the plot is the value of the penalty function on the line for one frequency. Figs. 6.2 shows the total penalty function for Figs. 6.1. From these plots, it is clear that by using few frequency, especially, when low frequency information is missing, there are many local minima. In our example, by increasing the number of frequencies the local minima disappeared. The weighting (or filtering) in the frequency domain plays an important role in removing the local minima. The optimum filter and means of obtaining such filters for each case are to be explored in the future.

In the first example, a Gaussian shape scatterer which is shown in Fig. (6.3) is reconstructed using scattered field at finite number of angles and frequencies. The

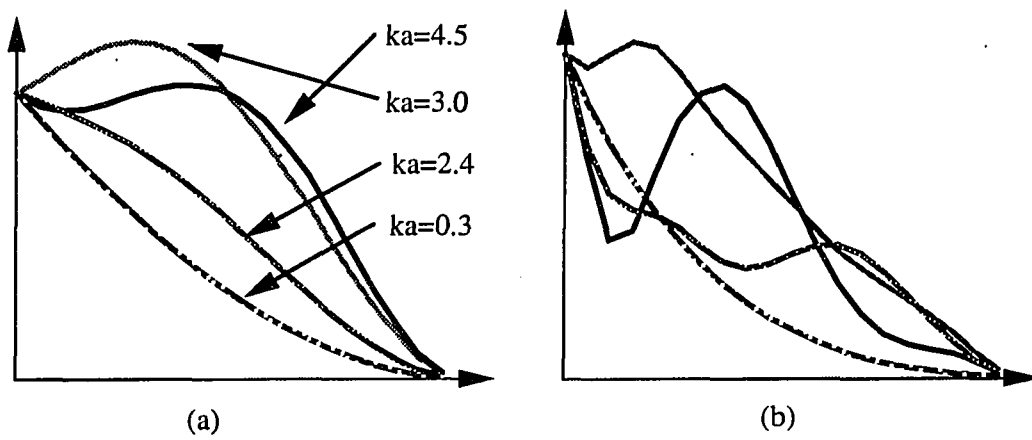


Figure 6.1: Curves showing the value of the penalty function versus λ for few frequencies: a) marching on a line from $v = 0$ to $v = v_0$, b) marching on a line from $v = 1$ to $v = v_0$

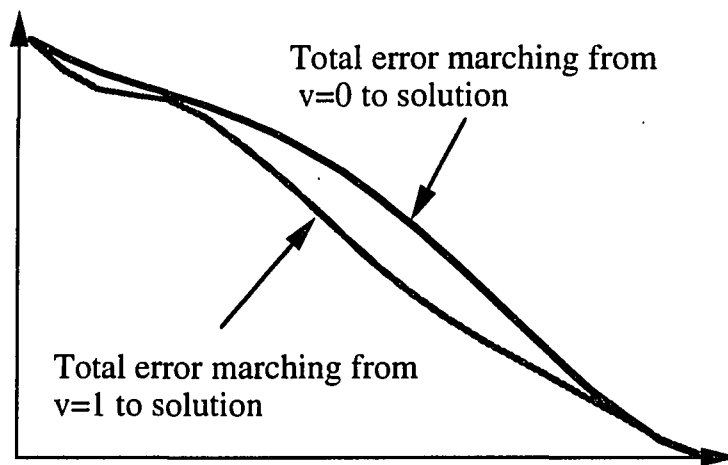


Figure 6.2: Comparing the total penalty function for the two cases.

reason for choosing Gaussian lie in the physical process the introduces the impurities. The impurity is introduced during the process of grinding the Silicon-Nitride with steel ball-bearings. Later, when Silicon-Nitride is heated to produce ceramic, the steel particles melt and diffuse in the background. This suggests it is reasonable to model the impurity with a Gaussian potential. The first case is with a 180 degree view angle and $0.1 < ka < 1.5$. The result of inversion without the minimum support is given in Fig. (6.4). The quality of inversion is acceptable and there are not many artifacts. After applying the minimum support the result is shown in Fig. 6.4a. The support has reduced slightly and there are not significant differences in the two result. Next, Inversion results are given for 150 and 120 degree view-angles respectively. The results of inversion without minimum support shows typical $(L_2)^2$ norm solution behavior although due to nonlinearity we do not know how close the solution without minimum support is to the $(L_2)^2$ norm solution. After applying the minimum support in both cases the object's support has reduced significantly and is much closer to the true object. In fact, the support is slightly smaller than the true object. In this case, there is sufficient spectral information and the incompleteness is due to the limited view-angle.

In the next case, measurements are provided over a 180 degree view-angle with ka range of $0.7 < ka < 6.0$. The reconstruction using these measurements clearly shows in Fig. 6.8a that there was not sufficient spectral information available and even with a 180 degree view-angle the inversion is not very good. The minimized support inversion extrapolated the spectral information accurately to provide a compact solution shown in Fig. 6.8b.

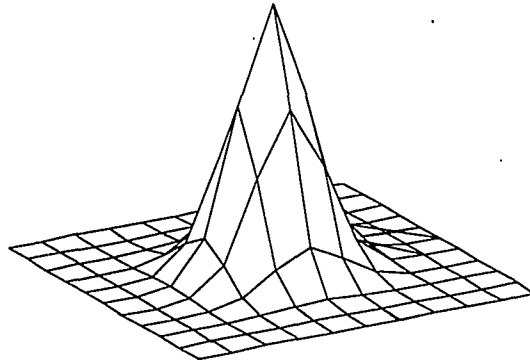


Figure 6.3: Original scatterer: Steel scatterer in Silicon-Nitride.

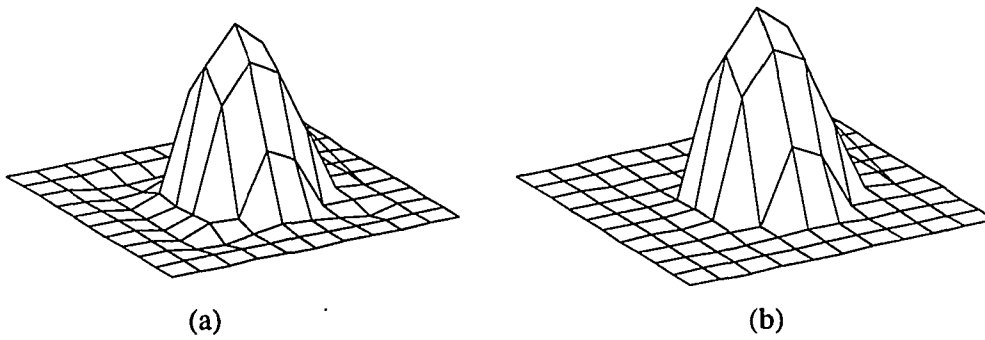


Figure 6.4: Inversion of a steel scatterer in Silicon-Nitride background using 180 degree view angle and $0.1 < ka < 1.5$ (e.g. for a 30μ radius particle $3 \text{ Mhz} < f < 50 \text{ Mhz}$): a) without minimum support, b) with the minimum support

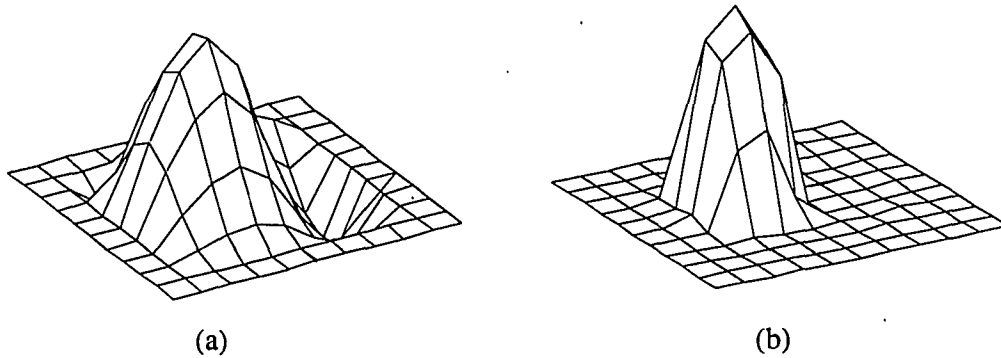


Figure 6.5: Inversion of a steel scatterer in Silicon-Nitride background using 150 degree view angle and $0.1 < ka < 1.5$ (e.g. for a 30μ radius particle $3 \text{ Mhz} < f < 50 \text{ Mhz}$): a) without minimum support b) with the minimum support

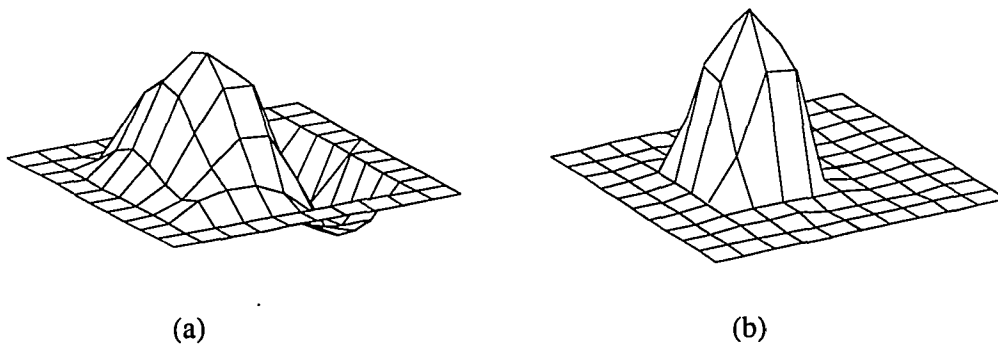


Figure 6.6: Inversion of a steel scatterer in Silicon-Nitride background using 120 degree view angle and $0.1 < ka < 1.5$ (e.g. for a 30μ radius particle $3 \text{ Mhz} < f < 50 \text{ Mhz}$): a) without minimum support b) with the minimum support

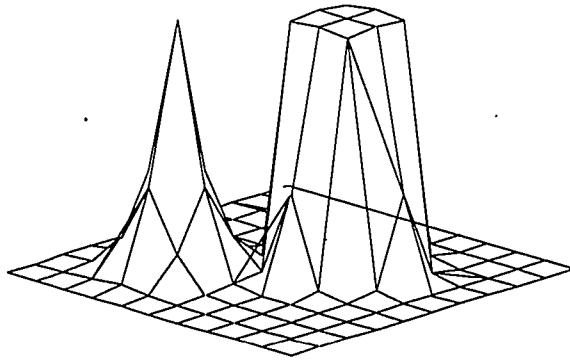


Figure 6.7: Original scatterer for case of steel in Silicon-Nitride

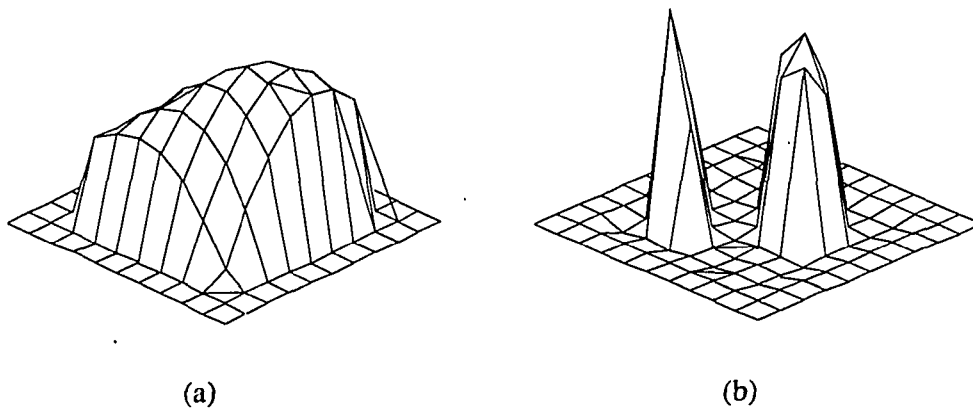


Figure 6.8: Inversion of a steel scatterer in Silicon-Nitride background using 180 degree view-angle and $0.7 < ka < 6$ (e.g. for a 30μ radius particle $20 \text{ Mhz} < f < 200 \text{ Mhz}$): a) without using minimum support, b) with using minimum support

Conclusion

An exact nonlinear elastic inversion of backscattered field was presented. Inversion results using a minimum support functional was compared with inversion results without the use of minimum support. Generally, when it is a priori known that scatterers are compact, the minimum support constraint can effectively reduce the artifact and ripples that are created due to missing data. In other words, the minimum support constraints helps fill the missing data in such a way that the resulting scatterer has the smallest volume (as defined by the minimum support functional). This technique is very suitable for NDE inversion of flaws such as cracks and voids where the compactness a priori assumption holds.

BIBLIOGRAPHY

- [1] Bates, R.H., "Renaissance inversion," *Inverse Problems of Acoustics and Elastic Waves*, F. Santosa, Y. Pao, W.W. Symes, and C. Holland, eds., SIAM, Philadelphia, 1984.
- [2] Berkhout, A.J., "Relationship between linearized inverse scattering and seismic migration," *Inverse Problems of Acoustics and Elastic Waves*, F. Santosa, Y. Pao, W.W. Symes, and C. Holland, eds., SIAM, Philadelphia, 1984.
- [3] Bleistein, N., J.K. Cohen, and F.G. Hagin, "Two and one-half dimensional Born inversion with an arbitrary reference," *Geophysics*, **52**, 26-36, 1987.
- [4] Boyse, W.E., J.B. Keller, "Inverse elastic scattering in three dimensions," *J. Acoust. Soc. Am.*, **79**, 215-218, 1986.
- [5] Corones, J.P., R.J. Krueger, and V. H. Weston, "Some recent results in inverse scattering theory," *Inverse Problems of Acoustics and Elastic Waves*, F. Santosa, Y. Pao, W.W. Symes, and C. Holland, eds., SIAM, Philadelphia, 1984.
- [6] Bryan, R.K. J. Skilling, "Deconvolution by maximum entropy, as illustrated by application to the jet of M87," *Monthly Notes Royal astronomical Society*, **191**, 69-79, 1980.

- [7] Crase, E., A. Pica, M. Noble, J. McDonald, and A. Tarantola, "Robust elastic nonlinear waveform inversion: Application to real data," *Geophysics*, **55**, 527-538, 1990.
- [8] Devaney, A.J., "Acoustic tomography," *Inverse Problems of Acoustics and Elastic Waves*, F. Santosa, Y. Paò, W.W. Symes, and C. Holland, eds., SIAM, Philadelphia, 1984.
- [9] Esmersoy, C., M. Oristaglio, "Reverse time wave-field extrapolation, imaging, and inversion," *Geophysics*, **53**, 920-931, 1988.
- [10] Firth, D., and R.F. Gould, "A hybrid finite difference/Helmholtz integral scheme for ultrasonic scattering," *Journal of Nondestructive Evaluation*, **9**, 167-179, 1990.
- [11] Frieden, B.R. "Computer in optical research: methods and application," Springer-Verlag, New-York, 1980.
- [12] Frieden, B.R. "Probability, statistical optics, and data testing: a problem solving approach," Springer-Verlag, New-York, 1991.
- [13] Frisk, G.V., J.F. Lynch, and S.D. Rajan, "Determination of compressional wave speed profiles using modal inverse techniques in a range-dependent environment in Nantucket sound," *J. Acoust. Soc. Am.*, **86**, 1928-1939, 1989.
- [14] Goswami, P.P., T.J. Rudolphi, F.J. Rizzo, and D.J. Shippy, "A boundary element model for acoustic-elastic interaction with applications in ultrasonic NDE," *Journal of Nondestructive Evaluation*, **9**, 101-112, 1990.

- [15] Goutsias, J.I., and J.M. Mendel, "Inverse problems in two-dimensional acoustic media: A linear imaging model," *J. Acoust. Soc. Am.*, **81**, 1471-1485, 1987.
- [16] Harker, A.H., J.A. Ogilvy, and J.A.G. Temple, "Modeling ultrasonic inspection of austenitic welds," *Journal of Nondestructive Evaluation*, **9**, 155-165, 1990.
- [17] Hsu, D.K., J.H. Rose, and D.O. Thompson, "Reconstruction of inclusions in solids using ultrasonic inverse Born approximation," *Journal of Applied Physics*, **55**, 162-168, 1984.
- [18] Kogan, V.G. and J.H. Rose, "Limited aperture effects on ultrasonic image reconstruction," *Journal of Acoustical Society of America*, **77**, 1342-1351, 1985.
- [19] Lailly, P., "Migration methods: Partial but efficient solutions to the seismic inverse problem," *Inverse Problems of Acoustics and Elastic Waves*, F. Santosa, Y. Pao, W.W. Symes, and C. Holland, eds., SIAM, Philadelphia, 1984.
- [20] Langenberg, K.J., "Applied inverse problems for acoustic, electromagnetic and elastic wave scattering," *Basic methods of tomography and inverse problems*, P.C. Sabatier editor, Adam Hilger, Bristol, England, 1987.
- [21] LeBras, R., and R.W. Clayton, "An iterative inversion of back-scattered acoustic waves," *Geophysics*, **53**, 501-508, 1988.
- [22] Levi, A., and H. Stark, "Image restoration by the method of generalized projections with application to restoration from magnitude," *Journal of Optical Society of America A*, **1**(9), 932-43, 1981.

- [23] Levy, B.C., and C. Esmersoy, "Variable background Born inversion by wavefield backpropagation," *SIAM J. Appl. Math.*, **48**, 952-971, 1988.
- [24] Lord, W., R. Ludwig, and Z. You, "Developments in ultrasonic modeling with finite element analysis," *Journal of Nondestructive Evaluation*, **9**, 129-143, 1990.
- [25] Mora, P., "Elastic wave-field inversion of reflection and transmission data," *Geophysics*, **53**, 750-759, 1988.
- [26] Mora, P., "Nonlinear two-dimensional elastic inversion of multioffset seismic data," *Geophysics*, **52**, 1211-1228, 1987.
- [27] Pao, Y.H. and C.C. Mow, "Diffraction of elastic waves and dynamical stress concentration," Rand Report R-482-PR, Rand, Santa Monica, 1971.
- [28] Poe, G.D., "Frequency response extrapolation in the theory of scattering," *Ph.D. Dissertation*, Univ. California at Davis, 1983.
- [29] Reshef, M., D. Kosloff, M. Edwards, and C. Hsiung, "Three-dimensional acoustic modeling by the Fourier method," *Geophysics*, **53**, 1175-1183, 1988.
- [30] Roberts, R.A. "Limited Data Tomography Using a Minimal Support Constraint," in *Review of Progress in Quantitative Nondestructive Evaluation*, **10A** Edited by D.O. Thompson and D.E. Chimenti, Plenum Press, New York, 435-442, 1991.
- [31] Roberts, R.A., "Model of the acoustic microscope response to scattering by near-surface void," *Journal of Nondestructive Evaluation*, **9**, 181-196, 1991.
- [32] Roberts, R.A. and A. Safaeinili, "Support Minimized Inversion of Incomplete Data: Application to X-Ray and Acoustic Data," submitted to *Inverse Problems*.

- [33] Rose, J.H., "Elastic Wave Inverse Scattering in Nondestructive Evaluation," *Pure and Applied GeoPhysics*, **131**(4), 715-739, 1989.
- [34] Sabatier, P.C., "Well-posed questions and exploration of the space of parameters in linear and non-linear inversion," *Inverse Problems of Acoustics and Elastic Waves*, F. Santosa, Y. Pao, W.W. Symes, and C. Holland, eds., SIAM, Philadelphia, 1984.
- [35] Sezan, M.I., and H. Stark, "Image restoration by convex projections in the presence of noise," *Journal of Applied Optics*, 2781-9, 1983.
- [36] Safaeinili, A., and J.P. Basart "Flaw Detection using a priori knowledge with limited view aperture system," in *Review of Progress in Quantitative Nondestructive Evaluation*, **9A** Edited by D.O. Thompson and D.E. Chimenti, Plenum Press, New York, 737-741, 1990.
- [37] Safaeinili, A. and J.P. Basart, "Applying a line-by-line Kalman filter Fourier mode image restoration," *Proceedings of 23rd Asilomar Conference on Signals, Systems and Computers*, 1989
- [38] Safaeinili, A., J.P. Basart, and H.-S. Hung, "Reconstructing low contrast flaws in limited view angle industrial tomograms using prototype flawless images," *Proceedings of 24th Asilomar Conference on Signals, Systems and Computers*, 1990.
- [39] Santosa, F., "Inverse Problems of Acoustics and Elastic Waves," *Inverse Problems of Acoustics and Elastic Waves*, F. Santosa, Y. Pao, W.W. Symes, and C. Holland, eds., SIAM, Philadelphia, 1984.

- [40] Schafbach, P.J., R.B. Thompson, and F.J. Rizzo, "Application of the boundary element method to elastic wave scattering by irregular defects," difference/Helmholtz integral scheme for ultrasonic scattering," *Journal of Nondestructive Evaluation*, **9**, 113-127, 1990.
- [41] Skilling J., R.K. Bryan "Maximum entropy image reconstruction: general algorithm," *Monthly Notes Royal astronomical Society*, **211**, 111-124,1984.
- [42] Tarantola, A., "The seismic reflection problem," *Inverse Problems of Acoustics and Elastic Waves*, F. Santosa, Y. Pao, W.W. Symes, and C. Holland, eds., SIAM, Philadelphia, 1984.
- [43] Zhu, W., "Inverse scattering of the three-dimensional elastic wave equation for three parameters," *J. Acoust. Soc. Am.*, **87**, 2371-2375, 1990.
- [44] Wu, R., and M.N. Toksoz, "Diffraction tomography and multisource holography applied to seismic imaging," *Geophysics*, **52**, 11-25, 1987.

APPENDIX A. GREEN'S FUNCTION DERIVATION

The displacement Green's functions for the infinite elastic medium with Lamé parameters λ, μ and ρ satisfy the following equation.

$$\tau_{ij,j:m} + \rho\omega^2 u_{i:m} = \delta(x - x')\delta_{im} \quad (\text{A.1})$$

where

$$\tau_{ij} = \lambda\delta_{ij}u_{k,k} + \mu(u_{i,j} + u_{j,i}) \quad (\text{A.2})$$

By replacing τ_{ij} in Eq. (A.1) with Eq. (A.2) we obtain

$$(\rho\omega^2 + \mu\frac{\partial^2}{\partial x_2^2} + (\lambda + 2\mu)\frac{\partial^2}{\partial x_1^2})u_{1:1}^G + ((\lambda + \mu)\frac{\partial^2}{\partial x_1\partial x_2})u_{2:1}^G = \delta(x - x') \quad (\text{A.3})$$

$$(\rho\omega^2 + \mu\frac{\partial^2}{\partial x_1^2} + (\lambda + 2\mu)\frac{\partial^2}{\partial x_2^2})u_{2:1}^G + ((\lambda + \mu)\frac{\partial^2}{\partial x_1\partial x_2})u_{1:1}^G = \delta(x - x') \quad (\text{A.4})$$

assuming a space harmonic form for displacement u Eq. (A.4) transforms into an algebraic equation which can be solved to yield

$$\hat{u}_{11}(k_1, k_2) = \frac{1}{\mu} \left\{ \frac{k_1^2}{k_T^2} \left(\frac{1}{k^2 - k_L^2} - \frac{1}{k^2 - k_T^2} \right) + \frac{1}{k^2 - k_T^2} \right\} \quad (\text{A.5})$$

$$\hat{u}_{12}(k_1, k_2) = \frac{1}{\mu} \left\{ \frac{k_1 k_2}{k_T^2} \left(\frac{1}{k^2 - k_L^2} - \frac{1}{k^2 - k_T^2} \right) \right\} \quad (\text{A.6})$$

Hence the displacement Green function can be obtained by taking the two-dimensional Fourier transform of the $\hat{u}_{11}(k_1, k_2)$ and $\hat{u}_{12}(k_1, k_2)$.

$$u_{11}(x_1, x_2) = \frac{1}{4\mu i} \{ H_0(k_T r) - \frac{1}{k_T^2} \left\{ \frac{x_1^2}{2r^2} (k_L^2 (H_2(k_L r) - H_0(k_L r))) - \right. \quad (\text{A.7})$$

$$k_T^2(H_2(K_T r) - H_0(k_T r)) + \frac{x_2^2}{r^3}(k_T H_1(k_T r) - k_L H_1(k_L r)) \quad (\text{A.8})$$

$$u_{12}(x_1, x_2) = -\frac{x_1 x_2}{\mu 4i k_T^2} \left\{ \frac{1}{2r^2} (k_L^2 (H_2(k_L r) - H_0(k_L r)) - \right. \quad (\text{A.9})$$

$$\left. k_T^2 (H_2(K_T r) - H_0(k_T r)) + \frac{1}{r^3} (k_T H_1(k_T r) - k_L H_1(k_L r)) \right\} \quad (\text{A.10})$$

Due to the symmetry, $u_{12}(x_1, x_2) = u_{21}(x_1, x_2)$ and $u_{22}(x_1, x_2)$ can be obtained from $u_{11}(x_1, x_2)$ by interchanging indices 1 and 2.

APPENDIX B. DISCRETIZATION OF THE INTEGRAL EQUATION

The wave motion in a homogenous isotropic elastic solid is governed by

$$\tau_{ij,j} + \rho\omega^2 u_i = 0 \quad (\text{B.1})$$

where stress tensor τ_{ij} is

$$\tau_{ij} = \lambda\delta_{ij}u_{k,k} + \mu(u_{i,j} + u_{j,i}) \quad (\text{B.2})$$

where λ and μ are the Lamé's constants and ρ is the density. Displacement U includes both shear (S-wave) and pressure wave (P-wave). Generally, parameters ρ , λ and μ are not constant; indicating the material is inhomogenous. If the medium is homogenous everywhere except for a finite region of space, then it is beneficial to represent ρ , λ and μ as

$$\rho = \rho_0 + \rho(x) \quad (\text{B.3})$$

$$\lambda = \lambda_0 + \lambda(x) \quad (\text{B.4})$$

$$\mu = \mu_0 + \mu(x) \quad (\text{B.5})$$

The general solution to Eq. (B.1) at presence of an incident displacement field u^{inc} can be represented in terms of the Green's functions $G_{i;j}(x|x')$ for the background medium with elastic parameters ρ_0 , λ_0 and μ_0 .

$$u_i(x') = u_i^{inc}(x') + \int G_{i;j}(x|x')s_j(x)dx. \quad (\text{B.6})$$

The displacement $u_i(x')$ can be obtained by solving the above equations. In order to solve for $u_i(x')$, we proceed to discretize the above integral equations. The choice of the basis function is very important in obtaining a physically sensible solution. As it will be discussed further, if only far-field displacements are desired, the choice of basis function is not as crucial as when we are interested in displacements close to the discontinuity regions. In the case at hand where functions and its derivatives are to be defined, a basis function should be chosen that is differentiable at least up to the order needed. Some basis functions like Gaussian-Sinc functions are infinitely differentiable

$$b(x) = e^{-a^2 x^2} \text{Sinc}\left(\frac{\pi x}{\Delta x}\right) \quad (\text{B.7})$$

where a is chosen such that it effectively limits the support of the basis function so the numerical integration can be carried out over a finite support. The choice of Δx depends on the bandwidth that is required. $u_i(x')$, $\lambda(x')$, $\mu(x')$ and $\rho(x')$ may be expressed in terms of the basis function $b(x)$ as

$$u_i(x') = \sum_k u_i(x_k) b(x' - x_k) \quad (\text{B.8})$$

$$\lambda(x') = \sum_k \lambda(x_k) b(x' - x_k) \quad (\text{B.9})$$

$$\mu(x') = \sum_k \mu(x_k) b(x' - x_k) \quad (\text{B.10})$$

$$\rho(x') = \sum_k \rho(x_k) b(x' - x_k) \quad (\text{B.11})$$

By combining Eqs. (B.6) and (B.11), the following linear system of equation is obtained.

$$\sum_k a_{ik}^{11} u_k^1 + a_{ik}^{12} u_k^2 = u_i^{1:inc} \quad (\text{B.12})$$

$$\sum_k a_{ik}^{21} u_k^1 + a_{ik}^{22} u_k^2 = u_i^{2:inc} \quad (\text{B.13})$$

where u_k^1 and u_k^2 are vectors containing first and second displacement components. a_{ik}^{jl} 's are defined as

$$a_{ik}^{jl} = - \int G_{j:1}(x_m, y_n; x, y) A_{1l}(x, y; x_p, y_q) + G_{j:2}(x_m, y_n; x, y) A_{2l}(x, y; x_p, y_q) \quad (\text{B.14})$$

where $G_{i:j}$ is the Green function given by

$$G_{1:1}^l(r) = \frac{1}{\lambda k_l^2 4i} [-k_l^2 \frac{x_2^2}{r^2} H_0''(k_l r) - k_l \frac{x_1^2}{r^3} H_0'(k_l r) - k_l^2 H_0(k_l r)] \quad (\text{B.15})$$

$$G_{1:2}^l(r) = G_{2:1}^l(r) = \frac{x_1 x_2}{4i \lambda k_l^2} [\frac{k_l^2}{r^2} H_0''(k_l r) - \frac{k_l}{r^3} H_0'(k_l r)] \quad (\text{B.16})$$

$$G_{2:2}^l(r) = \frac{1}{\lambda k_l^2 4i} [-k_l^2 \frac{x_1^2}{r^2} H_0''(k_l r) - k_l \frac{x_2^2}{r^3} H_0'(k_l r) - k_l^2 H_0(k_l r)] \quad (\text{B.17})$$

$$(\text{B.18})$$

and A_{ij} is given by

$$A_{11}(x, y; x_p, y_q) = - \sum_{m=p-n}^{p+np} \sum_{n=q-nq}^{q+nq} [(\lambda(x_m, y_n) + 2\mu(x_m, y_n)) b'(x - x_p) b'(x - x_n) b(y - y_q) b(y - y_n) + (\lambda(x_m, y_n) + 2\mu(x_m, y_n)) b''(x - x_p) b(x - x_n) b(y - y_q) b(y - y_n) + \mu(x_m, y_n) b(x - x_p) b(x - x_n) b'(y - y_q) b'(y - y_n) +$$

$$\mu(x_m, y_n)b(x - x_p)b(x - x_n)b''(y - y_q)b(y - y_n) + \quad (\text{B.19})$$

$$A_{12}(x, y; x_p, y_q) = - \sum_{m=p-n}^{p+n} \sum_{n=q-n}^{q+n} \quad (\text{B.20})$$

$$\begin{aligned} & [\lambda(x_m, y_n)b(x - x_p)b'(x - x_n)b'(y - y_q)b(y - y_n) + \\ & (\lambda(x_m, y_n) + \mu(x_m, y_n))b'(x - x_p)b(x - x_n)b'(y - y_q)b(y - y_n) + \\ & \mu(x_m, y_n)b'(x - x_p)b(x - x_n)b(y - y_q)b'(y - y_n) \end{aligned} \quad (\text{B.21})$$

$$A_{21}(x, y; x_p, y_q) = - \sum_{m=p-n}^{p+n} \sum_{n=q-n}^{q+n} \quad (\text{B.22})$$

$$\begin{aligned} & [\lambda(x_m, y_n)b'(x - x_p)b(x - x_n)b(y - y_q)b'(y - y_n) + \\ & (\lambda(x_m, y_n) + \mu(x_m, y_n))b'(x - x_p)b(x - x_n)b'(y - y_q)b(y - y_n) + \\ & \mu(x_m, y_n)b(x - x_p)b'(x - x_n)b'(y - y_q)b(y - y_n) \end{aligned} \quad (\text{B.22})$$

$$A_{22}(x, y; x_p, y_q) = - \sum_{m=p-n}^{p+n} \sum_{n=q-n}^{q+n} \quad (\text{B.23})$$

$$\begin{aligned} & [(\lambda(x_m, y_n) + 2\mu(x_m, y_n))b(x - x_p)b(x - x_n)b'(y - y_q)b'(y - y_n) + \\ & (\lambda(x_m, y_n) + 2\mu(x_m, y_n))b(x - x_p)b(x - x_n)b''(y - y_q)b(y - y_n) + \\ & \mu(x_m, y_n)b'(x - x_p)b'(x - x_n)b(y - y_q)b(y - y_n) + \\ & \mu(x_m, y_n)b''(x - x_p)b(x - x_n)b(y - y_q)b(y - y_n) + \\ & \omega^2 \rho(x_m, y_n)b(x - x_p)b(x - x_n)b(y - y_q)b(y - y_n)] \end{aligned} \quad (\text{B.23})$$

**APPENDIX C. DISCRETIZATION OF THE INTEGRAL
EQUATION (ALTERNATE METHOD)**

In order to find the displacements on the scatterer, the field equations need to be discretized. The discretized equations yield a system of equations for the $2 \times N$ displacement components. These equations can be written as

$$A_{ij}U_j = U_i^{inc} \quad (C.1)$$

where

$$\begin{aligned} A_{11}(p, q; l, k) = & \delta_{(p,q),(l,k)} + \\ & \sum_{i=-1}^1 \sum_{j=-1}^1 \gamma^{11}(i, j; p, q) G_{11}(p - k + i, q - l + j) + \\ & \sum_{i=-1}^1 \sum_{j=-1}^1 \gamma^{21}(i, j; p, q) G_{12}(p - k + i, q - l + j) \quad (C.2) \end{aligned}$$

$$\begin{aligned} A_{12}(p, q; l, k) = & \sum_{i=-1}^1 \sum_{j=-1}^1 \gamma^{12}(i, j; p, q) G_{11}(p - k + i, q - l + j) + \\ & \sum_{i=-1}^1 \sum_{j=-1}^1 \gamma^{22}(i, j; p, q) G_{12}(p - k + i, q - l + j) \quad (C.3) \end{aligned}$$

(C.4)

$$A_{21}(p, q; l, k) = \sum_{i=-1}^1 \sum_{j=-1}^1 \gamma^{11}(i, j; p, q) G_{21}(p - k + i, q - l + j) +$$

$$\sum_{i=-1}^1 \sum_{j=-1}^1 \gamma^{21}(i, j; p, q) G_{22}(p - k + i, q - l + j) \quad (C.5)$$

$$\begin{aligned} A_{22}(p, q; l, k) &= \delta_{(p,q),(l,k)} + \\ &\sum_{i=-1}^1 \sum_{j=-1}^1 \gamma^{12}(i, j; p, q) G_{21}(p - k + i, q - l + j) + \\ &\sum_{i=-1}^1 \sum_{j=-1}^1 \gamma^{22}(i, j; p, q) G_{22}(p - k + i, q - l + j) \quad (C.6) \end{aligned}$$

where γ^{ij} 's are defined as

$$\begin{aligned} \gamma^{11}(i, j; l, k) &= \\ (l, k) = (0, 0) &= 2\mu(i, j) + 2\kappa(i, j) - \rho(i, j)\omega^2\Delta x^2 \\ (l, k) = (-1, 0) &= -\kappa(i, j) + 0.25(\kappa(i + 1, j) - \kappa(i - 1, j)) \\ (l, k) = (1, 0) &= -\kappa(i, j) - 0.25(\kappa(i + 1, j) - \kappa(i - 1, j)) \\ (l, k) = (0, -1) &= -\mu(i, j) + 0.25(\mu(i, j + 1) - \mu(i, j - 1)) \\ (l, k) = (0, 1) &= -\mu(i, j) - 0.25(\mu(i, j + 1) - \mu(i, j - 1)) \\ \gamma^{12}(i, j; l, k) &= \\ (l, k) = (-1, -1) &= -0.25(\lambda(i, j) + \mu(i, j)) \\ (l, k) = (1, 1) &= -0.25(\lambda(i, j) + \mu(i, j)) \\ (l, k) = (-1, 1) &= 0.25(\lambda(i, j) + \mu(i, j)) \\ (l, k) = (1, -1) &= 0.25(\lambda(i, j) + \mu(i, j)) \\ (l, k) = (0, -1) &= 0.25(\lambda(i + 1, j) - \lambda(i - 1, j)) \\ (l, k) = (0, 1) &= -0.25(\lambda(i + 1, j) - \lambda(i - 1, j)) \\ (l, k) = (-1, 0) &= 0.25(\mu(i, j + 1) - \mu(i, j - 1)) \end{aligned}$$

$$\begin{aligned}
(l, k) = (1, 0) &= -0.25(\mu(i, j + 1) - \mu(i, j - 1)) \\
\gamma^{22}(i, j; l, k) &= \\
(l, k) = (0, 0) &= 2\mu(i, j) + 2\kappa(i, j) - \rho(i, j)\omega^2\Delta x^2 \\
(l, k) = (-1, 0) &= -\mu(i, j) + 0.25(\mu(i + 1, j) - \mu(i - 1, j)) \\
(l, k) = (1, 0) &= -\mu(i, j) - 0.25(\mu(i + 1, j) - \mu(i - 1, j)) \\
(l, k) = (0, -1) &= -\kappa(i, j) + 0.25(\kappa(i, j + 1) - \kappa(i, j - 1)) \\
(l, k) = (0, 1) &= -\kappa(i, j) - 0.25(\kappa(i, j + 1) - \kappa(i, j - 1)) \\
\gamma^{21}(i, j; l, k) &= \\
(l, k) = (-1, -1) &= -0.25(\lambda(i, j) + \mu(i, j)) \\
(l, k) = (1, 1) &= -0.25(\lambda(i, j) + \mu(i, j)) \\
(l, k) = (-1, 1) &= 0.25(\lambda(i, j) + \mu(i, j)) \\
(l, k) = (1, -1) &= 0.25(\lambda(i, j) + \mu(i, j)) \\
(l, k) = (0, -1) &= 0.25(\mu(i + 1, j) - \mu(i - 1, j)) \\
(l, k) = (0, 1) &= -0.25(\mu(i + 1, j) - \mu(i - 1, j)) \\
(l, k) = (1, 0) &= -0.25(\lambda(i, j + 1) - \lambda(i, j - 1)) \\
(l, k) = (-1, 0) &= 0.25(\lambda(i, j + 1) - \lambda(i, j - 1))
\end{aligned}$$

APPENDIX D. SERIES SOLUTION TO SCATTERING FROM A CYLINDER

The scattering from an elastic cylinder in an elastic background is a special case for which an exact solution may be found. The solution can be found in Pao and Mow [27]. The solution is expressed in the form of an infinite series.

Since we only consider a 2-D in plane motion the displacement u can be expressed as

$$u = \nabla\phi + \nabla \times \psi_z. \quad (\text{D.1})$$

Both ϕ and ψ satisfy the Helmholtz equation. Due to circular symmetry, we start with the Helmholtz equation in the cylindrical coordinates.

$$\left\{ \frac{\partial^2}{\partial r^2} + \frac{1}{r} \frac{\partial}{\partial r} + \frac{1}{r^2} \frac{\partial^2}{\partial \theta^2} + k^2 \right\} A = 0 \quad (\text{D.2})$$

solution to the above Helmholtz equation for the field outside of the cylinder can be written as

$$A(r, \theta) = \sum_{-\infty}^{\infty} c_m H_m(kr) e^{im\theta} \quad (\text{D.3})$$

and

$$A(r, \theta) = \sum_{-\infty}^{\infty} c_m J_m(kr) e^{im\theta} \quad (\text{D.4})$$

for the solution of the field inside the cylinder. where $H_m(kr)$ and $J_m(kr)$ are the m th order Hankel and Bessel functions. For each order there 4 unknown coefficients

in the final solution. Two coefficients for P-wave and S-wave inside the cylinder and two for outside solution. These unknowns can be obtained through satisfying the following boundary conditions

$$u_r^I = u_r^{II} \quad (D.5)$$

$$u_\theta^I = u_\theta^{II} \quad (D.6)$$

$$\tau_r^I = \tau_r^{II} \quad (D.7)$$

$$\tau_\theta^I = \tau_\theta^{II} \quad (D.8)$$

For each order m , the following four equations are solved to obtain the coefficients.

$$\begin{aligned} & k_p^I H'_m(k_p^I a) P C_m^I + \frac{im}{a} H_m(k_s^I a) S C_m^I \\ -k_p^{II} J'_m(k_p^{II} a) P C_m^{II} - \frac{im}{a} J_m(k_s^{II} a) S C_m^{II} &= -\frac{m}{a} i^{m+1} J_m(k_s^I a) \end{aligned} \quad (D.9)$$

$$\begin{aligned} & \frac{im}{a} H_m(k_p^I a) P C_m^I - k_s^I H'_m(k_s^I a) S C_m^I \\ -\frac{im}{a} J_m(k_p^{II} a) P C_m^{II} + k_s^{II} J'_m(k_s^{II} a) S C_m^{II} &= i^m k_s^I J'_m(k_s^I a) \end{aligned} \quad (D.10)$$

$$\begin{aligned} & ((\lambda^I + 2\mu^I) k_p^{I2} H''_m(k_p^I a) \\ & + \frac{\lambda^I k_p^I}{a} H'_m(k_p^I a) - \frac{\lambda^I m^2}{a^2} H_m(k_p^I a)) P C_m^I \\ & + (\frac{2\mu^I}{a} i m k_s^I H'_m(k_s^I a) - \frac{2\mu^I}{a^2} i m H_m(k_s^I a)) S C_m^I \\ & - ((\lambda^{II} + 2\mu^{II}) k_p^{II2} J''_m(k_p^{II} a) \\ & + \frac{\lambda^{II} k_p^{II}}{a} J'_m(k_p^{II} a) - \frac{\lambda^{II} m^2}{a^2} J_m(k_p^{II} a)) P C_m^{II} \\ & - (\frac{2\mu^{II}}{a} i m k_s^{II} J'_m(k_s^{II} a) - \frac{2\mu^{II}}{a^2} i m J_m(k_s^{II} a)) S C_m^{II} = \\ & - (\frac{2\mu^I}{a} i^{m+1} m k_s^I J'_m(k_s^I a) - \frac{2\mu^I}{a^2} i^{m+1} m J_m(k_s^I a)) \end{aligned} \quad (D.11)$$

$$\begin{aligned}
& \left(\frac{2im}{a} k_p^I H'_m(k_p^I a) - \frac{2im}{a} H_m(k_p^I a) \right) P C_m^I \\
& + (-k_s^{I2} H_m''(k_s^I a) + \frac{k_s^I}{a} H'_m(k_s^I a) - \frac{m^2}{a^2} H_m(k_s^I a)) S C_m^I \\
& - \frac{\mu^{II}}{\mu^I} \left(\frac{2im}{a} k_p^{II} J'_m(k_p^{II} a) - \frac{im}{a^2} J_m(k_s^{II} a) \right) P C_m^{II} \\
& - \frac{\mu^{II}}{\mu^I} \left(-k_s^{II2} J_m''(k_s^{II} a) - \frac{1}{a^2} J_m(k_s^{II} a) + \frac{im}{a} J_m(k_s^{II} a) \right) S C_m^{II} = \\
& -im \left(-k_s^{I2} J_m''(k_s^I a) - \frac{1}{a^2} J_m(k_s^I a) + \frac{im}{a} J_m(k_s^I a) \right) \quad (D.12)
\end{aligned}$$

APPENDIX E. PARALLEL COMPUTATION

An exact calculation of the forward scattered field requires considerable amount of computer time even for a very modest size scatterer. Parallel computers can be utilized effectively in the forward scattering calculation. There are two general category of parallel computers; 1) Single Instruction Multiple Data (SIMD) and 2) Multiple Instruction Multiple Data (MIMD).

In MIMD machines different processors can carry out different task on different data simultaneously. This type of machines are useful in "coarse grain" parallelization where large independent segments of the code run in parallel. In SIMD machines, on the other hand, the processors carry out the same operation on different data, hence, making "fine grain" parallelization possible. Generally, SIMD machines are more suited to our application. Operations like matrix multiplication, addition and inversion which are the major operations in the forward calculation, can be parallelized very easily and efficiently on a SIMD machine. In fact in our parallelized forward scattering code, most of the time was saved in the parallel matrix inversion and multiplication and summation. Our code was written for a 16000 processor MasPar (MP1) parallel computer.

The main difficulty in programming a SIMD parallel computer is the memory management and data distribution. Since each processor has a small memory size

(about 4 Kbyte), usually, it is not possible to store all of the data on all processors. Hence data should be distributed between all processors. However, if data is not distributed efficiently between processors, the amount of communication time needed to swap information could severely reduce the speed.

Optimum performance can be achieved by minimizing the interaction between the processors and also the interaction between the parallel machine and the host machine (ALU).

APPENDIX F. GRADIENT CALCULATION

In this section the gradients of the displacement with respect to the $v(x_i)$ is derived. To avoid any unnecessary complexity, we will derive the gradient of u_1^{sct} with respect to $v(x_i)$. It is clear that the derivation of gradients of u_2^{sct} follow analogous to that of u_1^{sct} .

Since we are interested in the discrete form of the gradient for numerical implementation, the discrete representation of the integral which results in u_1^{sct} is used.

$$u_1^{sct}(x^{sct}, \omega) = \sum_i \sum_j s_1(i, j) G_{11}(i, j | x^{sct}, \omega) + s_2(i, j) G_{12}(i, j | x^{sct}, \omega) \quad (\text{F.1})$$

where

$$s_1(x) = -\lambda_{,1}(u_{1,1} + u_{2,2}) - \lambda(u_{1,11} + u_{2,21}) - 2\mu_{,1}u_{1,1} - \mu_{,2}(u_{1,2} + u_{2,1}) - \mu(2u_{1,11} + u_{1,22} + u_{2,12}) - \rho\omega^2 u_1 \quad (\text{F.2})$$

so the gradient can be written as

$$\frac{\partial u_1^{sct}(x, \omega)}{\partial v_{mn}} = \sum_i \sum_j \frac{\partial s_1(i, j)}{\partial v_{mn}} G_{11}(i, j | x, \omega) + \frac{\partial s_2(i, j)}{\partial v_{mn}} G_{12}(i, j | x, \omega) \quad (\text{F.3})$$

The assumption is made that λ , μ and ρ can be represented as

$$\lambda(x) = (\lambda_1 - \lambda_0)v(x) + \lambda_0 = \delta\lambda v(x) + \lambda_0 \quad (\text{F.4})$$

$$\mu(x) = (\mu_1 - \mu_0)v(x) + \mu_0 = \delta\mu v(x) + \mu_0 \quad (\text{F.5})$$

$$\rho(x) = (\rho_1 - \rho_0)v(x) + \rho_0 = \delta\rho v(x) + \rho_0 \quad (\text{F.6})$$

Using the above equations, the gradients of s_1 with respect to v_{mn} can be written as

$$\begin{aligned} \sum_i \sum_j \frac{\partial s_1(i, j)}{\partial v_{mn}} G_{11}(i, j) = & \\ & -\left\{ \frac{\delta\lambda}{2} [(u_{1,1} + u_{2,2})^{(m-1,n)} G(m-1, n) - \right. \\ & (u_{1,1} + u_{2,2})^{(m+1,n)} G(m+1, n)] + \\ & \delta\lambda [(u_{1,11} + u_{2,12})^{(m,n)} G(m, n)] + \\ & \delta\mu [u_{1,1}^{(m-1,n)} G(m-1, n) - u_{1,1}^{(m+1,n)} G(m+1, n)] + \\ & \frac{\delta\mu}{2} [(u_{1,2} + u_{2,1})^{(m,n-1)} G(m, n-1) - \\ & (u_{1,2} + u_{2,1})^{(m,n+1)} G(m, n+1)] + \\ & \delta\mu [(2u_{1,11} + u_{1,22} + u_{2,12})^{(m,n)} G(m, n)] + \\ & \left. \rho\omega^2 u_1^{m,n} G(m, n) \right\} \quad (\text{F.7}) \end{aligned}$$

By expanding all terms and rearranging them above can be written as

$$\begin{aligned} \sum_i \sum_j \frac{\partial s_1(i, j)}{\partial v_{mn}} G_{\alpha\beta}(i, j) = & \sum_{l=-2}^2 \sum_{k=-2}^2 A_{11\alpha\beta}(l, k; m, n) u_1(m+l, n+k) + \\ & \sum_{l=-1}^1 \sum_{k=-1}^1 A_{12\alpha\beta}(l, k; m, n) u_2(m+l, n+k) \\ \sum_i \sum_j \frac{\partial s_2(i, j)}{\partial v_{mn}} G_{\alpha\beta}(i, j) = & \sum_{l=-1}^1 \sum_{k=-1}^1 A_{21\alpha\beta}(l, k; m, n) u_1(m+l, n+k) + \end{aligned}$$

$$\sum_{l=-2}^2 \sum_{k=-2}^2 A_{22\alpha\beta}(l, k; m, n) u_2(m+l, n+k) \quad (\text{F.8})$$

where

$$\begin{aligned} A_{11\alpha\beta}(l, k; m, n) &= \\ (l, k) = (0, 0) &= -\delta\rho\omega^2\Delta x^2 G_{\alpha\beta}(m, n) - \\ &\quad \frac{\delta\lambda}{4}(G_{\alpha\beta}(m-1, n) + G_{\alpha\beta}(m+1, n) - 8G_{\alpha\beta}(m, n)) - \\ &\quad \frac{\delta\mu}{4}(2G_{\alpha\beta}(m-1, n) + 2G_{\alpha\beta}(m+1, n) + \\ &\quad G_{\alpha\beta}(m, n-1) + G_{\alpha\beta}(m, n+1) - 24G_{\alpha\beta}(m, n)) \\ (l, k) = (-2, 0) &= \frac{\delta\lambda}{4}G_{\alpha\beta}(m-1, n) + \frac{\delta\mu}{4}G_{\alpha\beta}(m-1, n) \\ (l, k) = (2, 0) &= \frac{\delta\lambda}{4}G_{\alpha\beta}(m+1, n) + \frac{\delta\mu}{4}G_{\alpha\beta}(m+1, n) \\ (l, k) = (0, -2) &= \frac{\delta\mu}{4}G_{\alpha\beta}(m, n-1) \\ (l, k) = (0, 2) &= \frac{\delta\mu}{4}G_{\alpha\beta}(m, n+1) \\ (l, k) = (-1, 0) &= -(\delta\lambda + 2\delta\mu)G_{\alpha\beta}(m, n) \\ (l, k) = (1, 0) &= -(\delta\lambda + 2\delta\mu)G_{\alpha\beta}(m, n) \\ (l, k) = (0, -1) &= -\delta\mu G_{\alpha\beta}(m, n) \\ (l, k) = (0, 1) &= -\delta\mu G_{\alpha\beta}(m, n) \end{aligned} \quad (\text{F.9})$$

and

$$\begin{aligned} A_{12\alpha\beta}(l, k; m, n) &= \\ (l, k) = (-1, -1) &= \frac{\delta\lambda}{4}(G_{\alpha\beta}(m-1, n) - G_{\alpha\beta}(m, n)) + \\ &\quad \frac{\mu}{4}(G_{\alpha\beta}(m, n-1) - G_{\alpha\beta}(m, n)) \\ (l, k) = (-1, +1) &= -\frac{\delta\lambda}{4}(G_{\alpha\beta}(m-1, n) - G_{\alpha\beta}(m, n)) - \end{aligned}$$

$$\begin{aligned}
(l, k) = (+1, -1) &= \frac{\mu}{4}(G_{\alpha\beta}(m, n+1) - G_{\alpha\beta}(m, n)) \\
&\quad - \frac{\delta\lambda}{4}(G_{\alpha\beta}(m+1, n) - G_{\alpha\beta}(m, n)) - \\
(l, k) = (+1, +1) &= \frac{\mu}{4}(G_{\alpha\beta}(m, n-1) - G_{\alpha\beta}(m, n)) \\
&\quad + \frac{\delta\lambda}{4}(G_{\alpha\beta}(m+1, n) - G_{\alpha\beta}(m, n)) + \\
&\quad \frac{\mu}{4}(G_{\alpha\beta}(m, n+1) - G_{\alpha\beta}(m, n)) \tag{F.10}
\end{aligned}$$

$$\begin{aligned}
A_{22\alpha\beta}(l, k; m, n) &= \\
(l, k) = (0, 0) &= -\delta\rho\omega^2\Delta x^2 G_{\alpha\beta}(m, n) - \\
&\quad \frac{\delta\lambda}{4}(G_{\alpha\beta}(m, n-1) + G_{\alpha\beta}(m, n+1) - 8G_{\alpha\beta}(m, n)) - \\
&\quad \frac{\delta\mu}{4}(2G_{\alpha\beta}(m, n-1) + 2G_{\alpha\beta}(m, n+1) + \\
&\quad G_{\alpha\beta}(m-1, n) + G_{\alpha\beta}(m+1, n) - 24G(m, n)) \\
(l, k) = (0, -2) &= \frac{\delta\lambda}{4}G_{\alpha\beta}(m, n-1) + \frac{\delta\mu}{4}G_{\alpha\beta}(m, n-1) \\
(l, k) = (0, 2) &= \frac{\delta\lambda}{4}G_{\alpha\beta}(m, n+1) + \frac{\delta\mu}{4}G_{\alpha\beta}(m, n+1) \\
(l, k) = (-2, 0) &= \frac{\delta\mu}{4}G_{\alpha\beta}(m-1, n) \\
(l, k) = (2, 0) &= \frac{\delta\mu}{4}G_{\alpha\beta}(m+1, n) \\
(l, k) = (0, -1) &= -(\delta\lambda + 2\delta\mu)G_{\alpha\beta}(m, n) \\
(l, k) = (0, 1) &= -(\delta\lambda + 2\delta\mu)G_{\alpha\beta}(m, n) \\
(l, k) = (-1, 0) &= -\delta\mu G_{\alpha\beta}(m, n) \\
(l, k) = (1, 0) &= -\delta\mu G_{\alpha\beta}(m, n) \tag{F.11}
\end{aligned}$$

and

$$A_{12\alpha\beta}(l, k; m, n) =$$

$$\begin{aligned}
(l, k) = (-1, -1) &= \frac{\delta\lambda}{4}(G_{\alpha\beta}(m, n-1) - G_{\alpha\beta}(m, n)) + \\
&\quad \frac{\mu}{4}(G_{\alpha\beta}(m-1, n) - G_{\alpha\beta}(m, n)) \\
(l, k) = (-1, +1) &= -\frac{\delta\lambda}{4}(G_{\alpha\beta}(m, n-1) - G_{\alpha\beta}(m, n)) - \\
&\quad \frac{\mu}{4}(G_{\alpha\beta}(m+1, n) - G_{\alpha\beta}(m, n)) \\
(l, k) = (+1, -1) &= -\frac{\delta\lambda}{4}(G_{\alpha\beta}(m, n+1) - G_{\alpha\beta}(m, n)) - \\
&\quad \frac{\mu}{4}(G_{\alpha\beta}(m-1, n) - G_{\alpha\beta}(m, n)) \\
(l, k) = (+1, +1) &= \frac{\delta\lambda}{4}(G_{\alpha\beta}(m, n+1) - G_{\alpha\beta}(m, n)) + \\
&\quad \frac{\mu}{4}(G_{\alpha\beta}(m+1, n) - G_{\alpha\beta}(m, n)) \tag{F.12}
\end{aligned}$$

and the rest are zero.

APPENDIX G. ASYMPTOTIC EVALUATION OF INCIDENT FIELD

Field due to a transducer at any depth x_3 can be written as

$$\phi(x_1, x_2) = \iint \hat{\phi}(k_1, k_2) e^{j(k_1 x_1 + k_2 x_2 + \sqrt{k^2 - k_1^2 - k_2^2} x_3)} dk_1 dk_2 \quad (\text{G.1})$$

where $\phi(k_1, k_2)$ is termed the angular spectrum of the transducer. For large x_3 , the above integral can be evaluated asymptotically through a saddle point evaluation.

$$\phi(x_1, x_2) = \int dk_2 e^{j k_2 x_2} \int \hat{\phi}(k_1, k_2) e^{j x_3 (k_1 a_1 + \sqrt{k_p^2 - k_1^2})} dk_1 \quad (\text{G.2})$$

where $a_1 = x_1/x_3$ and $k_p^2 = k^2 - k_2^2$. The stationary point can be found by setting

$$\partial(k_1 a_1 + \sqrt{k_p^2 - k_1^2})/\partial k_1 = 0 \quad (\text{G.3})$$

which results in $k_1^s = a_1 k_p / (1 + a_1^2)$. Knowing

$$\int_{-\infty}^{\infty} e^{z f(x)} dx \simeq \int_{-\infty}^{\infty} e^{f(x^s) + f''(x^s)(x-x^s)^2} dx = e^{f(x^s)} \sqrt{\frac{2\pi}{-z f''(x^s)}} \quad (\text{G.4})$$

$\phi(x_1, x_2)$ may be written as

$$\phi(x_1, x_2) = \int \hat{\phi}(a_1 k_p / (1 + a_1^2), k_2) \sqrt{\frac{2\pi k_p}{x_3 (1 + a_1^2)^{3/2}}} e^{j x_3 (k_2 a_2 + \sqrt{1 + a_1^2} \sqrt{k^2 - k_2^2})} \quad (\text{G.5})$$

Following the same steps for the evaluation of this integral, we obtain

$$\phi(x_1, x_2) = \hat{\phi}(k x_1 / r, k x_2 / r) \frac{2\pi k x_3}{r^2} e^{j k r} \quad (\text{G.6})$$

where the saddle point is located at $(k_1, k_2) = (k x_1 / r, k x_2 / r)$.

APPENDIX H. CALCULATION OF THE VOLTAGE USING THE RECIPROcity THEOREM

The voltage induced in a transducer due to an incident field generated by the same transducer is calculated in this section. Let's assume we have access to reflected E and H fields in the cable connected to the transducers for two separate cases of flaw and no-flaw situations. E and H are the electric and magnetic fields for the no-flaw case, and E' and H' correspond to the case with flaw existing. Using the electromechanical reciprocity theorem and conservation of power,

$$\nabla \cdot (i\omega U \cdot T' - i\omega U' \cdot T - E \cdot H' + E' \cdot H) = 0. \quad (\text{H.1})$$

where U is the displacement and T is the stress. Assuming Γ and Γ' are the reflection coefficients for the two cases of no-flaw and flaw respectively,

$$E = (1 + \Gamma)E^+ \quad (\text{H.2})$$

$$H = (1 - \Gamma)H^+ \quad (\text{H.3})$$

$$E' = (1 + \Gamma')E^+ \quad (\text{H.4})$$

$$H' = (1 + \Gamma')H^+ \quad (\text{H.5})$$

where E^+ and H^+ are the input electric and magnetic fields.

Utilizing the above equations, H.1 can be written as

$$i\omega \int \nabla \cdot (U \cdot T' - U' \cdot T) dv = 2(\Gamma - \Gamma') \int (E^+ \times H^+) \cdot n ds \quad (\text{H.6})$$

Knowing $\int (E^+ \times H^+) \cdot n ds = -2P$ and $\delta\Gamma = \Gamma - \Gamma'$

$$\delta\Gamma = \frac{i\omega}{4P} \int \nabla \cdot (U \cdot T' - U' \cdot T) dv \quad (\text{H.7})$$

Further limiting the equation of the motion to that of the ideal fluid,

$$\delta\Gamma = \frac{i\omega}{4P} \int (\lambda' - \lambda) U'_{i,i} U_{k,k} - \omega^2 (\rho' - \rho) U_i U'_i dv \quad (\text{H.8})$$

As a special case where $\rho = \rho'$, the above relationship simplifies to

$$\delta\Gamma = \frac{i\omega}{4\rho P} \int \left(\frac{1}{c_0^2} - \frac{1}{c(x)^2} \right) p p' dv \quad (\text{H.9})$$

where $p = u_{k,k}$ is the pressure in the fluid.

APPENDIX I. RELATIONSHIP BETWEEN VOLTAGE AND THE SCATTERER POTENTIAL

In this section, the results from the reciprocity theorem are used to derive a linearized acoustic inversion. Voltage induced in a transducer in the pulse-echo mode is given by

$$s(x', \omega) = R(\omega) \int [(\lambda' - \lambda)pp' - \omega^2(\rho' - \rho)U_i U_i'] dv \quad (I.1)$$

where $R(\omega)$ is the frequency response of the transducer. p is the pressure, and U_i is the i_{th} component of displacement when no flaw is present. All components superscripted with ' correspond to the case with the flaw. Assuming $\rho = \rho'$, the voltage can be written as

$$s(x', \omega) = R(\omega) \int v(x)p(x, \omega)p'(x, \omega) dx \quad (I.2)$$

where $v(x) = \omega^2(1/c_0^2 - 1/c(x)^2)$. Simplifying further, by applying the Born approximation $p = p'$, voltage s is written as

$$s(x', \omega) = R(\omega) \int v(x)p(x' - x, \omega)^2 dx \quad (I.3)$$

Next we express $p(x)$ as

$$p(x) = \int \hat{p}(k_1) e^{j(k_1 x_1 + \sqrt{k^2 - k_1^2} x_2)} dk_1 \quad (I.4)$$

Using the steepest descent evaluation of the above integral for large x_2 , $p(x)$ may be written as

$$p(x, \omega) = \sqrt{\frac{2\pi\omega}{jrc}} \frac{x_2}{r} e^{jkr} \quad (I.5)$$

By substituting the Eq. (I.5) in Eq. (I.3) we obtain

$$s(x'_1, \omega) = -2\pi kj \int \frac{x_2^2}{r^3} e^{j2kr} v(x_1, x_2) dx_1 dx_2 \quad (I.6)$$

Above integral is in the convolutional form with respect to variable x_1 , where $v(x_1, x_2)$ is convolved with $\mathcal{W}(x_1, x_2)$ defined as

$$\mathcal{W}(x_1, x_2) = \frac{x_2^2 e^{j2kr}}{r^3} \quad (I.7)$$

where $r = \sqrt{x_1^2 + x_2^2}$. Taking the spatial Fourier transform with respect to x_1 will result in

$$\hat{s}(k_1, \omega) = -2\pi j \int \hat{\mathcal{W}}(k_1, x_2) \hat{v}(k_1, x_2) dx_2 \quad (I.8)$$

where

$$\hat{\mathcal{W}}(k_1, x_2) = \int \frac{x_2^2 e^{j2\omega r/c}}{r^3} e^{-jk_1 x_1} \quad (I.9)$$

$\hat{\mathcal{W}}(k_1, x_2)$ may be evaluated using the method of steepest descent for large x_2 resulting in

$$\hat{\mathcal{W}}(k_1, x_2) = \sqrt{\frac{2\pi j}{x_2}} \frac{(4\omega^2/c^2 - k_1^2)^{3/4} c^2}{4\omega^2} e^{j\sqrt{4\omega^2/c^2 - k_1^2} x_2} \quad (I.10)$$

Substituting Eq. (I.10) in Eq. (I.8) results in

$$\hat{s}(k_1, \omega) = \frac{(2\pi)^{3/2} c e^{-j\pi/4}}{4\omega} (4\omega^2/c^2 - k_1^2)^{3/4} \int v(k_1, x_2) e^{j\sqrt{4\omega^2/c^2 - k_1^2} x_2} dx_2 \quad (I.11)$$

Finally, the voltage is expressed in terms of the spatial Fourier transform of the scatterer potential as

$$\hat{s}(k_1, \omega) = \frac{(2\pi)^{3/2} c e^{-j\pi/4}}{4\omega} (4\omega^2/c^2 - k_1^2)^{3/4} \hat{v}(k_1, \sqrt{4\omega^2/c^2 - k_1^2}) \quad (\text{I.12})$$

APPENDIX J. FOCUSING OF AN ARRAY OF TRANSDUCERS

In many applications it is desired to image interior of a solid through measurements taken with transducers immersed in water. The imaging in effect is summarized in focusing of all transducers for all points in the solid. If the spatial frequency response (SFR), angular orientations, and positions of the transducers are known, it is possible to calculate the complex weights necessary for producing a focus at a given depth inside the solid. The case at hand requires forming a beam inside solid by adjusting the complex gain of transducers in water. In order to accomplish this objective, the relationship between the field produced by the transducer and the field inside the solid should be understood. One may start with the relationship between incident plane wave and resultant field in the solid as the building block for the relationship between the field in solid due to a more complex waveform. This can be achieved by utilizing the assumption that actual waveform can be expressed as a weighted sum of plane waves.

The problem at hand can be viewed as finding complex gains of each transducer such that they form a desired SFR at a prescribed depth inside the solid. The desired SFR can be written as the superposition of SFR corresponding to each transducer.

$$\Psi(k_1, k_2) = \sum_{i=1}^N \psi_i(k_1, k_2) z_i \quad (\text{J.1})$$

where z_i is the unknown complex weight and

$$\psi_i(k_1, k_2) = A^{tl} \psi(k'_1, k'_2) e^{-j(kp - k_3 a) \frac{k'_3}{k_3}} \quad (\text{J.2})$$

where A^{tl} is the transmission coefficient of the transmitted L wave, and $\psi(k_1, k_2)$ is the SFR of the transducer oriented parallel to the interface with its axis passing through the point of focus. k'_1 and k'_2 are components of k vector after rotation by an angle θ and ϕ .

$$\begin{pmatrix} k'_1 \\ k'_2 \\ k'_3 \end{pmatrix} = \begin{pmatrix} \sin(\phi)\cos(\theta) & \sin(\phi)\sin(\theta) & \cos(\phi) \\ \cos(\phi)\cos(\theta) & -\cos(\phi)\sin(\theta) & \sin(\phi) \\ \sin(\theta) & \cos(\theta) & 0 \end{pmatrix} \begin{pmatrix} k_1 \\ k_2 \\ k_3 \end{pmatrix} \quad (\text{J.3})$$

A pure L type plane wave is incident on a water-solid interface. The plane wave has an amplitude of unity expressed as e^{jkx} . The resultant field is composed of a reflected L type wave in water and transmitted L and S type wave inside solid. The transmission coefficients are

$$A^{tl} = \frac{2bk_{ts}^2 k_3 (k_r^2 - (k_3^{ts})^2)}{D} \quad (\text{J.4})$$

$$A^{rl} = 1 + \frac{2bk_{ts}^4 k_3^{tp}}{D} \quad (\text{J.5})$$

$$A^{ts1} = \frac{4bk_{ts}^2 k_2 k_3 k_3^{tp}}{D} \quad (\text{J.6})$$

$$A^{ts2} = -\frac{4bk_{ts}^2 k_1 k_3 k_3^{tp}}{D} \quad (\text{J.7})$$

$$D = -k_3 [(k_r^2 - (k_3^{ts})^2)^2 + 4k_3^{ts} k_3^{tp} k_r^2] - bk_{ts}^4 k_3^{tp} \quad (\text{J.8})$$

where A^{tl} , A^{rl} , A^{ts1} , and A^{ts2} are coefficients for the reflected L wave, transmitted L wave, and transmitted S waves respectively.

In order to solve for the complex gain z_i , one can minimize the distance between the ideal SFR and the synthesized SFR. The distance can be defined as

$$\begin{aligned} \mathcal{E} = & \int \int \left[\sum_{i=1}^N \psi_i(k_1, k_2) z_i - \Psi(k_1, k_2) \right] \\ & \left[\sum_{i=1}^N \psi_i(k_1, k_2) z_i - \Psi(k_1, k_2) \right]^* dk_1 dk_2 \end{aligned} \quad (\text{J.9})$$

assuming $z_i = x_i + jy_i$, we can derive

$$\begin{aligned} \frac{\partial \mathcal{E}}{\partial x_m} = & \int \int \left\{ \sum_{i \neq m} c_i c_m^* (x_i + jy_i) + \right. \\ & \sum_{k \neq m} c_m c_k^* (x_k - jy_k) + \\ & \left. 2c_m^2 x_m - (c_m q_m^* + c_m^* q_m) \right\} dk_1 dk_2 \end{aligned} \quad (\text{J.10})$$

$$\begin{aligned} \frac{\partial \mathcal{E}}{\partial y_m} = & \int \int \left\{ \sum_{i \neq m} c_i c_m^* (y_i - jx_i) + \right. \\ & \sum_{k \neq m} c_m c_k^* (y_k + jx_k) + \\ & \left. 2c_m^2 y_m - (c_m q_m^* - c_m^* q_m) \right\} dk_1 dk_2 \end{aligned} \quad (\text{J.11})$$

By setting the above equations to zero, we obtain

$$\begin{pmatrix} A & B \\ -B & A \end{pmatrix} \begin{pmatrix} X \\ Y \end{pmatrix} = \begin{pmatrix} Q_1 \\ Q_2 \end{pmatrix} \quad (\text{J.12})$$

Although above matrix is a $2N \times 2N$ matrix, due to symmetry only two $N \times N$ matrix inversion is necessary.

$$Y = (A^{-1}B + B^{-1}A)^{-1}(A^{-1}Q_1 + B^{-1}Q_2) \quad (\text{J.13})$$

$$X = A^{-1}(Q_1 - BY) \quad (\text{J.14})$$